Author's personal copy

Provided for non-commercial research and educational use.
Not for reproduction, distribution or commercial use.

This article was originally published in Comprehensive Inorganic Chemistry III, published by Elsevier, and the attached copy is provided by Elsevier for the author's benefit and for the benefit of the author's institution, for non-commercial research and educational use including without limitation use in instruction at your institution, sending it to specific colleagues who you know, and providing a copy to your institution's administrator.

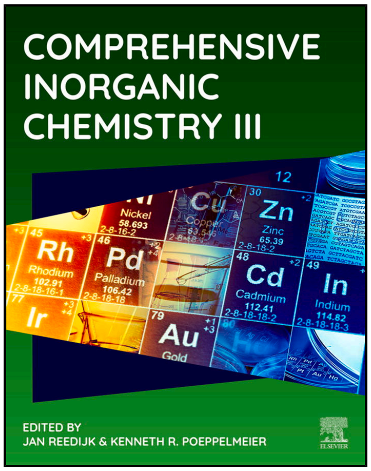

All other uses, reproduction and distribution, including without limitation commercial reprints, selling or licensing copies or access, or posting on open internet sites, your personal or institution's website or repository, are prohibited. For exceptions, permission may be sought for such use through Elsevier's permissions site at:
https://www.elsevier.com/about/our-business/policies/copyright/permissions

Bocus, M.; Neale, S. E.; Cnudde, P.; Van Speybroeck, V. Dynamic evolution of catalytic active sites within zeolite catalysis. In *Heterogeneous Inorganic Catalysis;* van Santen, R. A.; Hensen, E.; in Comprehensive Inorganic Chemistry III; Reedijk, J., Poeppelmeier, K. R., Eds.; Vol. 6, pp 165–200. Oxford: Elsevier. ©2023 Elsevier Ltd. ISBN 9780128231531. DOI: B978-0-12-823144-9.00012-1.

ISBN: 9780128231449

Copyright © 2023 Elsevier Ltd. All rights reserved

Elsevier

Author's personal copy

6.08 Dynamic evolution of catalytic active sites within zeolite catalysis

Massimo Bocus, Samuel E. Neale, Pieter Cnudde, and Véronique Van Speybroeck, Center for Molecular Modeling, Ghent University, Tech Lane Ghent Science Park Campus A, Zwijnaarde, Belgium

© 2023 Elsevier Ltd. All rights reserved.

Abstract

Zeolites with Brønsted acid and cation-exchanged sites are extremely effective single-site heterogeneous catalysts and are routinely employed in various industrially important processes such as MTH and SCR. However it is now generally accepted that these sites of catalytic activity are not necessarily statically fixed to the zeolite architecture, but are more dynamic in nature and can mobilize within the pores & cages of the respective zeolites at operando conditions. Herein, an overview of the state of understanding of the mobility of (i) protons in pristine BAS-zeolites, (ii) aluminum ions in the process of framework decomposition, and (iii) metal sites in TM-exchanged zeolites is presented. In turn, the state of play of computationally probing active-site mobility will then be discussed, whereby enhanced sampling techniques is highlighted in particular as an emerging and promising method for probing active site mobility. Finally, a selection of case studies are highlighted, in which enhanced sampling techniques were employed to elucidate the mobility of catalytic sites in zeolites.

6.08.1 Introduction

Over the last decades, zeolites have become the workhorse for acid-catalyzed transformations in the chemical industry with applications in (hydro)cracking, methane reforming, methanol-to-hydrocarbons (MTH), NOx reduction, biomass upgrading, etc.[1–5] Owing to their large surface area and characteristic porous network which exhibits a unique type of shape selectivity, zeolites compose a versatile class of materials for catalyzing chemical transformations which would otherwise be too highly activated to be feasible. Archetypical zeolites are crystalline microporous aluminosilicate frameworks built up by SiO_4 or AlO_4 tetrahedra. The incorporation of trivalent Al^{3+} as substituent for the tetravalent Si^{4+} ions in the framework results in the creation of catalytically active sites in the framework, shown in **Fig. 1**.[2] The overall negative charge on the framework can be compensated by the incorporation of cationic species. If protons (H^+) are introduced as charge-compensating cations, strong Brønsted acid sites (BAS) are formed as bridging hydroxyl groups. Alternatively, charge balancing can be accomplished by other cationic species such as metallic cations or (transition) metal complexes, giving rise to redox sites or Lewis acid sites (LAS). Albeit less common, lattice modifications through isomorphous substitution of framework Si sites by other trivalent (B^{3+},Fe^{3+},Ga^{3+}, …) or tetravalent (Sn^{4+},Ti^{4+}, Zr^{4+}, …) heteroatoms also lead to the introduction of Brønsted and Lewis acid sites respectively in the catalyst. Finally, depending on the specific conditions during the zeolite synthesis and hydrothermal treatment, these heteroatoms and bridging hydroxyl groups

Comprehensive Inorganic Chemistry III, Third Edition, 2023, 165–200

Author's personal copy

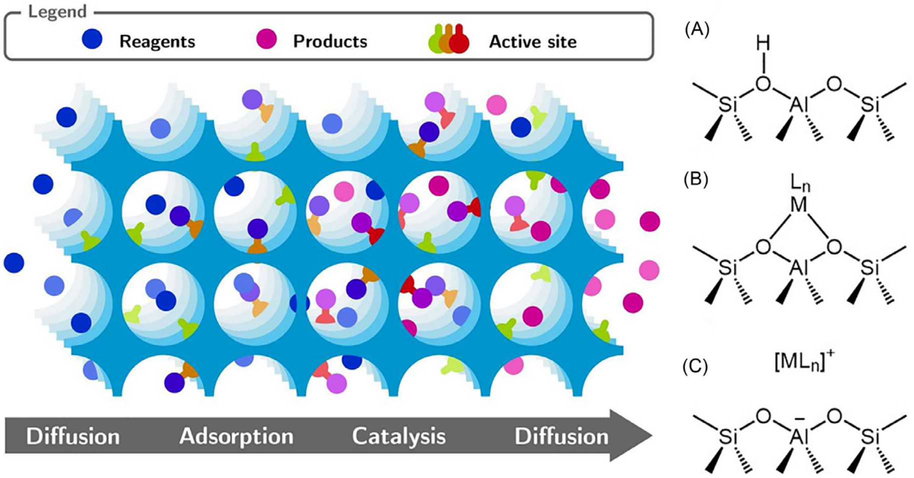

Fig. 1 Schematic representation of the steps occurring in acid zeolite catalyzed reaction. The active sites: (A) Brønsted acid sites (BAS), (B) framework-bound Lewis acid sites (LAS) and (C) mobilized LAS, can dynamically change by interacting with the reacting species, as highlighted by the different colors.

can to some extent be extracted from the framework, leading to the formation of LASs in the form of extra-framework species like extra-framework aluminum (EFAl).[6–9]

Tailoring the catalytic function of the formed Bronsted and Lewis acid sites is a critical factor in achieving zeolite catalysts with a high activity.[10,11] While the activity of BASs stems from the (partial) proton transfer to basic guest molecules, LASs are characterized by a vacant orbital of the metal complex which can coordinate with electron-rich groups of the guest species. The catalytic behavior of the zeolite catalyst is often not solely determined by intrinsic reaction rates, but also by diffusion phenomena as well as the location, density and strength of the acid sites.[12–15] The latter are key characteristics influencing the activity and selectivity of the catalyst which can be tuned by altering the type of the charge-compensating cations and their locations in the framework. Recently, dedicated studies showed progress towards controlling the targeted acid site distribution in the zeolite micropores.[16–19] Computational modeling has become ubiquitous for obtaining insight into the nature of the active sites and their interaction with crucial reaction intermediates and products. The ultimate goal is to unravel the catalytic mechanism and reactivity of the zeolite catalyst, which may eventually lead to dedicated control of the product selectivity and mitigating catalyst deactivation.

One of the main challenges in modeling catalytic processes on heterogeneous nanoporous catalysts is to accurately describe the interactions of adsorbates with the catalytically active sites at operating conditions. The state and the function of the catalytic material is critically dependent on the external conditions such as temperature, pressure, acidity, presence of moisture, … Specifically, zeolites were long believed to behave as rather static materials with a well-defined pore topology and a very stable lattice consisting of relatively strong Si—O and Al—O bonds. However, recent awareness has grown that the catalytic function may dynamically reorganize upon exposing the material to varying external process conditions.[10,20–23] In this sense, the active sites do not remain unaltered at fixed framework positions but can instead evolve in the course of the reaction. Depending on several factors such as the synthesis conditions, reaction temperature and presence of guest species, the active sites can actually detach from the framework and transform into mobile sites inside the catalyst micropores. For example, the intrinsic mobility of Brønsted acid protons, a phenomenon labeled proton hopping, is a function of the local structure and composition of the zeolite as well as the temperature.[24–26] At low temperature, liberated protons tend to jump solely between the four framework oxygens adjacent to the Al substitution, while at high temperature, protons may travel further to nearby framework positions.[27] The presence of protic molecules like ammonia, water or methanol around the BAS is also known to induce proton mobility by formation of ion-paired hydronium or methanol clusters.[28–34] Furthermore, even unsaturated apolar hydrocarbons such as alkenes or aromatics might readily deprotonate the framework, facilitating proton transfer through the formation of carbocation intermediates.[35–37]

Lewis acid sites are characterized by their dynamic nature as well due to the existence of both framework-bound complexes and extra-framework complexes detached from the lattice.[38–42] Framework-modified zeolites may thus contain a heterogeneous distribution of active sites in the micropores, ranging from isolated cationic species over mono- or binuclear metal-oxo complexes to metal oxide nanoclusters and the nature of these sites can be significantly affected by the specific reaction conditions.[11] Interestingly, the nature and stability of the catalytically active sites is sensitive to the zeolite topology and chemical composition, i.e., the distribution and/or proximity of the Al substituents in the framework.[39] Accurate zeolite models capable of capturing this complex active site behavior are therefore essential to understand and predict the outcome of relevant catalytic processes. To achieve this goal, a close synergy between theoretical simulations and experimental characterization to identify the precise nature of the active sites is indispensable.[43]

Assessing the precise location and dynamic behavior of the active sites is a topical subject in zeolite catalysis. Fundamental insight into catalytic materials is only possible by a strong connection of theoretical and experimental data. In this context, the

Author's personal copy

recent developments of in situ and operando spectroscopy techniques to map the function of the material with high spatial and temporal resolution at operating conditions is very promising.[44,45] In this article, we will demonstrate how theoretical models can aid in characterizing the active site mobility in acid zeolite catalysts and gaining a proper atomic level understanding on the interactions of guest molecules with the active sites. First, the state-of-the-art on the role of the different active sites in zeolite catalysis, i.e., Brønsted acid sites, (partially) hydrolyzed Al sites and transition metal-exchanged sites, will be introduced. A clear connection to both experimental and theoretical methods is given to identify the dynamic evolution of active sites at operating conditions. Subsequently, various computational methodologies to account for the operando and in situ catalytic conditions will be briefly reviewed. Finally, four case studies will be discussed demonstrating the value of operando modeling tools in characterizing the nature of the active sites. The first case study describes the Brønsted acid proton mobility in the context of methanol-to-hydrocarbons (MTH) conversion and ethanol dehydration. The second case study is devoted to Nickel active sites in ethylene oligomerization. The third and fourth example concern the investigation of H-SSZ-13 and Cu exchanged zeolites respectively for the selective catalytic reduction (SCR) of NOx. Each case study highlights how the acid function in zeolites can typically not be considered as a static site on the lattice but will rather change dynamically depending on the complexity of the operating environment and process conditions. Capturing this behavior correctly is a prerequisite in order to predict the catalytic properties and design catalysts with improved selectivities as well as enhanced lifetimes.

6.08.2 Experimental and theoretical evidence for active site mobility in zeolites

6.08.2.1 Proton mobility in Brønsted-acidic zeolites

If the charge compensation of the zeolite framework occurs through incorporation of a proton, bound to a bridging Si-O-Al oxygen atom, Brønsted acid sites (BAS) are formed. Despite its apparent simplicity, the BAS already possesses dynamic behavior that can significantly affect its catalytic properties. Herein, a survey of evidences collected for BAS mobility is presented for two situations of increasing complexity, namely proton mobility in the pristine zeolite framework (Fig. 2A) and proton mobility induced by the presence of adsorbed protic guest molecules (Fig. 2B and C).

6.08.2.1.1 BAS mobility in the pristine zeolite framework

In zeolites or zeotype materials, the BAS is commonly depicted as a static moiety, strongly anchored to a framework oxygen and dissociation is only considered upon active participation of the proton in the reaction under investigation, for instance by protonating an organic substrate. Proton transfer and exchange is indeed a key initial step in multiple important industrial processes, like aromatic electrophilic substitution[46] and alkene cracking.[36,37] The static description of the BAS is, however, contradicted by experimental observations above a certain temperature. ^{1}H solid state Magic-Angle-Spin Nuclear Magnetic Resonance (MAS NMR) represents one of the major techniques to investigate the nature of protons in zeolites.[47] Measurements conducted on various zeolites have proven that, above a temperature of ~400 K, the BAS is no longer localized on a specific site but rather hops between the 4 Al-bound oxygen atoms (Fig. 2A).[48–55] Despite a general agreement on the temperature induced free proton hopping, the barriers obtained for this process are seldom in agreement (Table 1).[49–51] In H-ZSM-5, for instance, barriers ranging between 11 and 45 kJ mol^{-1} have been reported. For the first value, the variation in the BAS signal width with temperature was considered and it has then later been suggested that partial overlap with a broad peak at higher ppm—initially not visible because of technical limitations—could be responsible for the values discrepancy (vide infra and Fig. 3) but a definitive conclusion is, to the best of our knowledge, not yet reported.[62]

Proton hopping can also be investigated using InfraRed (IR) spectroscopy,[56,63] with the advantage that even higher temperatures can be reached with respect to NMR. The decrease in intensity of the O-H stretching mode peak with increasing temperature is normally monitored. Such decrease has been attributed to the dissociation of the O—H bond, consistent with proton hopping. By deducing the equilibrium constant of the hopping from the integrated intensity at various temperatures, Osuga et al.[56] were able to use the Van't Hoff equation to retrieve the activation energy of the process. Surprisingly, they found two different temperature regions with two different activation energies: for medium-high temperatures (398–548 K, 37–28 kJ mol^{-1} in H-ZSM-5) they attribute the decrease in intensity to a localized hopping on the first coordination sphere around the Al defect, while at higher

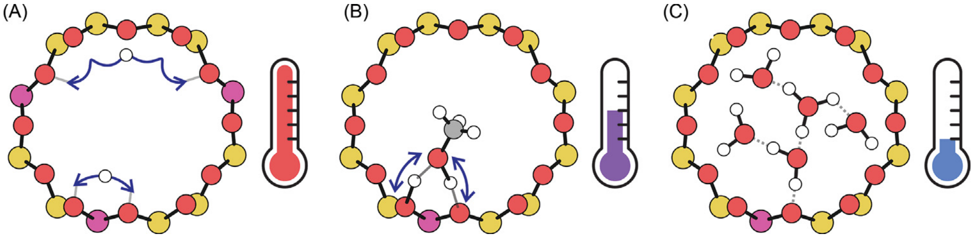

Fig. 2 Schematic depiction of the BAS mobilization in the framework in different circumstances. (A) Proton hopping in the pristine framework at high temperatures. (B) Proton hopping mediated by an adsorbed protic molecule (methanol for example). (C) Fully solvated BAS at low temperature. Color code: H white, C gray, O red, Si yellow and Al purple.

Author's personal copy

Table 1 Apparent activation energies for the proton hopping in various zeolite frameworks, with different Si/Al ratios and different methodologies, as extracted from the available literature.

Zeolite	*Si/Al*	*Methodology*	E_{app}^{act} *(kJ mol^{-1})*	*References*
H-ZSM-5	21	^{1}H NMR[a]	11	49
	38	^{1}H NMR[b]	45	50
	12–53	^{1}H NMR[a]	17–20	51
	35–90	IR	(37–28)-(23 – 22)[c]	56
	15–500	Impedance spectroscopy	89–126	57,58
	–	DFT (cluster)	117	59
	–	QM-pot	52–98	60
H-MOR	7	^{1}H NMR[b]	54	50
	39	IR	23–24[c]	56
	53	^{1}H NMR[a]	28	52
H-Y	1.2–2.6	^{1}H NMR	21–42	48
	3	^{1}H NMR[b]	61	50
	3	^{1}H NMR[a]	50	55
	–	QM-pot	68–106	60
H-SSZ-13	39	IR	23–18[c]	56
	11	QM-pot	58–97	61
	11	QM-pot	70–102	60

[a] Based on the linewidth of isotropic resonance.

[b] Based on the intensity loss of spin sidebands with temperature.

[c] Different values for low (398–548 K) and high (573–773 K) temperatures, respectively.

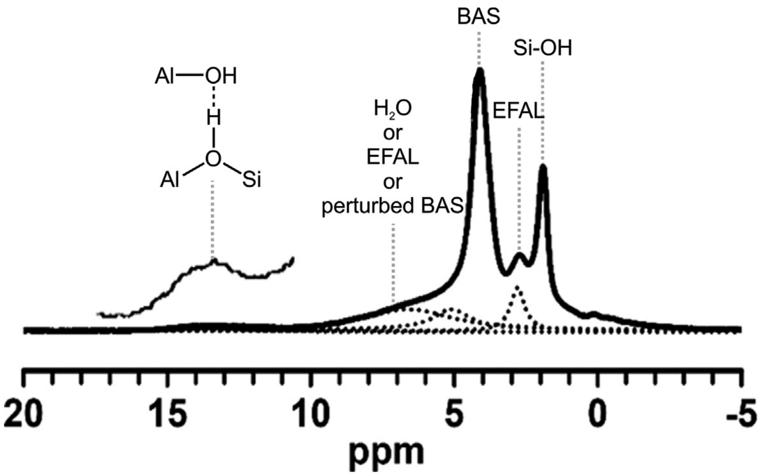

Fig. 3 ^{1}H MAS NMR spectrum of the H-ZSM-5 zeolite (Si/Al = 15). The inset shows a magnification of the 10–17 ppm region. The most common attributions for each peak are shown. Adapted with permission from Chen, K.; Abdolrahmani, M.; Horstmeier, S.; Pham, T.N.; Nguyen, V.T.; Zeets, M.; Wang, B.; Crossley, S.; White, J.L., Brønsted–Brønsted Synergies Between Framework and Noncrystalline Protons in Zeolite H-ZSM-5. *ACS Catal.* **2019**, *9*(7), 6124–6136. Copyright 2019, American Chemical Society.

temperatures (573–773 K, 23–22 kJ mol^{-1}) they invoked a more delocalized hopping, in which the proton can almost freely move in the zeolite pores (Fig. 2A). Such an inter site hopping has also been previously proposed based on impedance spectroscopy experiments,[57,58] in which higher activation energies were however found (89–126 kJ mol^{-1}, decreasing with decreasing Si/Al ratio).

Static calculations[64] provided even higher barriers for the inter Al proton hopping with similar Si/Al ratio as the impedance spectroscopy, although the correlation with the Si/Al ratio was maintained ($>$200 kJ mol^{-1}). This disagreement between computational and experimental proton hopping barriers is quite general in the available literature. Many computational investigations of proton hopping around the first coordination sphere of Al have been performed with static methodologies, both on cluster[59,65,66] and periodic[60,61,64,67] models. It was found that the activation energy strongly depends on the two specific oxygens involved in the hopping. As an example, Sierka & Sauer[61] reported zero-point corrected barriers for proton hopping in a fully periodic H-SSZ-13 model varying between 58 and 97 kJ mol^{-1}, as a function of the considered O atoms (B3LYP/T(O)DZP). Again, the computed activation energies are significantly higher than the experimentally measured ones (Table 1). As the adsorption of protic molecules on the BAS has been proposed to significantly reduce the hopping barriers (vide infra), it has been proposed that the lower experimental values

Author's personal copy

could be justified by the presence of residual amounts of water in the catalyst. A broad band centered at ~6 ppm, observed in the ^1H NMR spectrum of H-ZSM-5 (**Fig. 3**), was indeed later attributed to residual adsorbed water sticking to the framework even after high temperature drying,[62] despite previous reports providing different interpretations.[68–72] In more recent investigations, however, new evidences have suggested that such band would be produced by ExtraFramework ALuminum species (EFAL), as discussed more in detail in **Section 6.08.2.2**,[73] or by BAS involved in H-bonds with framework oxygens.[74]

6.08.2.1.2 Protic molecules mediated hopping and solvation of the BAS

Protic molecules adsorbed on the BAS can mediate proton hopping between (adjacent) oxygen atoms, with a reduced barrier caused by the less tensioned transition state (**Fig. 2**B).[59,75] The adsorption of a single water molecule on the BAS is related to the formation of a strong hydrogen bond. [76,77] Despite the BAS remaining bound to the framework, the hopping barrier around the Al is reduced from 117 to 17 kJ mol^{-1} in H-ZSM-5, according to Ryder et al.[59] Due to the high acidity of the BAS, not only typical amphoteric molecules (such as water and alcohols) can facilitate the hopping, but also aromatics[78,79], alkenes and even alkanes.[80,81] While a single protic molecule adsorbed on the BAS can easily exchange protons, multiple sufficiently basic adsorbates (depending on the acidity of the zeotype material under study) can completely abstract it from the framework, forming positively charged clusters (**Fig. 2**C). Being the most studied protic molecule in zeolites, this section focuses on the computational and experimental evidence concerning the water solvation of protons in zeolites. Such behavior is, of course, more general and applies also to other interesting protic molecules, such as methanol. In **Section 6.08.3.2.1**, more details will be provided on how advance sampling techniques have played a key role in elucidating how the cooperative action of methanol molecules influences some key steps in the MTH process.[82,83]

The adsorption of water in zeolites provides a further degree of complexity to the catalyst. As shown by theoretical calculations in H-SSZ-13[84] and Al K-edge X-ray Adsorption Near Edge Structure (XANES) of H-ZSM-5,[30] about 50% of the protons is still solvated at water loadings as low as 1 water molecule per BAS. This clearly points towards a heterogenous distribution of the water molecules in the zeolite, that prefer to aggregate in cluster of 2–3 molecule while leaving some BAS dehydrated instead of homogenously adsorb over all active sites. This is caused by the large energy gain caused by proton solvation when a sufficiently large cluster of water molecules is interacting with the BAS. Addition of two water molecules on the BAS causes the proton to easily shuttle between the zeolite and the water cluster. Metadynamics was used to quantify the barrier of the process, that was found to be in the order of k_BT at 330 K.[85] Once three or more molecules are adsorbed on the BAS, the proton gets solvated as hydronium ion and the abstraction from the framework becomes fundamentally complete. This behavior is very common for all zeolite and zeotype materials with strong BAS and has received widespread support from inelastic neutron scattering[86] and diffraction,[28] ^1H NMR,[87] IR spectroscopy[28,88] and many theoretical works employing MD simulations, starting from the late 1990s.[29,83,84,89–92]

Upon further increasing the amount of adsorbed water, the size of the protonated clusters can grow up to 7–8 water molecules before condensation is observed (in H-ZSM-5, independently on the Si/Al ratio, see **Fig. 4**).[93,94] Such clusters retain a structure that is mostly similar to gas-phase instead of solvated hydronium ions in pure liquid water.[30] After this point, the enthalpy of adsorption of water converges to the heat of condensation[94] and liquid water starts to condensate in the channels of the zeolite. This was also shown by an investigation of proton mobility with IR spectroscopy, monitoring the H/D exchange rate in the catalyst. The enthalpy variation associated with proton mobility decreases with increasing water content, which was interpreted by the formation of water chains connecting different Al sites, and thus the passage from isolated positive clusters migration towards a Grottuß-like mechanism.[25,26]

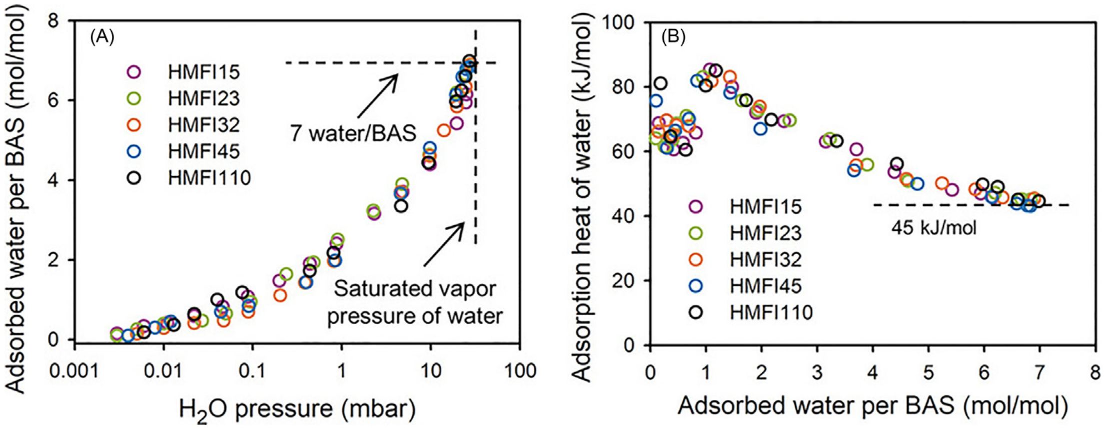

Fig. 4 (A) Number of water molecules per BAS as a function of the water partial pressure for H-ZSM-5 with different Si/Al ratio. As clearly visible, the amount of adsorbed water does not depend on the BAS density and stops at 7 water/BAS before condensation is observed. (B) Adsorption heat of water as a function of the number of water molecules adsorbed on the BAS. The value is initially high and converges to the condensation heat of water (~45 kJ·mol^{-1}) at 7 water molecules/BAS. Taken from https://doi.org/10.1002/anie.201812184.

Author's personal copy

It goes without saying that the formation of protonated clusters of solvent inside the zeolite catalyst has deep consequences in terms of reactivity, that has led to a significant amount of theoretical investigations. The presence of many (different) adsorbed molecules makes the use of static methodologies unsuitable as a lot of configurations should be taken into account[95]. Therefore, advanced sampling techniques have been employed to elucidate proton mobility, as presented in **Section 6.08.3.2.1**.

6.08.2.2 Framework-associated and extra framework aluminum (EFAL)

So far we discussed the transformations occurring at the BAS at reaction conditions without an effective modification of the zeolite skeleton. Now, the scope of active site modification will be extended in time by considering the breaking of framework bonds, which is normally associated with the (partial) extraction of aluminum defects. Zeolite dealumination is a wide and complex field of research. Many reactions can be involved, depending on zeolite loading, temperature, pH, neutralizing cation, etc. Moreover, dealumination is strongly related to desilication and therefore to the processes of mesopore formation and zeolite dissolution in medium and harsh water treatment, respectively. The purpose here is to provide a general overview of the current understanding in the EFAL chemistry of formation and effect on catalysis. For a more exhaustive discussion, the interested reader is referred to some recent literature reviews focused solely on the topic.[6,96,97]

By exposing zeolites to steam at high temperatures, to hot liquid water or, more in general, after hydrothermal synthesis, Al atoms can be extracted from the framework.[96] If the Al still maintains covalent bonds with the framework, it is referred to as framework-associated Al, while if it forms a physisorbed cluster, it is called an Extra Framework ALuminum (EFAL).[6] Despite EFALs being often associated with Lewis acidity, a survey of the available literature unravels that a lack of correlation exists between the amount of EFAL species and the measured Lewis acidity (**Fig. 5**).[6] This is likely caused by the fact that many techniques exist to probe the Al location in the framework and the Lewis acid character, which may lead to various results depending on multiple factors (as a trivial example, the dimensions of a probe basic molecule when quantifying acidity with IR spectroscopy).

Concerning the formation of EFAL and framework-associated Al, elucidating the mechanism of zeolite dealumination is a challenging task both experimentally and computationally.[97,98] While the zeolite framework has mostly been considered inert unless subjected to relatively high temperatures and/or water pressures, it has recently become obvious that its bonds are much more dynamic than previously thought. Both Si—O and Al—O bonds have been found to be very labile already at room temperature when liquid water is present in the pores of the H-SSZ-13 zeolite. The barriers for Si—O and Al—O bond cleavage were calculated

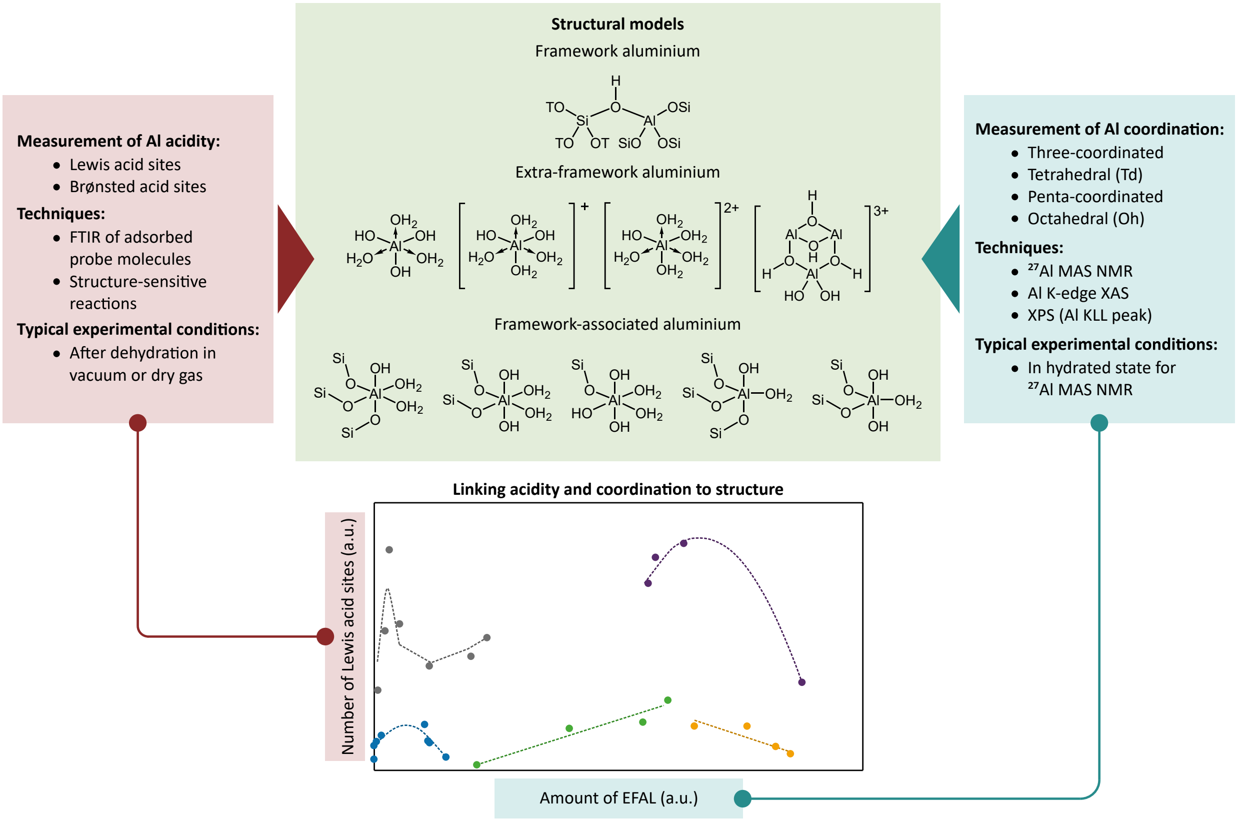

Fig. 5 Common methods for the measurement of the EFAL amount (*right*) and Lewis acidity (*left*). The central green panel shows some possible structures for EFALs and framework-associated Al while the bottom graph the lack of correlation between number of LAS and EFAL with data from the available literature. Adapted from https://doi.org/10.1038/s41563-020-0751-3.

Author's personal copy

to be only ~60 and ~25 kJ mol^{-1}, respectively.[99] This lability has also been confirmed experimentally by monitoring the easy integration of ^{17}O in multiple zeolite frameworks when exposed to $H_2{}^{17}O$ through NMR spectroscopy.[100] In the same study, it was also highlighted how Si-O-Al bridging oxygens are exchanged faster than Si-O-Si ones, in line with the computational results. Similarly, T-O-T reversible bond breaking in H-SAPO-34 has been proved by introducing in the framework bulky organic molecules, that would not be able to diffuse through the material unless the cages-connecting windows are enlarged by fast and reversible hydrolysis of the framework bonds.[101]

Moving to harsher treatments, the full dealumination mechanism at steaming conditions ($T > 673$ K, ~1 atm of steam) has been thoroughly investigated in the literature. Initial mechanistic investigations were performed using static DFT simulations.[102,103] A first proposal by Malola et al.[103] foresaw the passage through the formation of a vicinal disilanol[104–106] defect ($\equiv Si(OH)_2Al\equiv$) in H-SSZ-13, but was leading to prohibitively high reaction barriers (190 kJ mol^{-1}) for dealumination. Afterwards, a much more affordable mechanism (barrier of ~100 kJ mol^{-1}) starting with a water molecule attacking the Al atom in *anti* with respect to the bridging hydroxyl group was proposed[107–109] and later confirmed experimentally with ^{27}Al NMR, with which it was found that Al sites located in the channel intersection of H-ZSM-5—whose *anti* position is the most exposed—are more susceptible to abstraction.[110] The role of the number of water molecules on the dealumination has also proven to be important. While static calculations can still provide interesting insights,[111,112] a step forward towards the achievement of more realistic experimental conditions was performed by Nielsen et al., who used advanced sampling techniques to assess the influence of multiple water molecules on the dealumination barriers. The water molecules were shown to collectively cooperate in the extraction of the Al atom from the framework, by facilitating the proton transfers between different oxygens. The reaction proceeds through a stepwise cleavage of the Al—O bonds, with initial expansion of the Al coordination sphere by *anti* water addition. The barriers for each step are in the order 90–100 kJ mol^{-1}, similar to the results from static calculations, but increase by 10–20 kJ mol^{-1} when the amount of water molecules per BAS is reduced from 3 to 1 (**Fig. 6**).[113] Interestingly, the existence of partially hydrolyzed Al atoms, i.e., the intermediates in the proposed mechanism, has been identified multiple times in the literature based mainly on ^{27}Al NMR experiments and they are expected to play an important catalytic role at reaction conditions (see **Fig. 7**C and D).[114–116]

Once the Al is extracted from the framework, it is still unclear in which form it is more likely to persist in the catalyst. Initial theoretical investigations assumed the existence of mononuclear hydroxy-aquo complexes of the form $[Al(OH)_x(H_2O)_{n-x}]^{3-x}$.[117–119] ^{27}Al NMR experiments on H-ZSM-5 seem to suggest that a tetrahedral coordination is predominant, with octahedral Al appearing only at very long steaming times (~20 h).[120] Similarly, XANES measurements in H-β and H-MOR indicated that octahedral Al is present only at low temperatures and quantitatively converts in tetrahedral Al above 395 K.[121] Octahedral Al can however be relevant in other conditions. Recent ^{27}Al NMR experiments coupled with IR spectroscopy have shown that

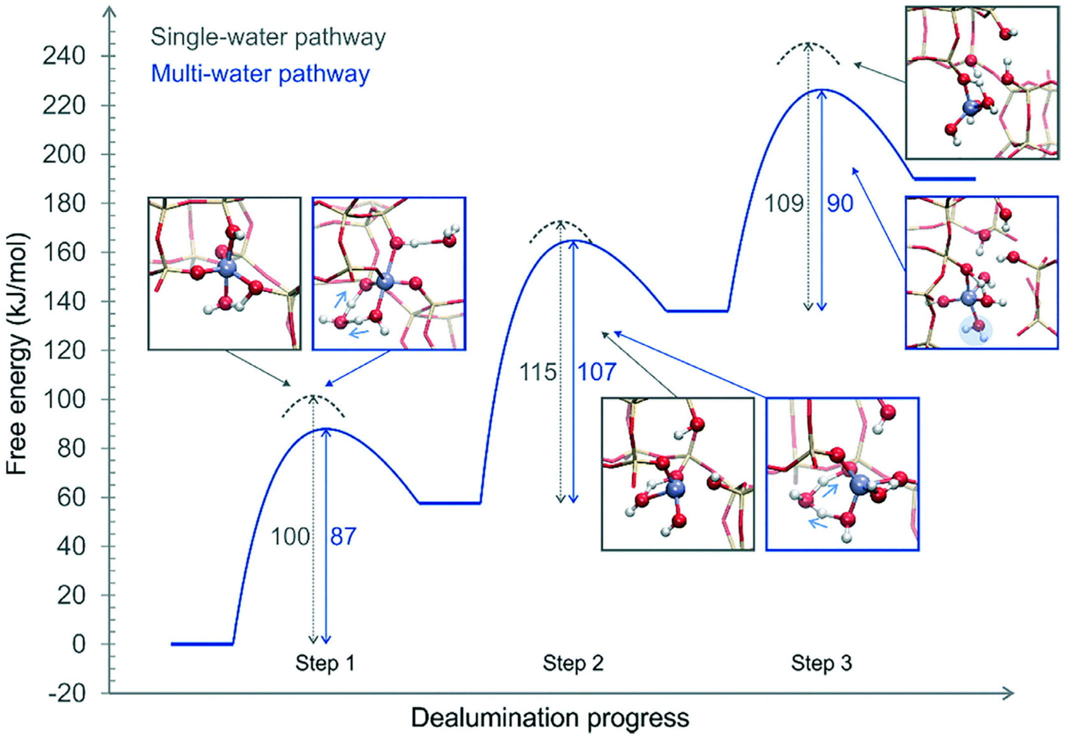

Fig. 6 Free energy diagram of the stepwise dealumination in H-SSZ-13, as obtained from DFT-MD umbrella simulations. The values close to the arrows show the intrinsic free energy barriers of each step with one (gray dashed line) and three (blue line) water molecules per Al atom. Reprinted with permission from Nielsen, M.; Hafreager, A.; Brogaard, R.Y.; De Wispelaere, K.; Falsig, H.; Beato, P.; Van Speybroeck, V.; Svelle, S., Collective Action of Water Molecules in Zeolite Dealumination. *Cat. Sci. Technol.* **2019**, *9*(14), 3721–3725. Copyright 2019, The Royal Society of Chemistry.

Author's personal copy

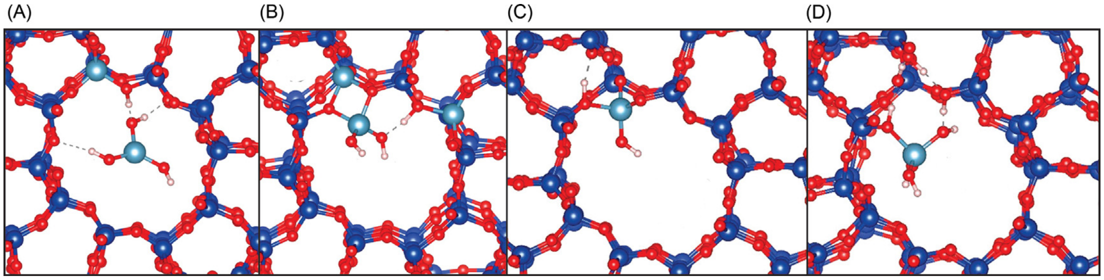

Fig. 7 DFT-optimized structures of some recently proposed (partially) hydrolyzed aluminum species, as derived from NMR measurements. (A and B) EFAL in synergistic proximity of a BAS. (C and D) Framework-associated aluminum. (A and B) Adapted with permission from Chen, K.; Abdolrahmani, M.; Horstmeier, S.; Pham, T.N.; Nguyen, V.T.; Zeets, M.; Wang, B.; Crossley, S.; White, J.L., Brønsted–Brønsted Synergies Between Framework and Noncrystalline Protons in Zeolite H-ZSM-5. *ACS Catal.* **2019**, *9*(7), 6124–6136. Copyright 2019, American Chemical Society. (C and D) Adapted with permission from Chen, K.; Horstmeier, S.; Nguyen, V.T.; Wang, B.; Crossley, S.P.; Pham, T.; Gan, Z.; Hung, I.; White, J.L., Structure and Catalytic Characterization of a Second Framework Al (IV) Site in Zeolite Catalysts Revealed by NMR at 35.2 T. *J. Am. Chem. Soc.* **2020**, *142*(16), 7514–7523. Copyright 2020, American Chemical Society.

the amount of framework-associated octahedral Al correlates with the Lewis acidity in wet H-MOR, representing a significant amount of the overall number of Lewis acid sites.[122] Tricoordinated extra-framework Al atoms with exceptional Lewis acidity have also been proposed for dealuminated HY zeolite, based on the results of NMR with trimethylphosphine as a probe molecule.[123] The true structure of framework and extra-framework Al is thus still an open question in the literature, as the rich structural variety of Al likely makes many structures possibly coexisting in the catalyst[6] (and references therein). Molecular modeling can in this case provide some useful insights. Pidko and *co*-workers proposed that the preferred state for EFAL species at reaction conditions is the polynuclear cluster $[Al_3O_4H_3]^{4+}$ in the faujasite zeolite, using a thermodynamic model coupled with the data from static DFT calculations.[11,124] These findings are, however, still waiting for experimental validation. Interestingly, the same authors also calculated that the activity towards alkane cracking of a BAS next to the polynuclear EFAL cluster is increased.[125] This increase in activity related to the synergistic proximity of BAS and EFAL species is of course deeply intertwined with the structural characterization of the EFAL itself and represents a remarkable subject of interest in the current investigation of zeolite chemistry.

A synergistic enhancement of the Brønsted acidity in the H-Y zeolite caused by proximity of EFAL species was initially proposed based on NMR evidences coupled back by DFT simulations.[126] The same authors also suggested that after hydration of the zeolite, the EFAL species tend to adopt an octahedral geometry and remain close to the framework aluminums because of strong H-bonds between the coordinating water molecules and the O atoms of the framework.[127] Very recently, moreover, technological advances in NMR spectroscopy allowed to discover a minor, very deshielded and relatively broad peak at 12–15 ppm in the ^{1}H spectrum of the H-ZSM-5 zeolite (Fig. 3).[128] Such peak was proposed to be associated with a tetrahedral or triangular planar EFAL species in direct hydrogen bonding with a BAS (Fig. 7A and B),[129] thus providing further evidence for a widespread proximity between framework and extra-framework aluminum.

In conclusion, the past depiction of zeolite active sites as well-defined framework-bound protons has been deeply challenged in the last decades and a new picture of the catalyst, with a more complex chemistry has emerged. Not only the BAS can be mobilized at typical reaction conditions, but also the framework itself has been shown to be subject to significant chemical reactivity. Unraveling the nature and catalytic activity of framework-associated and extra-framework aluminum species is nowadays a very active research field. While the positive effect of Brønsted-Lewis and Brønsted-Brønsted synergies on catalytic reactions such as the prototypical alkane H/D exchange is accepted,[7,130,131] future work will still be needed to achieve a realistic speciation of Al in zeolites at operating conditions, thereby leading to further improvement in our understanding of these fascinating materials.

6.08.2.3 Mobility of active sites in TM-exchanged zeolites

Transition metal (TM) exchanged zeolites have received significant attention over the past few decades as promising single-site catalytic materials.[38,132–134] Akin to Brønsted acid sites, as outlined in the previous section, exchanged TM sites in zeolites can mobilize under certain environmental conditions leading to divergent catalytic behavior. Arguably the most notable example is the mobilization of copper sites in chabazite during the ammonia assisted selective catalytic reduction of nitrous oxides (NH_3-SCR-NO_x, Fig. 8), where summaries of key spectroscopic, kinetic and theoretical studies investigating this phenomena constitute the bulk of this section. It should be noted that while the role of mobilized Cu ions in SCR reactivity had been implied as early as the 90s,[135] and mobility of Cu has been identified in Cu-Y and Cu-ZSM-5 systems under conditions relevant for NH_3-SCR,[136] this article focusses on the CHA topology. Other selected examples of TM site mobility are also outlined, such as Pd mobility in SSZ-13, Rh mobility in H-Y during ethene oligomerization & hydrogenation, and mobility of Ag clusters/nanoparticles in MFI during propane-assisted SCR reactivity. These are only a few examples which clearly show the dynamic rearrangements of TM-exchanged zeolites, however, based on these cases, it is clear that dynamic evolution of active sites is a much more general concept within the field of zeolite catalysis.

Author's personal copy

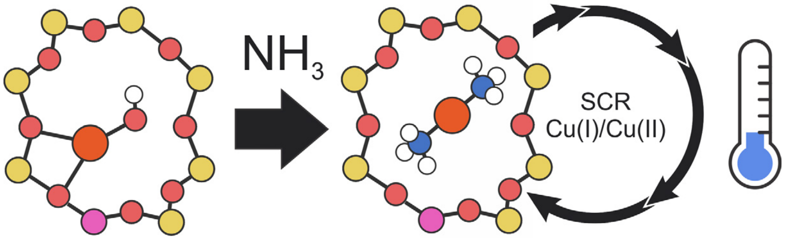

Fig. 8 Illustration of mobilization of cationic Cu sites in the low-temperature ammonia-assisted selective catalytic reduction of NO_x, catalyzed by Copper-exchanged chabazites. Cu = orange, Si = yellow, O = red, Al = purple, H = white.

6.08.2.3.1 Mobility of copper sites in Cu-CHA during low-temperature NH_3-SCR-NO_x

NH_3-SCR-NO_x is a widely employed process in the global effort to combat high NO_x emissions from industry and vehicle use, given the well-documented health impacts these gasses can cause if they remain largely abundant in the atmosphere.[137] Metal-exchanged zeolites are well-studied materials for this purpose,[138–140] offering efficient and robust catalytic systems that are less toxic than industrial vanadium-based catalysts such as V_2O_5-WO_3/TiO_2.[141]

NH_3-SCR reactivity in zeolites can be categorized into three subtypes:

(i) Standard SCR, in which NO is exclusively consumed upon reduction with NH_3 and O_2

$$4NO + O_2 + 4NH_3 \rightarrow 4N_2 + 6H_2O$$

(ii) Fast SCR, in which both NO and NO_2 are consumed in equal quantities:

$$NO + NO_2 + 2NH_3 \rightarrow 2N_2 + 3H_2O$$

(iii) NO_2 SCR, in which NO_2 is reduced exclusively upon reduction with NH_3:

$$2NO_2 + 2NH_3 \rightarrow 2N_2 + N_2O + 3H_2O$$

$$6NO_2 + 8NH_3 \rightarrow 7N_2 + 12H_2O$$

Copper-exchanged zeolites in particular have received significant attention for their propensity to facilitate "standard NH_3-SCR" (in which NO is exclusively consumed upon reduction with NH_3 and O_2). Initial discoveries in the 1970s utilized faujasite (zeolite Y),[142] and in the 1980s seminal work by Iwamoto and coworkers had identified Cu-SZM-5 as suitable catalysts for SCR reactivity.[143–146] However, more recent reports emerged in the early 2010s outlining that Cu-exchanged chabazites, i.e., SSZ-13 and SAPO-34, are superior catalysts with greater catalytic efficacy[147] and hydrothermal stability,[148] and as a result Cu-SSZ-13 is now widely used in the commercial treatment of diesel engine emmisions.[136,140] Despite these significant advances in the development of Cu-CHA catalytic systems, the speciation and nature of the active copper sites during NH_3-SCR reactivity is not entirely resolved and is an active area of research in its own right.[42] While this speciation is dependent on physiochemical factors such as gas-feed composition, temperature and also the framework composition itself such as the Si/Al ratio, cationic Cu-exchange has been shown to prevalently take place in which ions are anchored to 6-ring and 8-ring sites as Cu(I), Cu(II) and $[CuOH]^+$ species (**Fig. 9**).[149,150] Herein, a selection of key papers are outlined that elucidate the mobilization of these Cu catalytic sites during NH3-SCR-NOx reactivity, highlighting the importance of *operando* experimental and modeling techniques in unraveling this phenomenon.

6.08.2.3.1.1 Identification of catalytically relevant mobile $[Cu(NH_3)_2]^+$ under low-temperature standard SCR

Following initial reports identifying the catalytic capabilities of Cu-CHA, in situ studies revealed that solvation of Cu sites with ligating probe molecules can liberate them from the framework. Kwak et al. employed H_2-temperature programmed reduction (TPR) and FTIR to probe the nature of the cationic copper sites in Cu-SSZ-13, identifying that addition of H_2O (1%) into the H_2 gas stream significantly altered the reduction profiles, interpreted as the Cu sites moving from their original positions anchored to the framework upon H_2O-solvation. [151] Gao and coworkers probed Cu-SSZ-13 under conditions of NO oxidation, NH_3 oxidation and NH_3-SCR conditions using EPR spectroscopy and TPR studies,[152] finding that prior to full dehydration of the sample hydrated Cu(II) species were present and mobile, as indicated by multiple EPR spectroscopic features identified at the high-field, and low-field hyperfine structures being partially shielded. The lack of these features at higher temperature (250 °C) dehydrating conditions indicated that Cu ions are conversely immobile. The work of Gao and coworkers also provided some key evidence for the presence of transient dimers under low-temperature SCR conditions, which will be covered in **Section 6.08.3.2.4**. Szanyi and coworkers employed TP-XRD, XANES and vibrational (DRIFTS) spectroscopy to probe changes in the copper coordination environment in Cu-SSZ-13 during calcination, reduction with CO, and adsorption of CO and H_2O.[153] DRIFTS particularly proved to be a useful technique, where, for instance the adsorption of CO to form $[Cu(CO)_2]^+$ complexes at temperatures below 100 °C could be seen to alter the Cu influence on the asymmetric T-O-T (ν_{asym}(TOT)) region of the IR spectra. Solvation of Cu(II) sites by NH_3 was also identified by Beale and coworkers in combined theoretical and in situ FTIR studies.[154] At 250 °C, three distinct NH_3

Author's personal copy

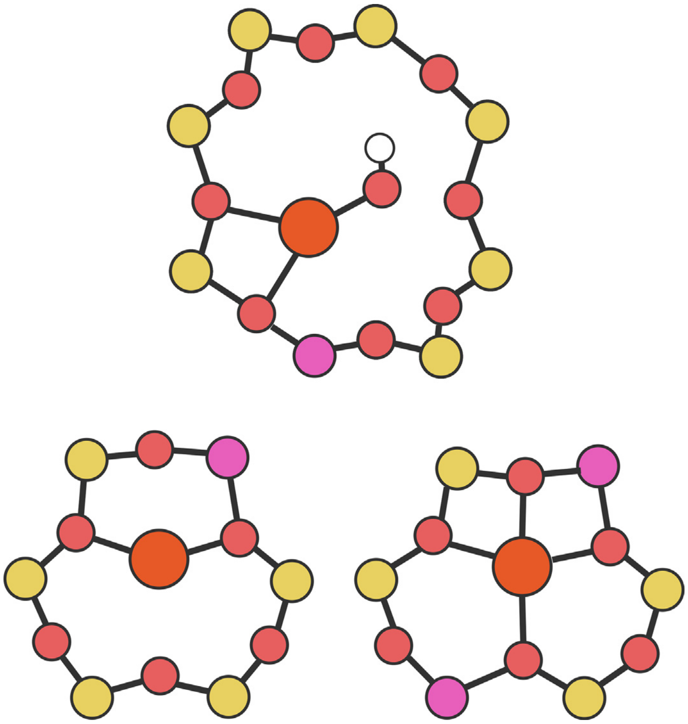

Fig. 9 Spectroscopically and computationally characterized locations of Cu(I) and Cu(II) ions at 6mr and 8mr rings upon cation-exchange. Cu = orange, Si = yellow, O = red, Al = purple, H = white.

species were identified, where one of which, a $[Cu(NH_3)_4]^{2+}$ complex, could be confirmed via FTIR with observation of frequencies in the 3100–3400 cm^{-1} range, at 1619 cm^{-1} and at 1278 cm^{-1}, which correspond to different contributing NH_3 vibrational modes. Theoretical absorbance bands obtained via Fourier-based analysis of AIMD simulations agreed with experimental bands and further supported formation of $[Cu(NH_3)_4]^{2+}$. Further PD, XAS and DFT studies by Beale and coworkers supported formation of untethered Cu species upon NH_3-solvation at room temperature.[155] For example, peaks at ~2.0 Å and >2.50 Å in the Cu K-edge k^3-weighted EXAFS spectra fit with a N coordination number of 4 and Cu-N distance of 2.04 Å, and a N coordination number of 2 with a distance of 2.71 Å, consistent with a liberated $[Cu(NH_3)_6]^{2+}$ species residing in the center of the cha cage. FTIR, XANES, XES and DFT studies by Bordiga and coworkers[156] also showed that NH_3 adsorption can result in the reduction of Cu(II) to Cu(I) with emergence of the 8982.5 eV peak in the XANES spectra (**Fig. 10**A), which, along with a high intensity of this peak, suggested a linear species in the form of O_{fw}—$Cu(NH_3)$ (bound to one oxygen of the zeolite) or $[Cu(NH_3)_2]^+$. This was reflected in DFT calculations on cluster models (PBE/TZVP level) where one equivalent drives the Cu out of the 6mr plane during structure optimization, while two form mobilized $[Cu(NH_3)_2]^+$ (**Fig. 10**C and D).

While the studies outlined above demonstrate that adsorbates such as H_2O, CO, NH_3 can liberate the cationic Cu sites, the conditions were not altogether identical to those during NH_3-SCR-NO_x. Subsequent studies featuring *operando* spectroscopic techniques with complementary ab initio calculations could instead evaluate the speciation of Cu under conditions more explicitly comparable to NH_3-SCR-NO_x, and a selection of these are summarized below.

Schneider and Gounder interrogated the speciation of Cu under various ex situ and in situ conditions in samples of Cu-SSZ-13, in which the 6-rings contain either 1 aluminum (1Al) or two (2Al), via XAS, static DFT and DFT-MD.[157] Analysis under ex situ conditions indicated that Cu(II) preferentially populates the 2Al 6-ring sites to form "Z_2Cu(II)" and at 1Al 6-ring sites to form "ZCuOH," and under hydrating conditions Cu sites can mobilize via solvated copper aqua complexes, consistent with reports summarized previously. Exposure to a subset of catalytic conditions of 300 pm NO and NH_3 at 473 K reduces all copper sites to Cu(I), where XANES was fitted to a Cu(I) fraction of 100%. AIMD simulations of $Z[Cu(NH_3)_2]/[ZNH_4]$ and $Z[Cu(NH_3)_2]$ systems revealed the $[Cu(NH_3)_2]^+$ species are highly mobile (**Fig. 11**), while XAS analysis found that a lone peak at 1.89 Å in the EXAFS region fits to a coordination number of 2 with respect to N or O. Conversely, analysis of samples with an oxidizing feed of 300 pm NH_3 and 10% O_2 indicated formation of $[Cu(NH_3)_4]^{2+}$ complexes that are ~50% less mobile than $[Cu(NH_3)_2]^+$. *Operando* EXAFS measurements on a Si:Al = 25, Cu:Al = 0.42 sample revealed a 60:40 Cu(I)/Cu(II) ratio, a lack of second-shell structure and a fit of 3.1 with respect to the CN, consistent with an admixture of $[Cu(NH_3)_2]^+/[Cu(NH_3)_4]^{2+}$, further evidencing that Cu sites are solvated and mobilized under catalytic conditions.

Characterization of the active sites at Cu-SSZ-13 under NH_3-SCR-NO_x conditions between 150 °C and 400 °C was also undertaken by Bordiga and coworkers via *operando* XANES, XAS and vtc-XES.[158] For reference, spectra of Cu(I) and Cu(II) aqua/amino complexes were obtained for linear combination fit (LCF) analyses. At low-temperature conditions (150 °C) the XANES region

Author's personal copy

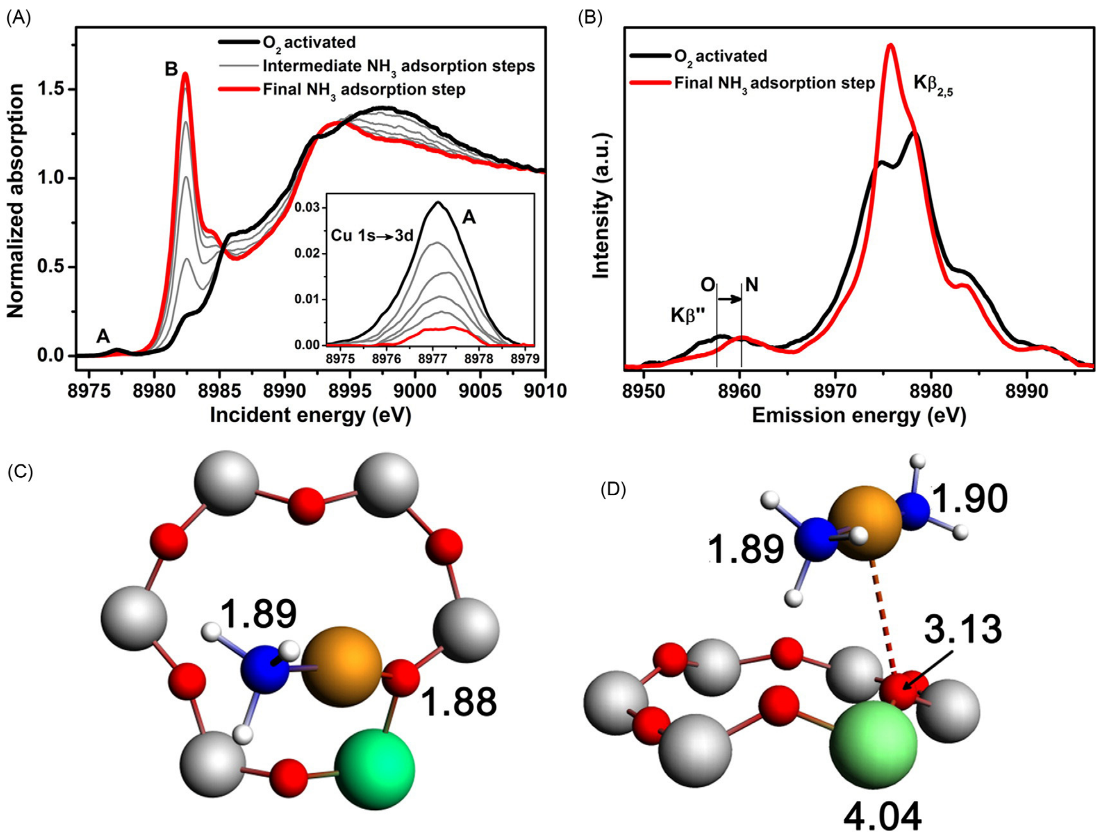

Fig. 10 (A) Evolution of the Cu K-edge XANES spectra of Cu-SSZ-13 with O_2/He and a 1300 pm gas-feed of NH_3 (in He) at 120 °C. Inset: pre-edge region. (B) Cu $K\beta_{2.5}$ and $K\beta''$ emission lines for initial and final states after exposure to NH_3. (C and D) Local 6mr environment of the DFT-optimized zeolite clusters upon exposure to one (C) or two (D) equivalents of NH_3 to Cu, computed at the PBE/TZVP level. Reprinted with permission from Giordanino, F.; Borfecchia, E.; Lomachenko, K.A.; Lazzarini, A.; Agostini, G.; Gallo, E.; Soldatov, A.V.; Beato, P.; Bordiga, S.; Lamberti, C., Interaction of NH3 With Cu-SSZ-13 Catalyst: A Complementary FTIR, XANES, and XES Study. *J. Phys. Chem. Lett.* **2014**, *5*(9), 1552–1559, with permission from the American Chemical Society.

was consistent with spectra obtained by Schneider and coworkers,[157] and LCF analyses identified an admixture of 46% $[Cu(NH_3)_2]^+$, 25% $[Cu(NH_3)_4]^{2+}$ and 26% remaining zeolite-bound Cu(II) species in the sample. The existence of mobilized Cu species could be validated via analysis of FT-EXAFS spectra, in which the second-shell region of ~2.3 Å (a fingerprint for framework-bound Cu species) is perturbed at lower temperatures (**Fig. 12**), while at higher temperatures this peak is present and agrees well with reference Z-Cu(II) spectra, thus identifying a temperature-dependence of Cu mobility.

Boronat and coworkers employed ab initio MD simulations, static DFT calculations and IR spectroscopy to probe the dynamic nature of copper mobility in Cu-SSZ-13 and Cu-SAPO-34 during NH_3-SCR.[159] AIMD simulations at 298 K and 523 K on unit cells featuring different gas feed adsorbates (NO, O_2, NO_2, NH_3) were performed to probe changes in the copper coordination mode (**Fig. 13**A). NH_3 could be seen to mobilize the Cu ions to form $[Cu(NH_3)_2]^+$, while NO, NO_2 and O_2 only mildly displaced Cu from the 6-ring, as shown by RMSD analysis of Cu positions in each simulation (**Fig. 13**B).

IR spectra recorded for Cu(I) and Cu(II) states in Cu-SAPO-34 samples with different catalytically relevant feeds at low- and high-temperatures also unraveled a dynamic nature of copper mobility (**Fig. 14**). In the initial Cu(I) state ν(TOT) vibrations in the 800–1000 cm^{-1} region disappear upon exposure to NH_3 at lower-temperatures, and reemerge at high temperatures (623 K). With an initial Cu(II) state and a gas feed ratio of 5:2:1 O_2:NO:Cu, the ν_{asym}(TOT) fingerprint remains throughout the 298–623 K temperature range, and only when NH_3 is added to the gas feed (2:1 NH_3:Cu) at 423 K the ν(TOT) fingerprint disappears again, in which complementary analysis of EXAFS identifies this is concomitant with Cu(II) → Cu(I) reduction.

6.08.2.3.1.2 The role of mobilized copper in the oxidation half-cycle during NH_3-SCR-NO_x

With the identification of mobilized $[Cu(NH_3)_2]^+$ species forming under low-temperature catalytic conditions, their role in the Cu(I) → Cu(II) oxidation half-cycle during NH_3-SCR-NO_x was not immediately clear. As previously discussed, Gao and coworkers employed kinetics studies and EPR measurements to probe Cu-SSZ-13 and identified highly mobile hydrated Cu species,[152] where in samples with low to intermediate cationic copper loadings (Cu/Al ≤ 0.22), transient dimeric Cu species were identified to form under catalytic conditions via interaction of pairs of $[Cu(NH_3)_2]^+$, as indicated by a quadratic dependence on Cu site density on the SCR rate. Moreover, EPR spectroscopic features were consistent with dipolar interactions between Cu(II) ions. In a subsequent

Author's personal copy

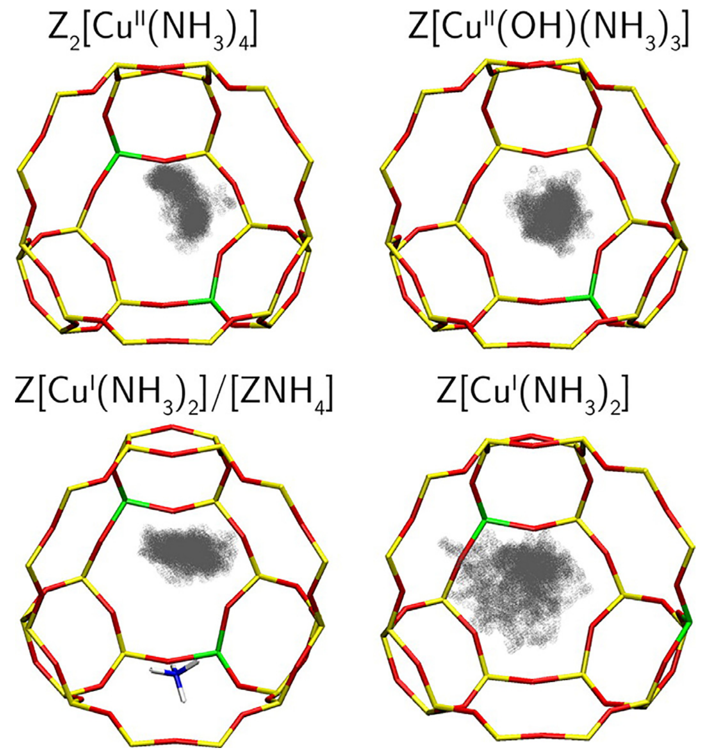

Fig. 11 Copper cation positions (shown as gray balls) inside the SSZ-13 cage across 90 ps AIMD simulations. Reprinted from Paolucci, C.; Parekh, A.A.; Khurana, I.; Di Iorio, J. R.; Li, H.; Albarracin Caballero, J.D.; Shih, A.J.; Anggara, T.; Delgass, W.N.; Miller, J.T.; Ribeiro, F.H.; Gounder, R.; Schneider, W.F., Catalysis in a Cage: Condition-Dependent Speciation and Dynamics of Exchanged Cu Cations in SSZ-13 Zeolites. *J. Am. Chem. Soc.* **2016**, *138*(18), 6028–6048, with permission from the American Chemical Society.

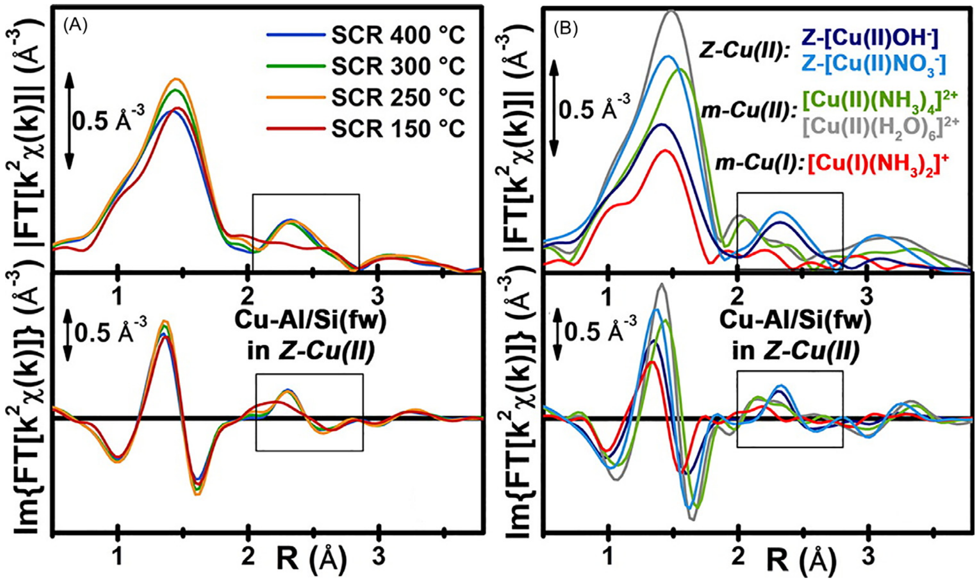

Fig. 12 (A) FT-EXAFS spectra (top: moduli, bottom: imaginary parts of the Fourier transform) of the Cu-SSZ-13 sample collected during SCR reaction conditions at a range of temperatures. (B) FT-EXAFS spectra of references employed for analysis of the *operando* spectra, i.e., via LCF, by Borfecchia and coworkers. Reprinted from Lomachenko, K.A.; Borfecchia, E.; Negri, C.; Berlier, G.; Lamberti, C.; Beato, P.; Falsig, H.; Bordiga, S., The Cu-CHA deNOx Catalyst in Action: Temperature-Dependent NH3-Assisted Selective Catalytic Reduction Monitored by Operando XAS and XES. *J. Am. Chem. Soc.* **2016**, *138*(37), 12025–12028, with permission from the American Chemical Society.

Author's personal copy

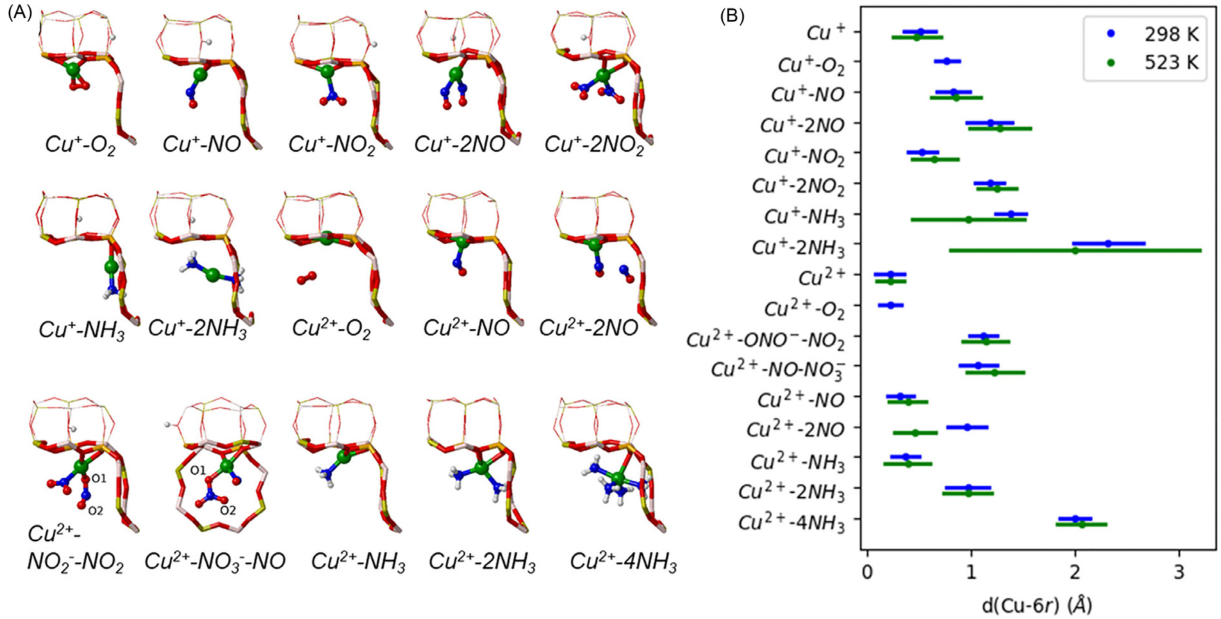

Fig. 13 (A) Snapshots of Cu(I) and Cu(II) cationic species at the 6mr in Cu-SAPO-34 with probe adsorbates (labeled below each structure), which were generally most visited during 100 ps AIMD runs at 298 K. (B) Average and RMSD distances of the Cu cations traveled from the 6mr at 298 K (blue) and 523 K (green). Reprinted from Millan, R.; Cnudde, P.; Hoffman, A.E.J.; Lopes, C.W.; Concepción, P.; van Speybroeck, V.; Boronat, M., Theoretical and Spectroscopic Evidence of the Dynamic Nature of Copper Active Sites in Cu-CHA Catalysts under Selective Catalytic Reduction (NH3–SCR–NOx) Conditions. *J. Phys. Chem. Lett.* **2020**, *11*, 10060–10066, with permission from the American Chemical Society.

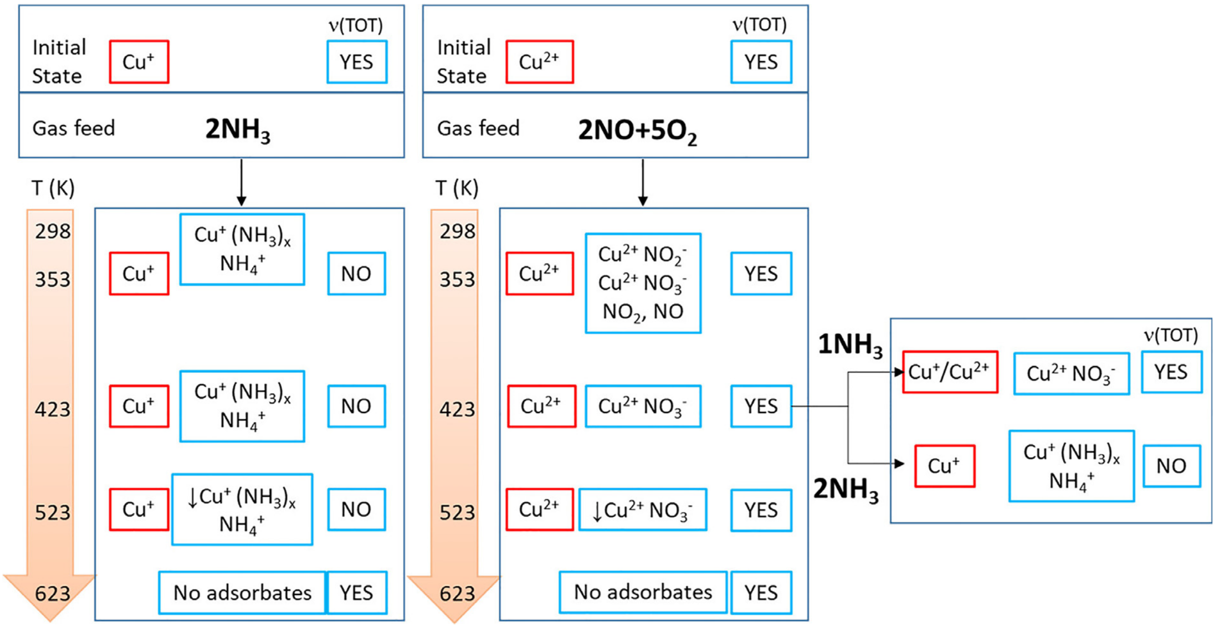

Fig. 14 Flow chart summarizing the oxidation states of cationic Cu sites (red) identified by EXAFS, the speciation of the Cu sites identified by IR (blue), and the presence of asymmetric ν(TOT) peaks as a function of temperature and gas feed in Cu-SAPO-34 (also blue). Reprinted from Millan, R.; Cnudde, P.; Hoffman, A.E.J.; Lopes, C.W.; Concepción, P.; van Speybroeck, V.; Boronat, M., Theoretical and Spectroscopic Evidence of the Dynamic Nature of Copper Active Sites in Cu-CHA Catalysts Under Selective Catalytic Reduction (NH3–SCR–NOx) Conditions. *J. Phys. Chem. Lett.* 2020, *11*, 10060–10066, with permission from the American Chemical Society.

study, Gao and coworkers also identified that the SCR rate (mol NO g^{-1} s^{-1}) was quadratically dependent on Cu/Al ratio (Fig. 15B) under low temperature conditions (200 °C), while a linear dependence is observed at 380 °C (Fig. 15A).[160] DFT calculations (PBE-D3 level) revealed that O_2 activation proceeds most accessibly with participation of two $[Cu(NH_3)_2]^+$ complexes to form bridged $[Cu(NH_3)_2]$-O_2-$[Cu(NH_3)_2]$ species rather than activation over an individual $[Cu(NH_3)_2]^+$ complex. Cu(I) oxidation at the bridged

Author's personal copy

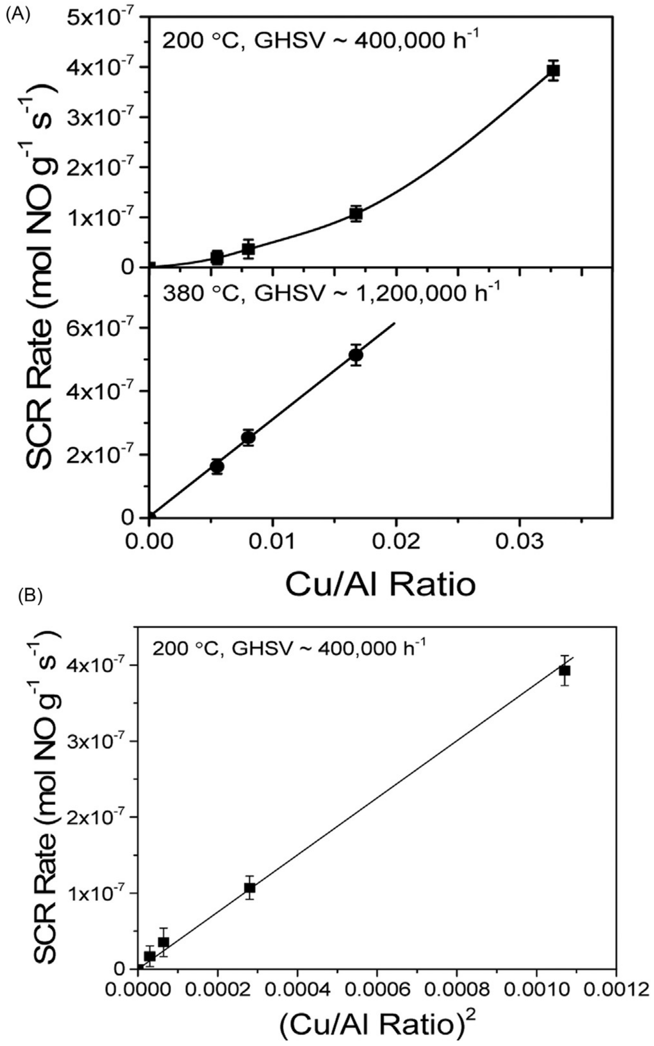

Fig. 15 (A) SCR rate (mol NO g^{-1} s^{-1}) against Cu/Al ratio at 200 °C (top) and 380 °C (lower). (B) SCR rate against $(Cu/Al)^2$. Reprinted from Gao, F.; Mei, D.; Wang, Y.; Szanyi, J.; Peden, C.H.F., Selective Catalytic Reduction Over Cu/SSZ-13: Linking Homo- and Heterogeneous Catalysis. *J. Am. Chem. Soc.* **2017**, *139*(13), 4935–4942, with permission from the American Chemical Society.

species was then characterized to take place via NO addition and subsequent NO_2 release to afford $[(NH_3)_2\text{-Cu(II)-O-Cu(II)-}NH_3)_2]^{2+}$, followed by hydrolysis to yield $[(NH_3)_2Cu(OH)]^+$. At low Cu site densities diffusion of $[Cu(NH_3)_2]^+$ to a neighboring cage was proposed to be rate-limiting, while formation of the $[(NH_3)_2\text{-Cu(II)-O-Cu(II)-}NH_3)_2]^{2+}$ dimer is proposed as rate-limiting at higher site densities. A computed diffusion coefficient (D) for $[Cu(NH_3)_2]^+$ of 4.4×10^{-12} m^2 s^{-1} was obtained via AIMD (NVT, 200 °C, D = RMSD/6t) which supports a diffusion-controlled process at low temperatures and Cu-loadings.

Separate Cu-density dependent kinetic schemes were established by Paolucci and coworkers, where for densities over 1.9×10^{-4} $Å^{-3}$ the rate increases linearly, while at lower densities of $< 1.13 \times 10^{-4}$ $Å^{-3}$ the quadratic dependence was observed.[20] LCF analyses of Cu K-edge XANES region of different Cu-CHA samples outlined an inverse relation of Cu-Cu distance with Cu(I) fraction, providing evidence for an alternative non-single site mechanism at play whereby the rate of Cu(I) oxidation increases with greater site densities. This behavior was rationalized by an O_2-consuming step in the oxidation half-cycle being sensitive to the Cu density. Monitoring the rate of decay of Cu(I) under O_2 in samples with differing site densities via Cu K-edge XANES could also identify decay is second-order in Cu(I), implicating the following pseudobimolecular mechanism:

$$2\left[Cu(NH_3)_2\right]^+ + O_2 \rightarrow \left[(NH_3)_2Cu\text{–}O_2\text{–}Cu(NH_3)_2\right]^{2+}$$

Static DFT calculations (PBE-D2 level) on a 12-T site supercell with two $[Cu(NH_3)_2]^+$ complexes charge-compensated by 2 Al atoms, revealed that initial $[Cu(NH_3)_2]^+$ diffusion to a neighboring cage is facile with an activation barrier of 35 kJ mol^{-1}, and subsequent coordination of O_2 to the two close by Cu(I) ions is favored (-59 kJ mol^{-1}) over a single-ion binding mode (-26 kJ mol^{-1}) to form a triplet dimeric species. Spin-forbidden rearrangement to form a di-oxo structure then takes place, where

Author's personal copy

each Cu(II) ion adopts a square-planar geometry. However, to gain more accurate insight into the energetics of $[Cu(NH_3)_2]^+$ diffusion, metadynamics simulations were performed (see **Section 6.08.3.2.4**).

Recently XAS and diffuse reflectance UV-Vis-NIR spectroscopic studies have been used to further probe the structure of the $[Cu_2(NH_3)_4O_2]^{2+}$ species.[161] A starting state of mobilized $[Cu(NH_3)_2]^+$ could be formed via exposure of pre-treated Cu-CHA to 1000 pm NO and 1000 pm NH_3 at 200 °C and confirmed by the 8982.5 eV fingerprint in the Cu K-edge EXAFS spectra. Exposure of this sample to O_2 (10% in He) revealed an almost complete disappearance of the fingerprint, indicating the oxidation of most $[Cu(NH_3)_2]^+$ species. This was further supported by UV-Vis-NIR with a red-shift of the ligand-to-metal charge transfer (LMCT) peak from 35 k to 25 k, along with emergence of a d-d absorption peak at 13850 cm^{-1}. Signals in the NIR region (6515 cm^{-1} and 4970 cm^{-1}) arising from combination modes of NH_3 and NH_4^+, also indicated NH_3 is still ligated to the oxidized Cu(II) sites. The precise structure of this state was probed by fitting of the FT-EXAFS spectra against gas-phase DFT structures (M06-HF-D3/Def2-TZVP level), and the best fit obtained supported a side-on μ-η^2,η^2-peroxo diamino dicopper(II) species $[Cu_2(NH_3)_4O_2]^{2+}$ (**Fig. 16**A(iii)) over an end-on trans μ-1,2-peroxo binding mode (**Fig. 16**A(ii)). Subsequent exposure of the sample featuring $[Cu_2(NH_3)_2O_2]^{2+}$ to NH_3 shows a partial re-emergence of the 8982.5 eV peak, rationalized by partial reformation of monomeric $[Cu(NH_3)_2]^+$, while in the UV-Vis-NIR spectrum a shift from 13,800–14,400 cm^{-1} and a lowering in intensity also suggests some Cu(II) remains. LCF analysis of the XANES region also identified partial reduction of Cu(II) to Cu(I), with an admixture of 65% $[Cu(NH_3)_2]^+$ and 35% $[Cu(NH_3)_3(X)]^+$, which was considered to be either $[Cu(NH_3)_3(OH)]^+$, as previously predicted by Paolucci and coworkers,[157] and computationally identified by Shimizu and coworkers,[162] or $[Cu(NH_3)_3(OO)]^+$, which was proposed based on LCF analysis of the XANES region spectra. Conversely, exposure of the oxidized $[Cu_2(NH_3)_2O_2]^{2+}$ species to NO disaggregates the Cu centers along with reduction to Cu(I), as seen by the reemergence of the 8982.5 eV peak, with concomitant formation of N_2. UV-Vis-NIR spectra shows the minimization of the intensity of the 13,850 cm^{-1} peak corresponding to $[Cu_2(NH_3)_2O_2]^{2+}$ and emergence of a series of peaks at around 20,000, 16,350, 13,300 and 10,600 cm^{-1}. The Cu K-edge XANES region of the XAS spectra is also consistent with a $Z[Cu(NH_3)]$ species (**Fig. 16**B(ii)).

The aforementioned *operando* studies identifying the role of mobile $[Cu(NH_3)_2]^+$ and resulting dimeric $[Cu(NH_3)_2O_2]^{2+}$ in the low-temperature NH_3-SCR pathway can inform new proposals of full catalytic cycles for the low-temperature NH_3-SCR-NO_x pathway. Moreover, as transient intermediates can be unidentifiable, even via *operando* spectroscopic techniques, DFT calculations can fill in the gaps, serving to provide insight in proposing a complete mechanism for such an intriguing reaction. A recent example of the application of DFT to provide a full working catalytic cycle of NH_3-SCR-NO_x is by Grönbeck and coworkers.[163] Calculations at the PBE + U-D3 (a LOT which the authors identified as a strong performer based on prior benchmarking studies)[164], revealed

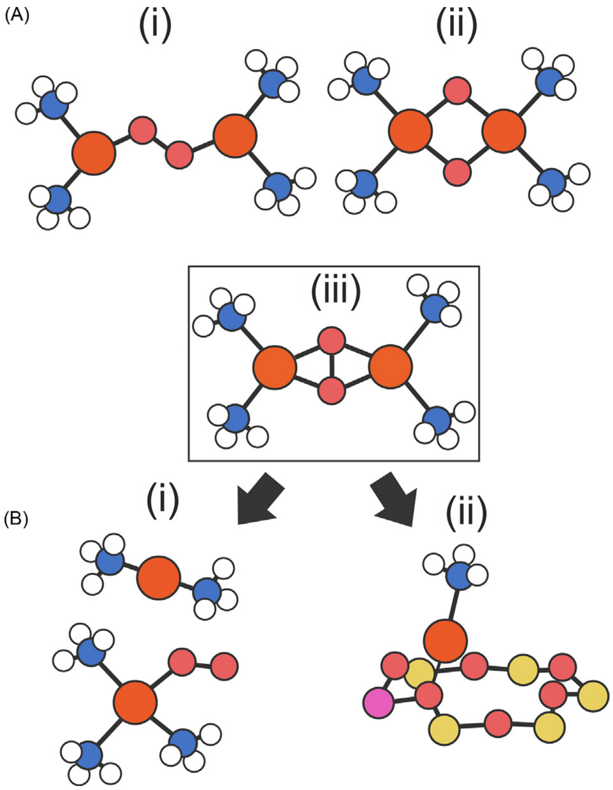

Fig. 16 (A) Forms of $[Cu(NH_3)_2O_2]^{2+}$ proposed and considered in the study by Berlier and coworkers: (i) trans-μ-1,2-peroxo diamino dicopper(II), (ii) bis-μ-oxo diamino dicopper(III), and (iii) μ-η^2,η^2-peroxo diamino dicopper(II), supported by fitting against *operando* XAS measurements. (B) Proposed products of (i) NH_3 addition and (ii) NO addition to μ-η^2,η^2-peroxo diamino dicopper(II).

Author's personal copy

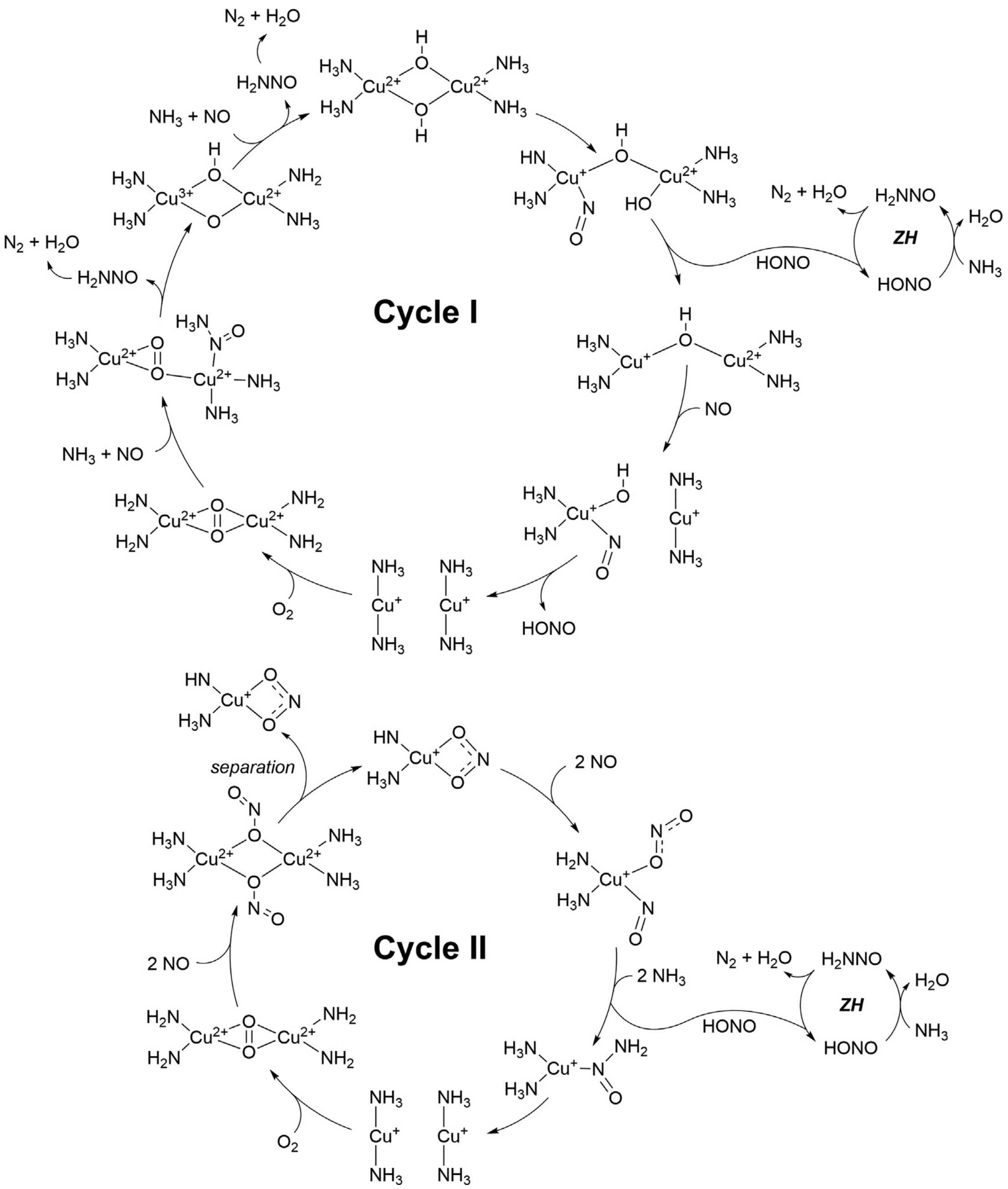

Fig. 17 Two catalyst cycles proposed and characterized with DFT at the PBE+U-D3 level, by Grönbeck and coworkers, differing in the binding mode of NO at the oxidized $[Cu_2(NH_3)_4(O_2)]^{2+}$ species.

initial activation of O_2 at a mobilized $[Cu(NH_3)_2]^+$ pair takes place to form the μ-η^2,η^2-peroxo dimer, supporting the work of Berlier and coworkers.[161] Two divergent cycles were characterized based on the initial binding mode of NO to the resulting dimer (Fig. 17).

Cycle I considers NO coordination at Cu^{2+} and subsequent NH_3 addition to form a $NONH_3$ ligated complex. The overall formation of this $[Cu_2(NH_3)_4(O_2)(NONH_3)]^{2+}$ species from $[Cu(NH_3)_2]^+$ monomers is turnover-limiting. Proton transfer from the -NH_3 moiety can then take place to release H_2NNO and form a bridging ^-OH group, where H_2NNO decomposes to N_2 and H_2O upon diffusion from the Cu sites to an available Bronsted acid site. The process of NO + NH_3 uptake to release H_2NNO is repeated to form a bridged hydroxide dimer, upon which further addition of NO and final release of HONO can complete the cycle. Cycle II conversely begins with NO binding to O_2 to form a $[Cu(NO_2)_2(NH_3)_2]^{2+}$ species, upon which Cu separation takes place to form $[Cu(NH_3)_2(NO_2)]^+$ pairs. At each Cu site addition of NO and NH_3, followed by release of H_2NNO then takes place, where formation of HONO and H_2NNO is turnover-limiting.

Author's personal copy

6.08.2.3.2 Solvation and mobility of Pd in SSZ-13

Much like in Cu-CHA, palladium sites in SSZ-13 have also been recently identified to mobilize under hydrating conditions by Paolucci et al. via combined in situ spectroscopic, kinetics and theoretical studies.[165] Ab initio thermodynamic analysis of a series of candidate "Z[PdH_XO_Y]" species was carried out at the HSE06-D3(BJ) level at two separate temperature regimes (298 K and 773 K). This identified that at lower temperatures Pd(II) sites preferentially form $[Pd(H_2O)_4]^{2+}$ under hydrating conditions in the chabazite cages, while framework-coordinated $Z_2Pd(II)$ at 6-ring sites featuring two Al-substitutions is preferred at higher temperatures (**Fig. 18**). This temperature-dependent mobilization of Pd, analogous to Cu mobilization outlined in the previous section, was supported by in situ XAS experiments, where the XANES region of Pd-SSZ-13 exposed to 10% O_2 and 3.1% H_2O at 473 K agreed with reference homogeneous aqueous Pd(II) spectra. Moreover CO oxidation was more amenable at the low-temperature hydrating conditions, implicating the role of mobilized H_2O-solvated Pd species in other Pd-zeolite catalytic transformations in hydrating conditions, such as the Wacker oxidation process. [166,167]

6.08.2.3.3 Mobility of Rh in zeolite Y and consequences for ethene hydrogenation & oligomerization

Rh-exchanged zeolites have been studied for both ethylene oligomerization and hydrogenation, with efforts tracing back to the 1970s in which Rh-Y was employed for this purpose[168–170] with more recent efforts by Gates have also focusing on Rh-Y for ethene dimerizations.[171,172] As part of this line of research, in 2011 Gates identified that the speciation of Rhodium in cation-exchanged Rh-Y can interconvert between monomeric $Rh(C_2H_4)_2$ sites, and small-clustered Rh_n sites based on the ratio of H_2:C_2H_4 in the gas feed, thus revealing a mobility of Rh sites during an interconvertible speciation process.[22] Reaction of $Rh(C_2H_4)_2(acac)$ with dealuminated zeolite HY (Si/Al = 30) afforded spatially uniform and well-defined $Rh(C_2H_4)$ sites anchored via two Rh—O bonds, supported by IR and EXAFS measurements, where IR spectra revealed that ~25% of the Bronsted acid sites are Rh-exchanged.

Upon exposure of the Rh-Y sample to a flow of H_2 at room temperature, small Rh clusters formed, as evidenced by EXAFS measurements, which fitted to a Rh-Rh coordination number of 1.9. Moreover the Rh-O coordination number remained unaffected, indicating that the clusters are anchored to the zeolite framework. This identified that disengagement and mobilization of Rh sites *en route* to cluster formation can take place by tuning the gas feed composition. The Rh-Y sample was then probed for its catalytic efficacy in ethene hydrogenation and oligomerization as a function of C_2H_4:H_2 ratio in the gas feed, with rates of ethane (hydrogenation) and butane (oligomerization) formation measured (**Fig. 19**, top) along with *operando* FT-EXAFS spectra, where cycles of (1) C_2H_4-rich, (2) H_2-rich, (3) pure H_2 and (4) H_2-rich again were used in the gas feed tuning procedure. As a result, changes in the product selectivity and magnitudes of the FT-EXAFS spectra were seen, indicating changes from monomeric to multinuclear clusters were coinciding with changes in selectivity towards oligomerization or hydrogenation.

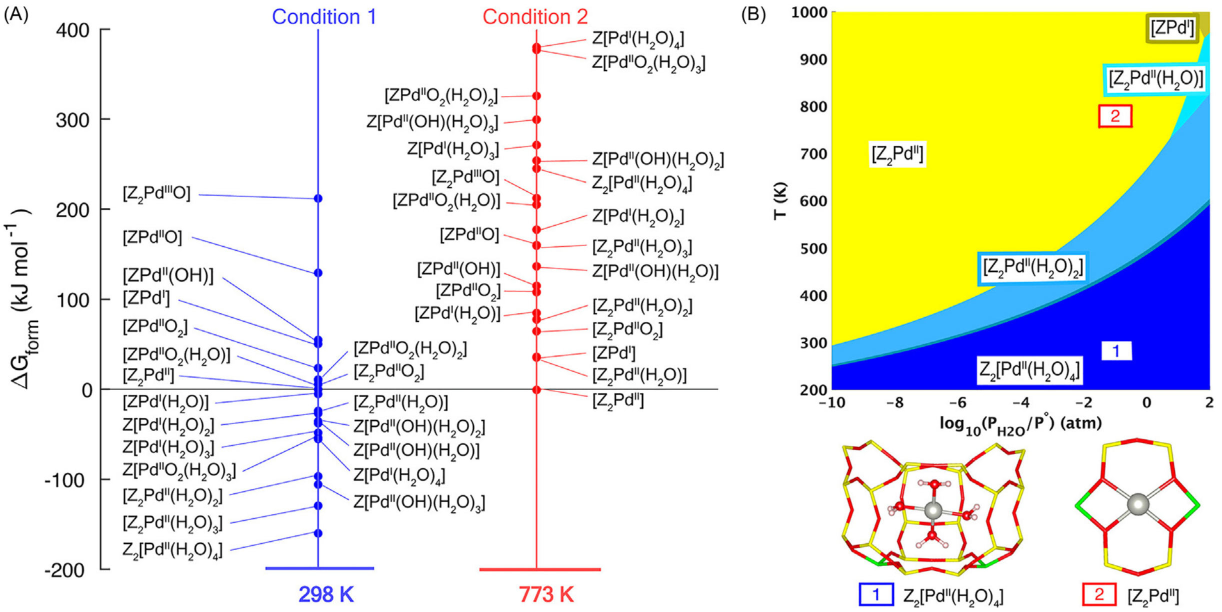

Fig. 18 (A) Computed free energies (HSE06-D3(BJ) level) of various "[$ZPd(H_xO_y)_z$]" states of Pd-speciation at 298 K (blue) and 773 K (red). (B) Phase diagram of Pd-speciation as a function of temperature & pressure constructed via ab initio thermodynamic analysis, showing the preference for solvated $[Pd(NH_3)_4]^{2+}$ species at low-temperatures (cobalt blue) to a preference for framework-anchored $Z_2Pd(II)$ species at higher-temperatures (yellow). Reprinted from Mandal, K.; Gu, Y.; Westendorff, K.S.; Li, S.; Pihl, J.A.; Grabow, L.C.; Epling, W.S.; Paolucci, C., Condition-Dependent Pd Speciation and NO Adsorption in Pd/Zeolites. *ACS Catal.* **2020**, *10*(21), 12801–12818.

Author's personal copy

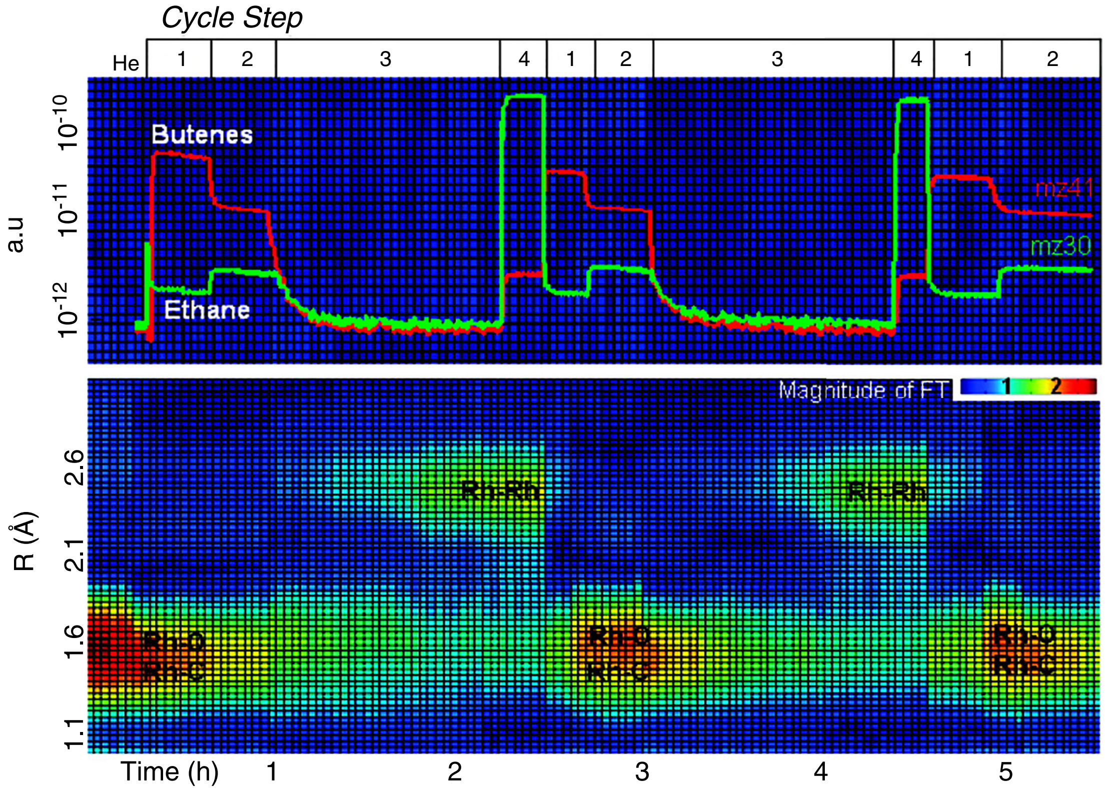

Fig. 19 (Top) Changes in selectivity towards butanes (red line) and ethane (green) formation catalyzed by $Rh(C_2H_4)_2$ supported in zeolite HY, and (bottom) time-resolved Fourier-transform (FT)-k^3-weighted EXAFS data, outlining the evolution of the magnitude of the FT over time (bottom X-axis) and composition feed-cycles (top X-axis). Reprinted from Serna, P.; Gates, B.C., Zeolite-Supported Rhodium Complexes and Clusters: Switching Catalytic Selectivity by Controlling Structures of Essentially Molecular Species. *J. Am. Chem. Soc.* **2011**, *133*(13), 4714–4717, with permission from the American Chemical Society.

6.08.2.3.4 Mobility of Ag sites in MFI during C_3H_8-SCR reactivity

Another example of mobility and clustering of active TM sites under reductive conditions, leading to subsequent consequences for propane-assisted SCR (C_3H_8-SCR) of NO was identified in Ag-MFI by Shibata and coworkers.[173,174] Under 673 K the rate of C_3H_8-SCR catalyzed by Ag-MFI-58 was significantly enhanced by the addition of H_2, where a maximum NO conversion of 48% was seen at 573 K in the presence of 0.5% H_2, and a lower ~10% conversion was measured in the absence of 0.5 H_2 (Fig. 20).[174] This enhanced reactivity assisted by exposure to H_2 was shown to be reversible, where upon H_2 addition and complementary increased NO conversion rates, removal of H_2 suppresses C_3H_8-SCR to levels observed prior to H_2 addition (Fig. 20).

The speciation of the cationic Ag(I) sites in both the presence and absence of H_2 was then probed via UV-Vis spectroscopy. Upon exposure of the sample to H_2, bands at ~260 and ~284 nm emerged, which, based on comparison with other UV-Vis characterizations of Ag clusters,[175–180] was assigned as Ag_n^+ clusters ($2 \leq n \leq 4$). Subsequent treatment of the H_2 addition sample under C_3H_8-SCR conditions in the absence of H_2 led to these Ag_n^+ signals to disappear. Assuming cationic monomeric Ag(I) sites are framework bound in Ag-MFI-58 in the absence of H_2, this revealed that H_2 exposure mobilizes the Ag cations to form cationic Ag_n^+ clusters. Further assessment of the rate of C_3H_8-SCR in a range of samples with varying Ag/Al ratios also identified that in the presence of H_2 an increase in Ag/Al ratio increases the NO conversion to N_2 with a reaction order above 1, thus supporting the notion that the cationic Ag_n^+ clusters, reversibly formed upon H_2-induced mobilization of Ag sites, are the catalytically active species in the C_3H_8-SCR process. Based on kinetic analyses of Ag(I) reduction to Ag_2^+ by H_2-TPR studies, reported previously in Ag-CHA by Beyer and coworkers,[181] the authors proposed that the following mechanism is taking place to form the Ag_n^+ clusters:

$$H_2 \rightleftharpoons 2H \ (X)$$

$$H + Ag(I) \rightleftharpoons [AgH]^+ \ (Y)$$

$$[AgH]^+ + Ag(I) \rightleftharpoons Ag_2^+ + H^+ \ (Z)$$

Subsequently Shimizu and coworkers extensively probed the structure and nature of these identified Ag clusters by a combination of H_2-TPR, XRD, UV-Vis, and Ag K-edge EXAFS studies.[173] The H_2-TPR results at Ag-MFI-58 revealed two peaks of H_2 consumption, which combined with XRD studies indicated that all Ag^+ cations first reduce to small clusters, followed by further aggregation

Author's personal copy

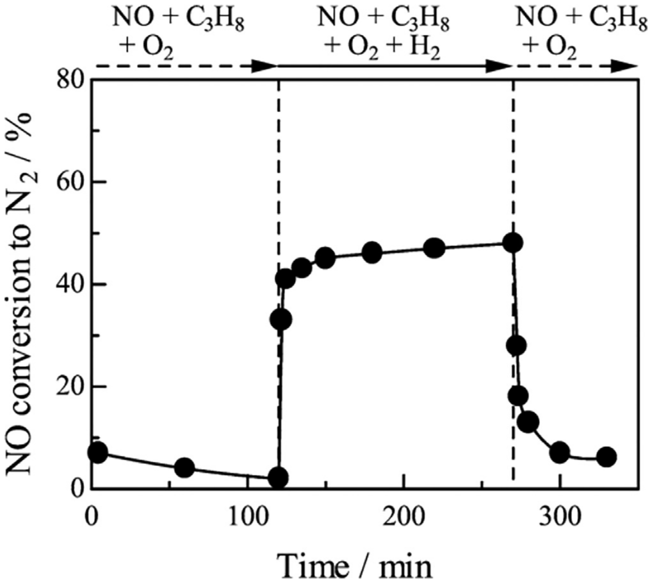

Fig. 20 Time evolution of C_3H_8-SCR of NO in Ag-MFI-58 in both the presence and absence of H_2. Reprinted from Shibata, J.; Takada, Y.; Shichi, A.; Satokawa, S.; Satsuma, A.; Hattori, T., Ag Cluster as Active Species for SCR of NO by Propane in the Presence of Hydrogen Over Ag-MFI. *J. Catal.* **2004**, *222*(2), 368–376, with permission from Elsevier.

Table 2 Curve-fitting analysis of FT-EXAFS for a range of Ag samples.

Samples	*Scatter atom*	*N*	*r (Å)*
Ag-MFI(22)-48	Ag	1.3	2.71
Ag-MFI(22)-58	Ag	1.9	2.73
Ag-MFI(13)-30	Ag	1.0	2.72
Ag-MFI(7.7)-33	O	0.9	2.11
Ag-MFI(22)-58[a]	Ag	3.3	2.73
Ag foil[b]	Ag	12	2.89
Ag_2O[b]	O	2	2.04

[a] Measured after H_2 treatment at 573 K.
[b] Parameters from crystal structures. [173]

to larger particles. Curve-fitting analysis of FT-EXAFS spectra of a range of different Ag-MFI samples with varying Ag/Al ratios (**Table 2**), after C_3H_8-SCR in the presence of 0.5% H_2 revealed that, the coordination number of Ag increases as a function of Ag/Al ratio, where in the Ag-MFI-58 sample after H_2 treatment at 573 K a coordination number of 3.3 is fit with Ag-Ag distances of 2.73 Å, indicating that under these conditions the clusters are around 3–4 atoms in size. Based on the combined results from these different experimental studies, the authors proposed a most probable structure of Ag_4^+ clusters forming and serving as the active catalytic sites during lower-temperature and H_2-rich conditions of C_3H_8-SCR of NO.

Overall, this section outlines some selected and important examples of mobility of TM centers within zeolites, with a particular focus on *operando* experimental and computational studies elucidating Cu-mobility during standard SCR reactivity in chabazites. These highlighted examples demonstrate that the arrangement of such active sites during catalysis should not necessarily be assumed to be static, where one could anticipate that with further experimental & computational interrogations of TM-zeolite catalysts through state-of-the-art *operando* techniques, this phenomena could also be unraveled in other examples in the future.

6.08.3 Computational assessment of active site mobility in zeolites

6.08.3.1 Overview of enhanced sampling methods over static methods

A fundamental understanding of the functioning of active sites in zeolite catalysts at the molecular level is essential to improve catalytic processes or design new, highly selective catalysts. In this regard, the inherent characteristic dynamic behavior of zeolite materials at realistic working conditions introduces a major complexity. Modeling the dynamic nature of the active sites and their catalytic function at realistic operating conditions requires advanced operando spectroscopic and computational techniques as many zeolite catalyzed processes are typically occurring in a complex molecular environment with multiple guest species present

Author's personal copy

at higher temperatures and pressures. In recent years, the field of computational chemistry has progressively shifted from a standard static modeling approach towards these operando models. In order to properly characterize the complex dynamic environment of the zeolite catalyst, a range of methods encompassing molecular dynamics simulations, microkinetic models, machine learning algorithms, etc. are being explored.[2,182,183]

The standard quantum chemical modeling approach describes the 0 K potential energy surface (PES) of the reactive system by a discrete set of points, typically corresponding to the reactant, product and transition states. This static description of the working catalytic material can be a huge oversimplification as the structure of the active sites are presumed to remain unaltered by the reaction conditions. In reality, however, these assumptions become invalid as competitive pathways determining the product selectivity may be operational and various guest molecules may be present in the zeolite micropores, transforming the nature of the active sites. A second disadvantage of the static approach is that temperature effects are often ignored or underestimated. While at low temperature, intermediates and reactants are often well-defined stationary states on the potential energy surface, the intermediates and active sites behave dynamically at high temperature and their mobility is hence improperly accounted for.[183,184]

In zeolite catalysis, the presence of various guest species and the high reaction temperatures urge to make the transition from the PES to the free energy surface (FES) at realistic conditions. Due to the specific microporous nature of the catalyst, the FES for zeolite systems can be rather complex, exhibiting multiple local stationary states. Dynamic techniques rely on a sampling protocol to scan a larger part of the configurational space, while accounting for framework flexibility, finite temperature effects and anharmonic motions. Two general methodologies are distinguished, namely Monte Carlo (MC) simulations and Molecular Dynamics (MD) simulations, which will be the focus of this article. In MD simulations, the real-time evolution of the system on the FES is explored and an ensemble of different configurations with actual paths connecting these physical states is sampled. The temperature and pressure can be controlled by coupling a thermostat or barostat to the simulation engine in order to mimic the true experimental conditions. The energy surface may be constructed both with first-principle methods such as DFT as well as classical force-field methods, although for the description of bond formation and cleavage only a first-principle description is suitable. Since the interaction of guest molecules with the active sites often involves a rearrangement of chemical bonds and interactions, the application of DFT methods is inevitable.

Currently, the attainable time scales for first-principle MD simulations of zeolite systems—which are typically in the order of hundreds of ps—are sufficient for the description of stable configurations and local minima, while activated processes such as chemical transformations can hardly be observed in the time span of the simulation. The situation can be compared to a topographical map of a mountain landscape, as shown in **Fig. 21**. During a regular MD simulation of a few hundred picoseconds, the sampling would be limited to the mountain valleys only. However, to describe the activated processes, one would also have to visit the mountain passes with sufficiently high probabilities. Various free energy methods have been developed to enhance the sampling in low probability regions of configurational space, thus allowing to reconstruct the free energy surface for activated transitions. Some techniques improve the sampling of all degrees of freedom such as Transition Path Sampling (TPS) which, due to the high computational cost, has only limitedly found its way into the field of heterogeneous catalysis.[184–186] Alternatively, the sampling can also be enhanced along selected degrees of freedom only, the so-called collective variables (CV).

The selection of these CVs is essential for a successful description of the activated transition, though identifying all degrees of freedom involved in the reaction is not always trivial.[187,188] The premier criterion for a proper CV is its ability to uniquely distinguish between the initial state, the final state and all intermediate states while for computational efficiency, the dimensionality

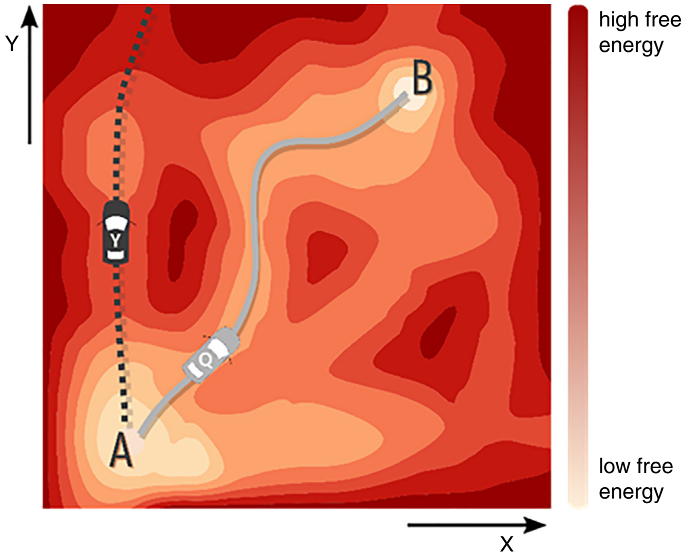

Fig. 21 Exploration of a hypothetical free energy surface by driving the sampling in various directions.

Author's personal copy

should be kept as low as possible. The CVs are described as a function of the microscopic coordinates of the system, employing often geometric parameters such as distances, angles, coordination numbers, etc. The same process can be described by multiple appropriate CVs, resulting in differently shaped free energy surfaces. A recent study on methylation reaction kinetics in zeolite ZSM-5 has shown that activation barriers estimated by employing a different set of CVs are in good agreement, provided the width of the reactant and transition state region of the free energy profiles is taken into account.[189]

Three enhanced sampling techniques which have been successfully demonstrated for zeolite-catalyzed reaction systems are Metadynamics (MTD), Umbrella Sampling (US) and Thermodynamic Integration (TI),[37,189–192] schematically represented in Fig. 22. In principle, all techniques should yield equal free energy profiles for the same reaction process if the configuration space is sampled sufficiently well.[189] Metadynamics is a non-equilibrium technique, developed by Laio and Parrinello,[193–195] in which the sampling of low probability regions is facilitated by the introduction of a bias potential acting on the selected CVs. This potential is constructed on the fly by gradually spawning Gaussian shaped hills along the system trajectory in the CV space until the potential energy of the local minima artificially increases so that reaction barriers can be overcome. The free energy profile as a function of the predefined reaction coordinate can be reconstructed by taking the opposite of the bias potential function. While the MTD method is an excellent tool to scan the configurational space of complex systems and explore reaction mechanisms, the statistical error of the method is dependent on the choice of the Gaussian hill parameters which is less desirable.[196] To speed up the convergence of the free energy profile in MTD simulations, the multiple walker MTD scheme has been proposed. Herein, multiple simulations are run in parallel which all simultaneously sample the same free energy surface though the communication between the simulations allows for a more efficient screening of different regions of the free energy surface.[197]

In the Umbrella Sampling technique, introduced by Torrie and Valleau,[198] the CV range is divided into a set of windows and for each window a biased MD simulation is carried out. An external potential restricts the sampling of the configurational space to the individual window only, thus ensuring the sampling is equally well in all regions of the CV space. The free energy profile can be reconstructed by employing a post-processing algorithm such as the weighted histogram analysis method (WHAM).[199] Also within Thermodynamic Integration, proposed by Kirkwood,[200] a number of points along the CV range are selected and for each point a constrained MD simulation at fixed CV values is performed. The free energy profile is then obtained by integrating over the averaged free energy derivative in terms of the CVs. Both techniques are computationally very efficient thanks to their high parallelizability, although a proper knowledge on the reaction mechanism and its intermediates has to be known in advance.[201] For more detailed information on free energy methods, the reader is referred to dedicated reviews.[202–204]

Through the application of MD techniques and free energy methods, several studies were able to characterize the important role of dynamic active sites in zeolite catalysis. On the one hand, Bronsted acid sites originally located on the lattice can be captured by protic molecules to form reactive clusters as demonstrated in the context of the MTO process[33,92] or even by unsaturated hydrocarbons present in the pores of the material to form carbocation intermediates in the context of alkene cracking.[36,190,205] In particular, the existence of alkyl carbocations has long been debated due to their unstable nature at low temperature. However, finite temperature effects have an important contribution to the stabilization of these intermediates and their occurrence in the zeolite environment at elevated reaction temperatures could be demonstrated by performing MD simulations in contrast to static DFT calculations.[36] MD studies in the field of selective catalytic reduction of nitrogen oxides also evidenced that the structure of Lewis acid sites can dynamically evolve in the course of the reaction.[20] Below, three examples demonstrating the beneficial use of enhanced sampling techniques for characterizing the mobility of Brønsted and Lewis acid sites are discussed in detail.

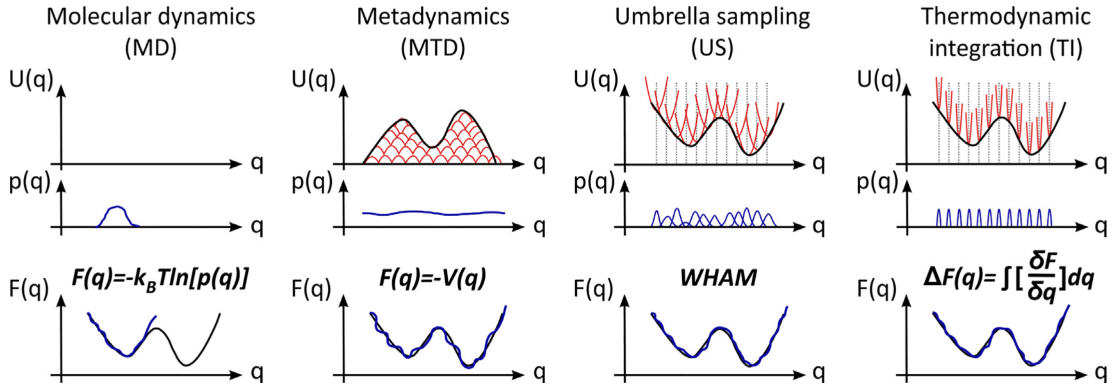

Fig. 22 Schematic representation of the regular MD and enhanced sampling techniques, metadynamics (MTD), umbrella sampling (US) and thermodynamic integration (TI) for a fictitious free energy profile F(q), bias potential U(q) and sampling probability p(q) as a function of collective variable q.

Author's personal copy

6.08.3.2 Case studies

6.08.3.2.1 Proton mobility in zeolites

As explained in Section 6.08.2.1, the BAS in zeolites becomes completely solvated once few protic molecules are adsorbed in the framework. This represents a very interesting case study for enhanced sampling techniques. Indeed, with the addition of solvent molecules the number of available configurations becomes so large that static calculations are effective only if a very large number of structures is optimized.[206] Here, we discuss two cases in which advanced sampling techniques have been effectively used to gain insight into zeolite-catalyzed reactions with mobilized protons, namely ethanol dehydration in H-β at high water loadings and the formation of surface methoxide species (SMS) at high methanol loadings, an initial reaction of the MTH process.[82]

Bates et al. have recently performed a thorough analysis of the ethanol dimerization to diethyl ether in the presence of water, catalyzed by the H-β zeolite.[207] The impact of water in the zeolite pores on the reaction kinetics and mechanism is well established. For example the velocity of H/D exchange for isobutane[208] and benzene[209] in H-ZSM-5 with relatively low Si/Al ratio increases with a loading of ~ 1 H_2O/BAS, to then decrease again when the loading exceeds 1–3 H_2O/BAS. While a few water molecules on the BAS likely make the proton transfer entropically easier, more water molecules in the proton solvation remarkably stabilize it, reducing its acidity. Also, Liu et al. studied the dehydration of cyclohexanol in water, comparing the homogenous H_3PO_4 and the H-βzeolite as catalysts, finding that the reaction proceeds remarkably faster in the latter.[210] The authors invoked a favorable association between the cyclohexanol and the hydronium ion in the zeolite with respect to pure liquid water.

When ethanol dehydration to diethyl ether is considered, a -1 order in the reaction kinetics with respect to water is found. Using a combination of in situ IR spectroscopy and ab initio molecular dynamics simulations, it was shown that in the zeolite pores a reactive cluster in the form of $(C_2H_5OH)(H_3O^+)(H_2O)_{4-5}$ is present, with more extended water networks around it whose size is dependent on the applied water pressure. The introduction of ethanol in the water cluster becomes less favorable as the cluster grows, because of the alkyl group disrupting the hydrogen bond network. Metadynamics was used to study the transition state of the reaction (Fig. 23). It was found that the ethanol molecules do not significantly disrupt the protonated water cluster and prefer to reside at its periphery. Similarly, the transition state as well resides at the periphery of the protonated water cluster. With the growth of the water cluster, the formation of the hydrophobic diethyl ether disrupts the network of hydrogen bonds significantly compared to the reacting ethanol molecules, therefore explaining the negative dependence of the reaction kinetics with respect to water pressure.

A second case in which the presence of protic molecules absorbed in the catalyst pores is known to be of fundamental importance is the MTH process which gained a lot of interest in the contemporary chemical industry,[3] as it is a possible link between sustainable raw materials and commodity chemicals. A complete overview of the intriguing MTH mechanism is outside the scope of this contribution and the interested reader is therefore referred to specialized reviews on the topic.[13,82,211,212] Here, the focus will lie on the transformations occurring at the BAS in the initial stages of the process, when methanol starts to adsorb in the catalyst pores. Once methanol (or any small alcohol in general) is introduced into the framework of a zeotype material, the acidity of the BAS immediately catalyzes dehydration reactions. These reactions can produce dimethyl ether, if methanol reacts with itself, or surface methoxide species (SMS), if the methyl group is transferred to the framework.[213,214] Interestingly, the higher basicity of methanol with respect to water implies that even less molecules are needed to solvate the BAS. This has been confirmed with AIMD since the late 1990s.[215] For instance, in the aluminophosphate zeotype material H-SAPO-34 the BAS is solvated for more than 50% of the time with only three methanol molecules, while seven water molecules are needed to reach the same result.[83]

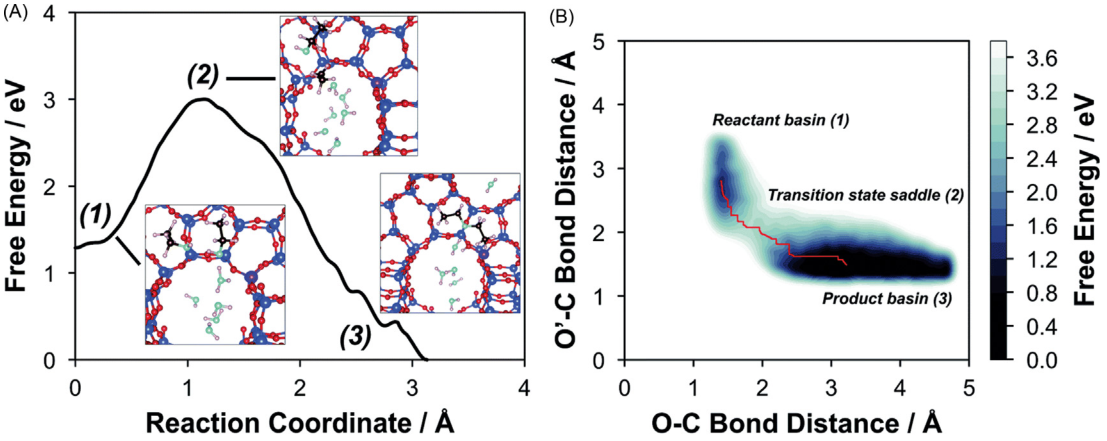

Fig. 23 (A) Reaction profile for the dehydration of ethanol to diethyl ether in H-β with 5 co-adsorbed water molecules, as obtained from metadynamics. Snapshots of the simulation are also shown. (B) The original 2-dimensional free energy surface from which the profile in (A) was derived. The minimum free energy path is shown in red. Adapted with permission from Bates, J.S.; Bukowski, B.C.; Greeley, J.; Gounder, R., Structure and Solvation of Confined Water and Water–Ethanol Clusters Within Microporous Brønsted Acids and Their Effects on Ethanol Dehydration Catalysis. *Chem. Sci.* **2020**, *11*(27), 7102–7122. Copyright 2020, The Royal Society of Chemistry.

Author's personal copy

When the formation of SMS in H-ZSM-5 was for the first time studied with advance sampling techniques,[216] it was found that static and dynamic simulations depict a very different image. Indeed, when a second methanol molecule is introduced in the reaction environment, static calculations suggest that the free energy barrier to form SMS increases (provided that thermal corrections are taken into account[217,218]), since the optimization of the transition state leads to a ring-like structure whose large entropic penalty compensates the modest enthalpic stabilization. By using metadynamics, on the other hand, the barrier was shown to decrease as a consequence of an easier proton abstraction from the framework by the two protic molecules, subsequently facilitating the SMS formation from the protonated methanol molecule.

Later on, De Wispelaere et al.[32] investigated the role of water in the MTH process. The differences between extra water and extra methanol molecules present during the SMS formation were studied in H-SAPO-34 with a combination of enhanced sampling techniques and in situ microspectroscopy. Also in this case it was found that the formation of protonated clusters, either from water or methanol, helps to reduce the reaction barrier for SMS formation (**Fig. 24**). However, this effect is smaller for water, as it actually directly competes with methanol for the access to the BAS. This reflects experimentally in a longer induction period for MTH when water is cofeed with methanol.

Based on experimental evidence suggesting that the formation of SMS can already occur at room temperature,[219–222] Nastase et al.[33] recently investigated such phenomena as a function of the acid site density and methanol loading in H-ZSM-5. By performing metadynamics, the authors demonstrated that not only larger methanol loadings can lower the methylation barriers, but also a closer proximity between Al defects, in agreement with the experimental observations. Nonetheless, the decrease in the barrier height was not as pronounced as in the experimental case, therefore the authors proposed that more Al locations or alternatively different type of active sites, such as framework-associated and extra-framework aluminum, should also be considered.

6.08.3.2.2 Ni-SSZ-24 for ethene oligomerization

Interested in the mechanism of ethene oligomerization in Ni-exchanged zeolites, Brogaard and coworkers employed advanced Umbrella Sampling simulations to probe the mechanism at operating conditions in Ni-SSZ-23 (25 bar and 120 °C) and to calculate intrinsic reaction barriers and construct free energy profiles.[23] The initial reactant state modeled was a $[Ni(C_2H_4)(C_2H_5)]^+$ species anchored to the zeolite via two Ni – O bonds, based on a key state in the Cossee-Arlman mechanism identified in a previous study.[223] DFT-MD simulations were carried out at the revPBE-D3 level, and the constructed free energy profile is outlined in **Fig. 25**, while **Fig. 26** and **Table 3** highlight the choice of collective variable employed for each process.

Initial ethene coordination was characterized to take place with accompanying formation of a ß-agostic interaction with the ethyl ligand and cleavage of both Ni—O bonds from the zeolite framework, thus mobilizing the Ni(II) cation to afford $[Ni(C_2H_5)(C_2H_4)_2]^+$. This was supported by histogram analysis of Ni-Al distances where an increase from ~3 to 6 Å is identified in the reactant and product sampling regions, respectively (**Fig. 27**A, inset). The replacement of a relatively weak-field O_{fw} ligand with a stronger η^2 ethene ligand also induces a tetrahedral/trigonal-planar to square-planar geometry change in $[Ni(C_2H_5)(C_2H_4)_2]^+$, bringing the two coupling partners closer together. C-C coupling can then take place with an intrinsic activation barrier of 37 kJ mol^{-1}, where, in reverse to the mobilization observed in the prior step, re-coordination of Ni(II) to the AlO_2^- site of the framework concomitantly takes place (again supported by shortening of the average Ni-Al interatomic distance). Following formation of the anchored $[Ni(C_4H_9)(C_2H_4)]^+$ species, coordination of additional ethene can take place with an intrinsic reaction barrier of 37 kJ mol^{-1}, followed by ß-hydrogen transfer (where $\Delta G^\ddagger = 20$ kJ mol^{-1}) to afford a mobilized $[Ni(C_4H_8)(C_2H_5)(C_2H_4)]^+$ species. Subsequent ethene coordination and 1-butene desorption can take place to regenerate the mobilized $[Ni(C_2H_4)_2(C_2H_5)]^+$ species. Alternatively, from the $[Ni(C_4H_9)(C_2H_4)]^+$ adduct, a process of ethene coordination and C-C coupling to afford the n-hexyl intermediate was also modeled, which was found to be kinetically disfavored. A microkinetic model constructed from the computed energetics identified that rate of 1-butene formation is approximately two orders of magnitude higher than 1-hexene formation, which was supported by continuous flow experiments where 98% selectivity towards butenes formation was observed over hexenes.

This study neatly demonstrates the power of *operando* modeling techniques such as US to probe and reveal the tendency of active TM sites in zeolites to mobilize under catalytic conditions. In this case, Ni(II) reversibly is shown to mobilize in the form of four-coordinate cationic organonickel complexes interacting with the zeolite framework via longer-range coulombic interactions, resembling an organometallic nickel complex interacting with solvent molecules under homogenous catalytic conditions. Ethene dimerization can take place from this state with accompanying re-anchoring of the Ni site, and comparison of the computationally-derived microkinetic model was found to be consistent with experiment.

6.08.3.2.3 Mobility of active sites in H-SSZ13 during fast NH_3-SCR-NO_x

In 2017, Schneider and coworkers employed a combination of static DFT calculations, ab initio molecular dynamics, metadynamics and complementary experimental kinetics studies to unravel the role of the Brønsted acid site in fast NH_3-SCR-NO_x in H-SSZ-13.[34] Three distinct mechanistic routes of N_2O_3 consumption, an intermediate postulated as a transient intermediate in fast SCR, were considered and modeled with this combined approach:

1. A “NH_4^+” route, in which a NH_4^+ cation interacting with the Brønsted acid site reacts with N_2O_3 to afford H_2NNO and HONO:

$$ZNH_4 + N_2O_3 \rightarrow ZH + H_2NNO + HONO$$

Author's personal copy

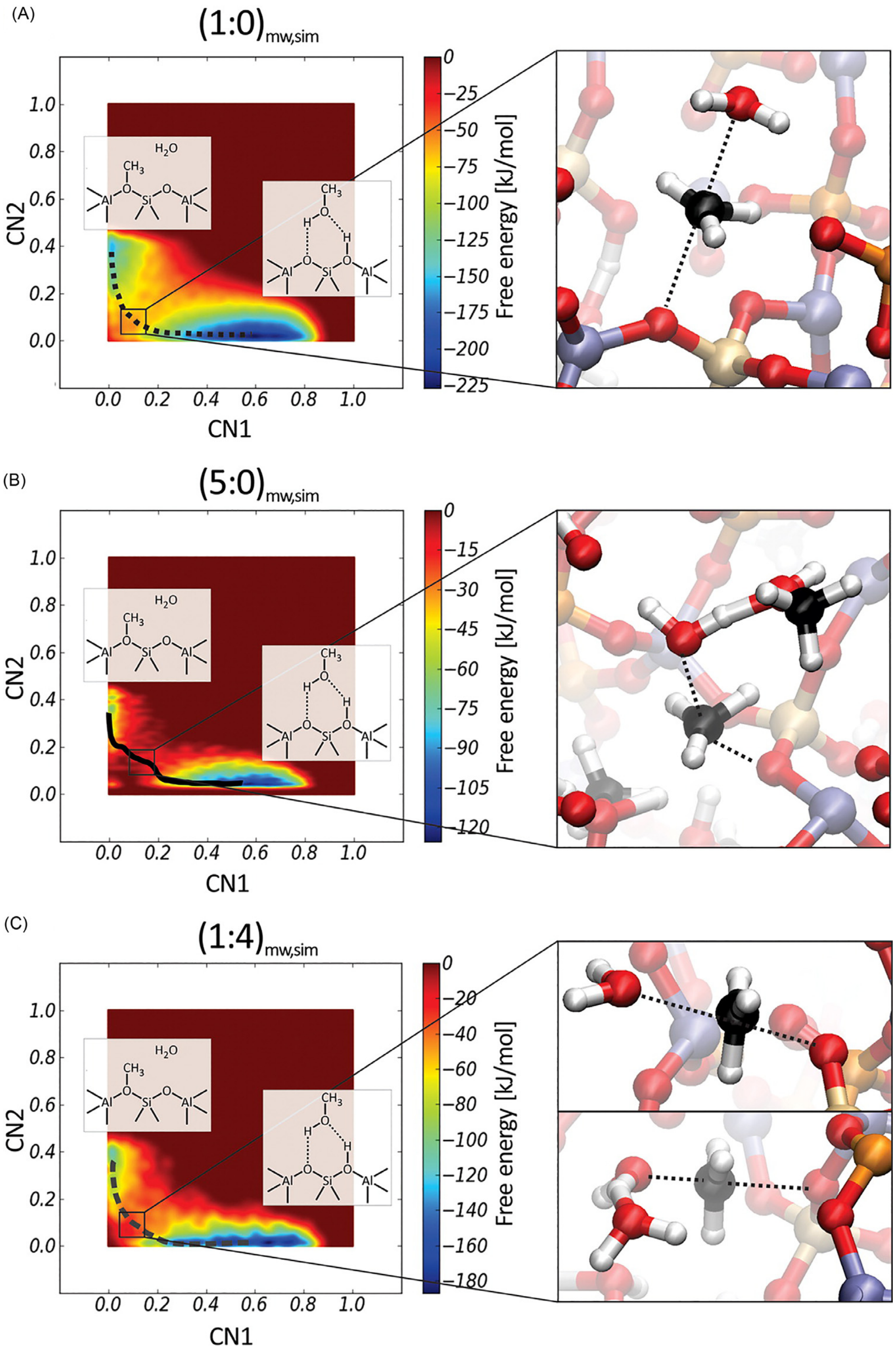

Fig. 24 2D FES at 330 °C for methoxide formation in pure methanol $(1{:}0)_{mw,sim}$ and $(5{:}0)_{mw,sim}$ (A, B) and the $(1{:}4)_{mw,sim}$ methanol-water mixture (C) occluded in H-SAPO-34, with indication of the least free energy path. The insets show snapshots of the TS region. $(x{:}y)_{mw,sim}$ stands for x MeOH and y H2O molecules per BAS. Adapted with permission from De Wispelaere, K.; Wondergem, C.S.; Ensing, B.; Hemelsoet, K.; Meijer, E.J.; Weckhuysen, B.M.; Van Speybroeck, V.; Ruiz-Martinez, J., Insight Into the Effect of Water on the Methanol-to-Olefins Conversion in H-SAPO-34 From Molecular Simulations and In Situ Microspectroscopy. *ACS Catal.* **2016**, *6*(3), 1991–2002. Copyright 2016, American Chemical Society.

Author's personal copy

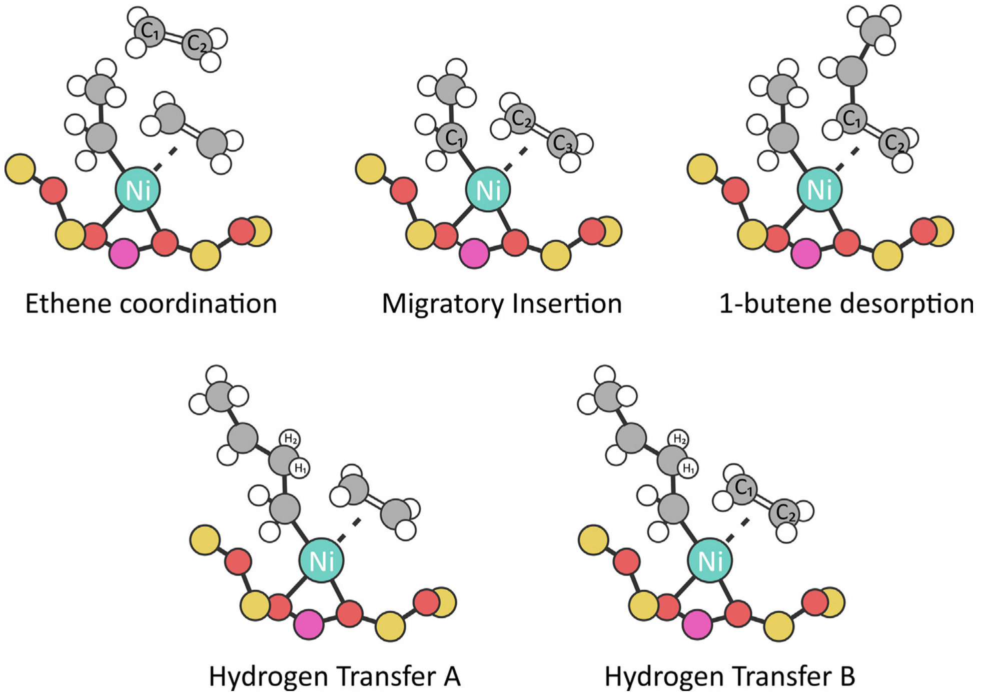

Ethene coordination

Migratory Insertion

1-butene desorption

Hydrogen Transfer A

Hydrogen Transfer B

Fig. 25 Free energy profile (in kJ/mol) of ethene oligomerization by Ni-SSZ-24 constructed from results of Umbrella Sampling calculations of the elementary steps at 25 bar and 120 °C. Reprinted from Brogaard, R.Y.; Kømurcu, M.; Dyballa, M.M.; Botan, A.; Van Speybroeck, V.; Olsbye, U.; De Wispelaere, K., Ethene Dimerization on Zeolite-Hosted Ni Ions: Reversible Mobilization of the Active Site. *ACS Catal.* **2019**, *9*(6), 5645–5650, with permission from the American Chemical Society.

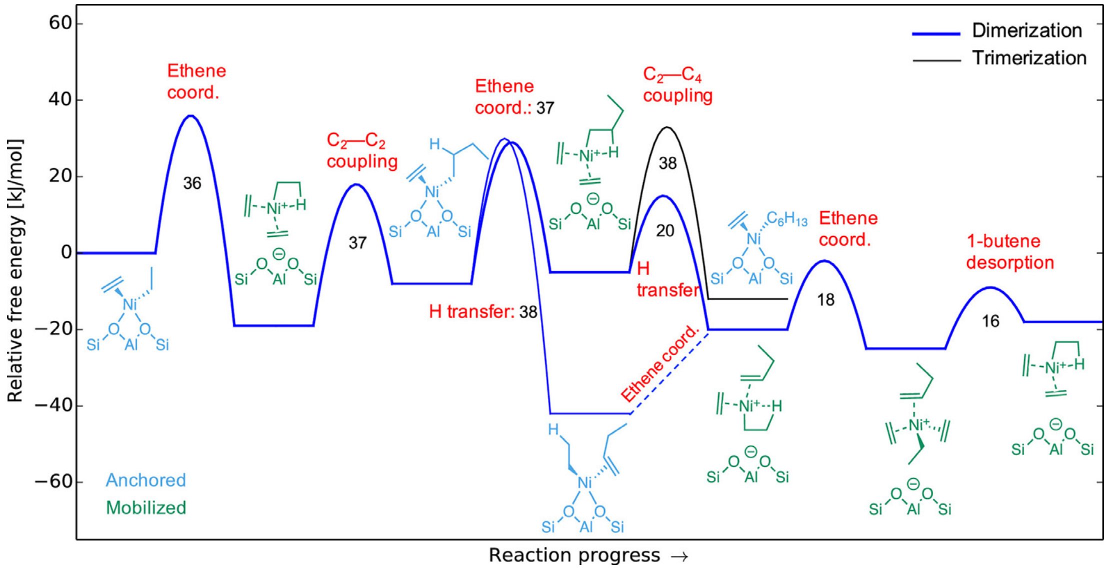

Fig. 26 Illustrative structures to outline the atoms used in the CNs used to sample each process, along with parameters. Si = yellow, O = red, Al = purple, N = blue, H = white, Ni = turquoise.

2. A "ZH" route, in which the protonated Brønsted Acid site reacts with N_2O_3 to form a short-lived "ZNO" intermediate, which is subsequently consumed by NH_3 to regenerate "ZH":

$$ZH + N_2O_3 \rightarrow ZNO + HONO$$

$$ZNO + NH_3 \rightarrow ZH + H_2NNO$$

Author's personal copy

Table 3 CN parameters for the reaction steps illustrated in Fig. 26.

Reaction step	*Coordination number*	r_0 *[Å]*	*n*	*m*
Coordination of ethene	CN (Ni, C in surrounding ethenes)	2.1	6	8
Migratory insertion	CN (C in ethene, C_α in alkyl)	1.9	6	12
Hydrogen transfer A	CN (ß-H in butyl, Ni)	1.5	6	10
Hydrogen transfer B	CN (ß-H in butyl, C in ethene)	1.8	6	12
1-butene desorption	CN(Ni, C in C═C of 1-butene)	2.7	6	10

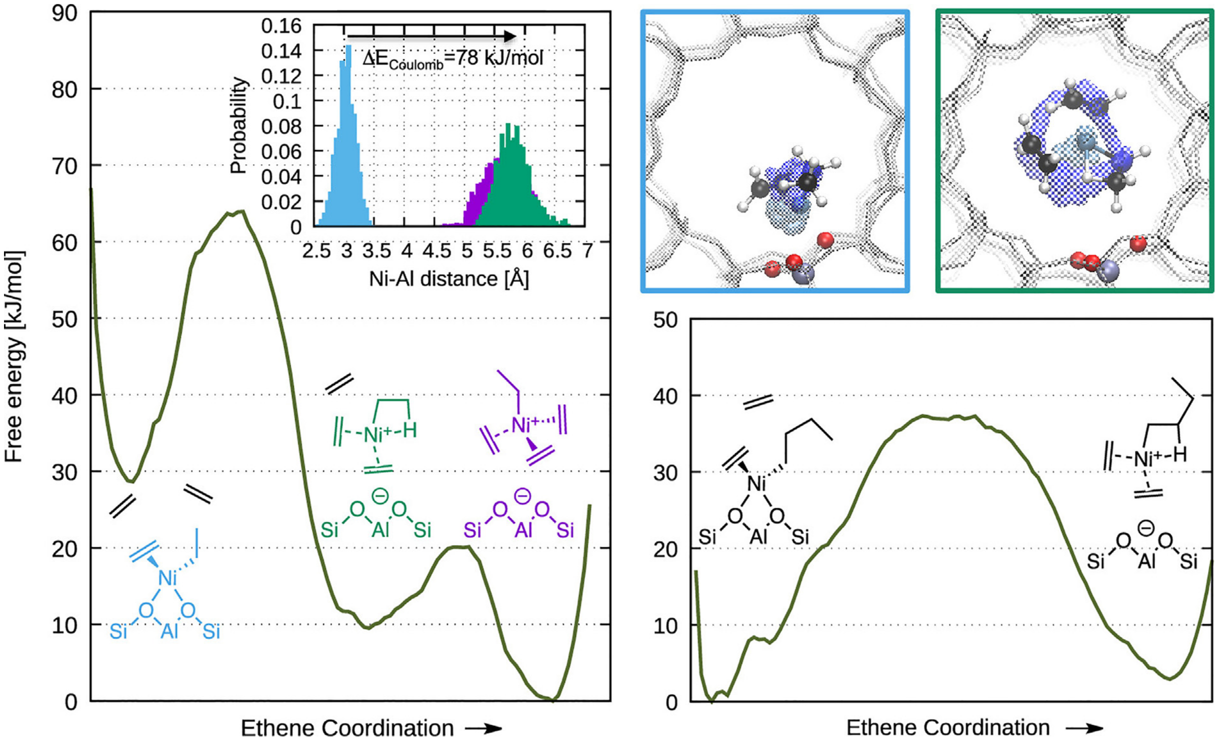

Fig. 27 Free energy profile of ethene coordination from $[Ni(C_2H_4)(C_2H_5)]^+$ complex (*left*) with Ni-Al distance histograms of the reactant and product states (*left, inset*), and from $[Ni(C_2H_4)(C_4H_9)]^+$ complex (*bottom right*). MD snapshots (*top right*) of the anchored and mobilized Ni(II) states, with the time-elapsed position of the Ni atom (*turquoise*) and Ni-bound ethyl C atom (*blue*) in the MD trajectories. Reprinted from Brogaard, R.Y.; Kømurcu, M.; Dyballa, M.M.; Botan, A.; Van Speybroeck, V.; Olsbye, U.; De Wispelaere, K., Ethene Dimerization on Zeolite-Hosted Ni Ions: Reversible Mobilization of the Active Site. *ACS Catal.* **2019**, *9*(6), 5645–5650, with permission from the American Chemical Society.

3. A "physisorbed NH_3" route, in which the tethered NH_4^+ active site is solvated with an equivalent of ammonia to form a "$ZNH_4 \cdot NH_3$" adduct, which in turn can react with N_2O_3:

$$ZNH_4 \cdot NH_3 + N_2O_3 \rightarrow ZNH_4 + H_2NNO + HONO$$

Metadynamics calculations were performed on a 12-T-site SSZ structure (Si/Al = 11) via the CPMD method at the PBE level of theory.

Initial experimental rate measurements revealed that the rate of NO_x consumption varies non-linearly with respect to temperature (Fig. 28A), where two distinct activation energies were identified depending on the temperature range. An activation energy of ~30 kJ mol^{-1} could be observed in the temperature range of 613–653 K while $E_A = 21$ kJ mol^{-1} was identified for 498–533 K.

AIMD simulations combined with a Potential Mean Force (PMF) approach were employed to assess the free energy of adsorption of NH_3. Free energies could be obtained by integrating the obtained constraint force along a predefined one-dimensional grid of separation distance between the adsorbate (NH_3) and active site (either ZH or ZNH_4^+). The coverages of NH_3 across the temperature range employed experimentally revealed that almost all Brønsted Acid sites take the form of the NH_4^+ site, and at higher temperatures a physisorbed NH_3 site of $ZNH_4 \cdot NH_3$ is unlikely to form.

The reactivity of the proposed active sites with N_2O_3 were then investigated computationally via metadynamics simulations, with two CVs sampled in each case (outlined in Fig. 29 and Table 4).

Author's personal copy

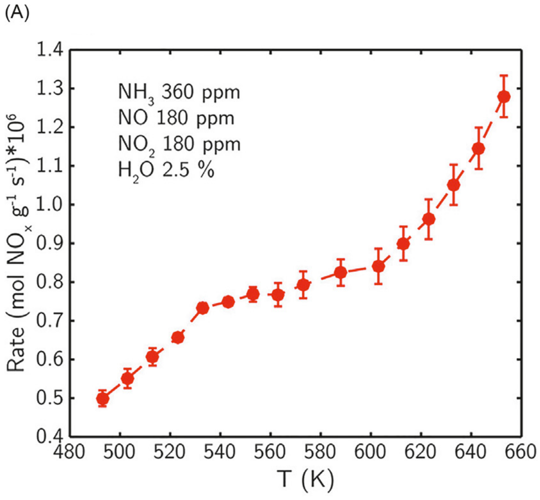

Fig. 28 (A) Rate of NO_x consumption under fast SCR conditions per gram of H-SSZ-13, versus temperature. (B) Corresponding Arrhenius plots, detailing two separate kinetic schemes at different temperature ranges. Reprinted from Li, S.; Zheng, Y.; Gao, F.; Szanyi, J.; Schneider, F.; Experimental and Computational Interrogation of Fast SCR Mechanism and Active Sites on H-Form SSZ-13. *ACS Catal.* **2017**, *7*(8), 5087–5096, with permission from the American Chemical Society.

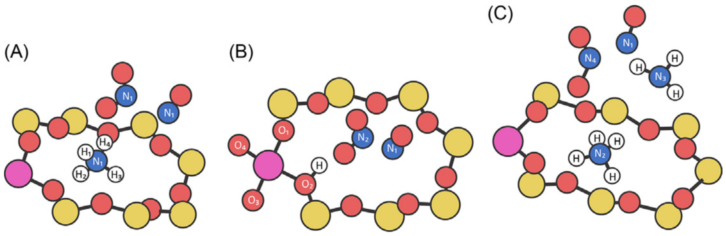

Fig. 29 Schematic structures of starting points and collective variables used in the metadynamics simulations of the (A) NH_4^+ route, (B) ZH route and (C) physisorbed NH_3 route. Si = yellow, O = red, Al = purple, N = blue, H = white.

Table 4 Collective Variables for the reaction steps illustrated in Fig. 29.

Route	*CV_1*	*CV_2*	*E_a (kJ mol^{-1})*
(a) NH_4^+	CN[N_1-N_2]	*SUM*(CN[N_2-$H_{1,2,3,4}$])	80
(b) ZH	CN[N_1-H]	*TOTAL*(CN[$N_{1,2}$-$O_{1,2,3,4}$])	100
(c) Physisorbed NH_3	*SUM*(CN[N_1-$N_{2,3}$])	TOTAL(CN[$N_{2,3}$-H_{all}])	60

The metadynamics simulations revealed that the physisorbed NH_3 route (Fig. 30C) proceeds via an activation free energy of 80 kJ mol^{-1}, where NO addition to NH_3 takes place concomitantly with hydrogen transfer from NH_3 to NO_2 to form HONO and H_2NNO. In the NH_4^+ route (Fig. 30A), NH_3 partially desorbs from the Al site before reacting in a similar manner with N_2O_3 as the physisorbed route, where $E_A = 100$ kJ mol^{-1}. Finally, the ZH route (Fig. 30B) proceeds with proton transfer from the Brønsted acid site to NO_2 to form a ZNO site takes place, with an activation energy of 60 kJ mol^{-1}.

The authors subsequently constructed a kinetic model based on the computed barriers of the three routes via metadynamics simulations, in which individual rates of the three routes were calculated as a function of temperature along with a total rate (Fig. 31). This revealed that at temperatures below 570 K, the physisorbed NH_3 reaction route dominates and contributes the most to the total rate of fast SCR in the catalytic system, and up to 570 K temperature the rate is invariant with respect to temperature. Beyond 570 K the NH_4^+ route dominates, and the initial identification of two separate temperature-dependent kinetic regimes was uncovered.

These studies therefore demonstrate the power and application of enhanced sampling techniques in the accurate *operando* modeling of mobilized catalytically active sites when used in concert with experiment. While the identification of two separate

Author's personal copy

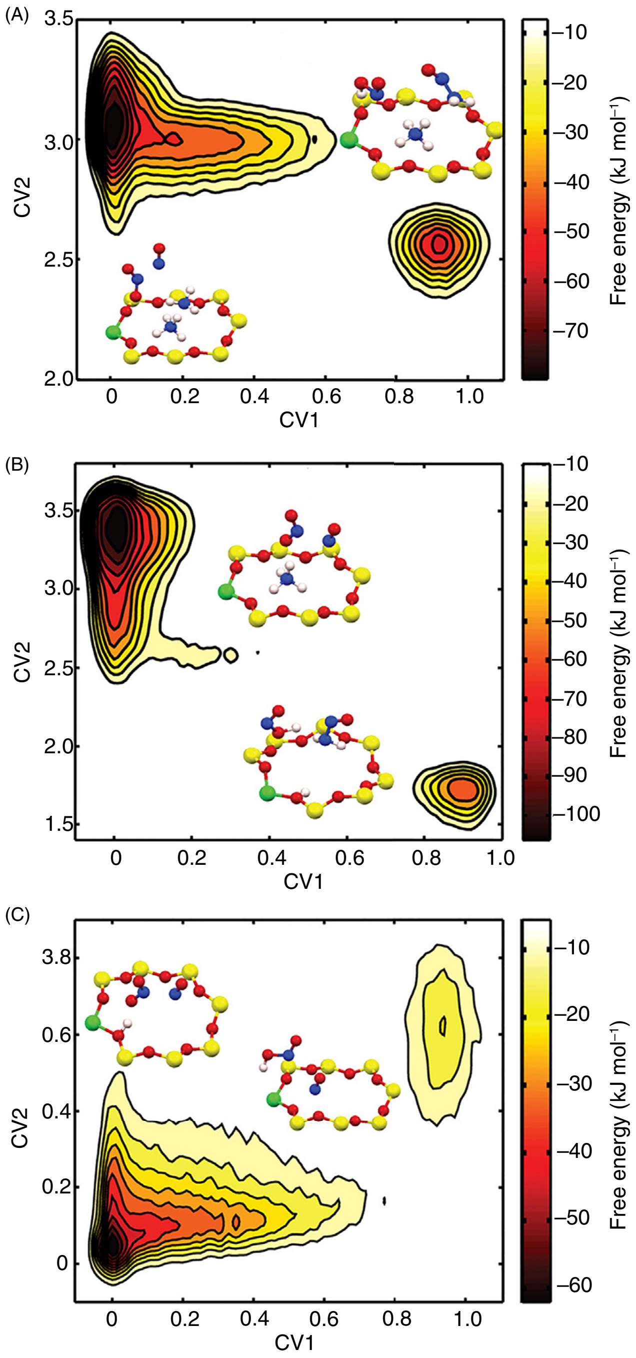

Fig. 30 2D free energy profiles for the (A) Physisorbed NH_3 route, (B) NH_4^+ route and (C) ZH route. Reprinted from Li, S.; Zheng, Y.; Gao, F.; Szanyi, J.; Schneider, F.; Experimental and Computational Interrogation of Fast SCR Mechanism and Active Sites on H-Form SSZ-13. *ACS Catal.* **2017**, *7*(8), 5087–5096, with permission from the American Chemical Society.

temperature dependent reaction-schemes in fast NH_3-SCR-NO_x reactivity in H-SSZ-13 was identified by experiment, complementary metadynamics simulations could pinpoint the mechanistic origins of this temperature-dependent behavior.

6.08.3.2.4 Mobility of multinuclear Cu sites in chabazites for the selective catalytic reduction (SCR) of nitrogen oxides

As previously outlined (Section 6.08.2.3.1.2), Gounder and coworkers employed a combination of XAS, static and dynamic DFT calculations to probe the speciation and role of mobile cationic copper sites in low-temperature NH_3-SCR.[20] The mobility of the $[Cu(NH_3)_2]^+$ complexes were assessed using metadynamics simulations via CPMD. The Cu-Al CN was chosen as the CV to describe

Author's personal copy

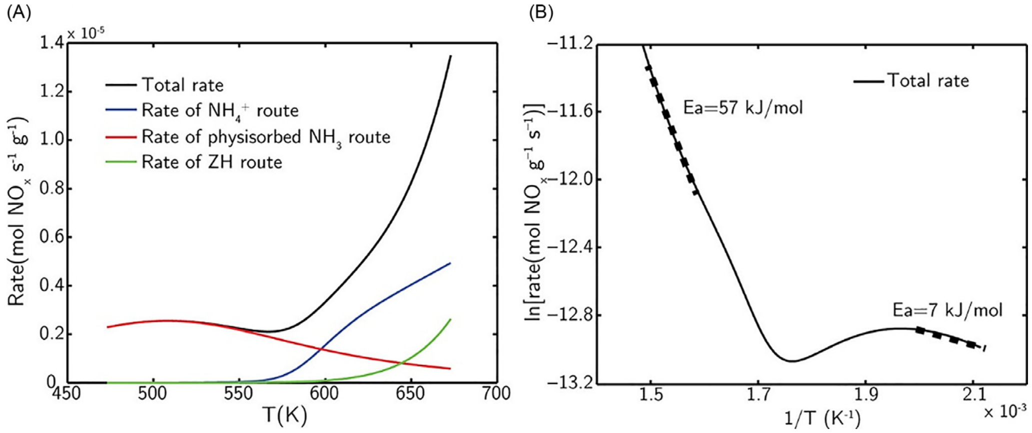

Fig. 31 (A) Computed total rate (black), and rates of the three modeled mechanistic routes as a function of simulation temperature. (B) Arrhenius plot of total rate. Reprinted from Li, S.; Zheng, Y.; Gao, F.; Szanyi, J.; Schneider, F.; Experimental and Computational Interrogation of Fast SCR Mechanism and Active Sites on H-Form SSZ-13. *ACS Catal.* **2017**, *7*(8), 5087–5096, with permission from the American Chemical Society.

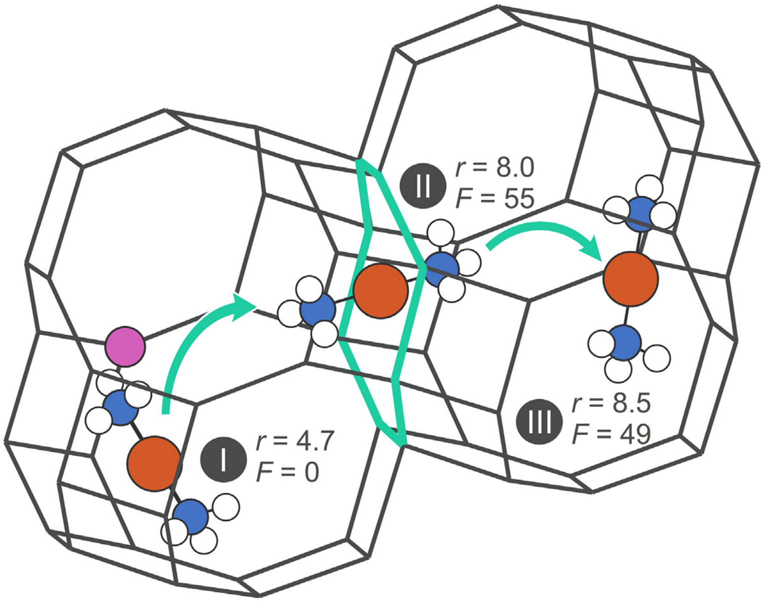

Fig. 32 Illustration of the diffusion of $[Cu(NH_3)_2]^+$ species into a neighboring chabazite cage, with Cu-Al interatomic distances (*r*, in Å) and free energies (*F*, in kJ/mol) of the reactant state (I), saddle point (II) and product (III), calculated via metadynamics simulations by Schneider and Gounder.[20]

the diffusion of $[Cu(NH_3)_2]^+$ to the adjacent CHA cage. The longest Cu-Al distance in the pre-equilibration MD simulation was chosen for the CN parameter d_0.

The metadynamics simulations, and the corresponding free energy profile revealed the $[Cu(NH_3)_2]^+$ equilibrates in the aluminated cage with a Cu-Al distance of 4.7 Å (state I, Fig. 32), upon which the free energy increases as the Cu species approaches the window to the adjacent cage, hitting a peak at a Cu-Al distance of 8 Å and an activation barrier of 55 kJ mol^{-1} (state II, Fig. 32). Finally, as $[Cu(NH_3)_2]^+$ diffuses into the neighboring cage, a local minimum (state III, Fig. 32) is observed at a Cu-Al distance of 8.5 Å. This activation barrier of 55 kJ mol^{-1} was used to estimate a rate of molecular diffusion of $6 \times 10^6\ s^{-1}$, and the fraction of mobilized $[Cu(NH_3)_2]^+$ to "anchored" Cu at the charge-compensated cage (i.e., the population of state III relative to state I at equilibrium) was estimated to be 1.4×10^{-3} at operating conditions (473 K). Moreover, the electrostatic contribution to the charge-separation of $[Cu(NH_3)_2]^+$ and the Al site was estimated using Coulomb's law, where Cu and Al were assumed to be positive and negative point-charges, respectively. This indicated that the electrostatic interactions between Cu and Al is a dominating contributor to the energetics of $[Cu(NH_3)_2]^+$ diffusion, until around 7 Å, where steric hindrance likely proceeds to play a larger contributing role in diffusing through the 8-ring window.

Author's personal copy

6.08.4 Conclusions and perspectives

Within this article, the current knowledge on the nature and evolution of active sites within zeolite catalysis has been reviewed. Recently a consensus has been reached that active sites may become very dynamic under operating conditions, where the latter may refer to altered temperatures, partial pressures, etc. In this context, the state of understanding of proton mobility, mobility of Al sites via framework decomposition, and mobility of TM-exchanged sites within zeolites has been surveyed, highlighting in particular the use of operando spectroscopic and computational methods to identify these phenomena. As many catalytic processes in nanoporous materials occur at high temperatures and are influenced by the guest adsorption in the pores, operando modeling of the catalytic function is of critical importance to accurately describe the reaction systems. The more "standard" static modeling approach starts from a few points on the potential energy surface, such as reactants, transition states and products. This is a huge oversimplification of the working catalytic material, and in reality the scene is much more complex. Competitive pathways may be operational which are essential for determining product selectivities, various guest molecules may be present in the pores of the material which may alter the nature of the active site or facilitate certain reaction paths, and the operating temperature window may change the nature of the reactive intermediates.[37,40,83] The field of computational modeling and spectroscopic characterization has evolved substantially, enabling more precise information on the nature of the active site and its mobility during operation. Using enhanced sampling MD techniques based on a first-principle description of the PES, one can map the free energy surface at realistic conditions. As such, a dynamic reorganization of catalytically active sites could be better characterized for various processes, as outlined in selected case studies. For Brønsted acidic sites, protic molecules in the zeolite pores were able to capture the proton originally located on the lattice to form protonated reactive clusters.[32,204] For Ni-zeolites used in ethene oligomerization it was shown that ethene molecules reversibly mobilize the active site and exchange with the zeolite as ligands during reaction.[23] Such reactant-mobilized active sites have also been observed in the selective catalytic reduction of nitrogen oxides with ammonia in H-SSZ-13,[34] and Cu-SSZ-13 zeolites in standard SCR and some other cases.[20] In the quest for conversion of new feedstocks such as biomass, new heterogeneous catalysts will have to be designed, containing more complex active sites, combining for example Brønsted and Lewis acid functions in close proximity.[224] Ideally one could atomically design so-called single active sites at the surface of a solid catalyst, which gives the desired function and is robust in the desired operation window.[225–227] To achieve this goal, the role of enhanced sampling techniques, in concert with accurate operando spectroscopic techniques, is expected to be crucial and increasingly prevalent in heterogeneous catalysis. Insight into the characterization of dynamic and mobile catalytic sites will both aid in the rationalization of the observed reactivities and selectivities, and will in turn inform further predictions of refined catalyst systems.

References

1. Vogt, E. T. C.; Weckhuysen, B. M. Fluid Catalytic Cracking: Recent Developments on the Grand Old Lady of Zeolite Catalysis. *Chem. Soc. Rev.* **2015,** *44* (20), 7342–7370.
2. Van Speybroeck, V.; Hemelsoet, K.; Joos, L.; Waroquier, M.; Bell, R. G.; Catlow, C. R. A. Advances in Theory and their Application Within the Field of Zeolite Chemistry. *Chem. Soc. Rev.* **2015,** *44,* 7044–7111.
3. Tian, P.; Wei, Y.; Ye, M.; Liu, Z. Methanol to Olefins (MTO): From Fundamentals to Commercialization. *ACS Catal.* **2015,** *5* (3), 1922–1938.
4. Jacobs, P. A.; Dusselier, M.; Sels, B. F. Will Zeolite-Based Catalysis Be as Relevant in Future Biorefineries as in Crude Oil Refineries? *Angew. Chem. Int. Ed.* **2014,** *53* (33), 8621–8626.
5. Dusselier, M.; Davis, M. E. Small-Pore Zeolites: Synthesis and Catalysis. *Chem. Rev.* **2018,** *118* (11), 5265–5329.
6. Ravi, M.; Sushkevich, V. L.; van Bokhoven, J. A. Towards a Better Understanding of Lewis Acidic Aluminium in Zeolites. *Nat. Mater.* **2020,** *19* (10), 1047–1056.
7. Zhang, Y.; Zhao, R.; Sanchez-Sanchez, M.; Haller, G. L.; Hu, J.; Bermejo-Deval, R.; Liu, Y.; Lercher, J. A. Promotion of Protolytic Pentane Conversion on H-MFI Zeolite by Proximity of Extra-Framework Aluminum Oxide and Brønsted Acid Sites. *J. Catal.* **2019,** *370,* 424–433.
8. Gounder, R.; Jones, A. J.; Carr, R. T.; Iglesia, E. Solvation and Acid Strength Effects on Catalysis by Faujasite Zeolites. *J. Catal.* **2012,** *286,* 214–223.
9. Almutairi, S. M. T.; Mezari, B.; Filonenko, G. A.; Magusin, P. C. M. M.; Rigutto, M. S.; Pidko, E. A.; Hensen, E. J. M. Influence of Extraframework Aluminum on the Brønsted Acidity and Catalytic Reactivity of Faujasite Zeolite. *ChemCatChem* **2013,** *5* (2), 452–466.
10. Shamzhy, M.; Opanasenko, M.; Concepción, P.; Martínez, A. New Trends in Tailoring Active Sites in Zeolite-Based Catalysts. *Chem. Soc. Rev.* **2019,** *48* (4), 1095–1149.
11. Li, G.; Pidko, E. A. The Nature and Catalytic Function of Cation Sites in Zeolites: A Computational Perspective. *ChemCatChem* **2019,** *11* (1), 134–156.
12. Hereijgers, B. P. C.; Bleken, F.; Nilsen, M. H.; Svelle, S.; Lillerud, K.-P.; Bjørgen, M.; Weckhuysen, B. M.; Olsbye, U. Product Shape Selectivity Dominates the Methanol-to-Olefins (MTO) Reaction Over H-SAPO-34 Catalysts. *J. Catal.* **2009,** *264* (1), 77–87.
13. Olsbye, U.; Svelle, S.; Bjørgen, M.; Beato, P.; Janssens, T. V. W.; Joensen, F.; Bordiga, S.; Lillerud, K. P. Conversion of Methanol to Hydrocarbons: How Zeolite Cavity and Pore Size Controls Product Selectivity. *Angew. Chem. Int. Ed.* **2012,** *51* (24), 5810–5831.
14. Cnudde, P.; Demuynck, R.; Vandenbrande, S.; Waroquier, M.; Sastre, G.; Speybroeck, V. V. Light Olefin Diffusion during the MTO Process on H-SAPO-34: A Complex Interplay of Molecular Factors. *J. Am. Chem. Soc.* **2020,** *142* (13), 6007–6017.
15. Cnudde, P.; Redekop, E. A.; Dai, W.; Porcaro, N. G.; Waroquier, M.; Bordiga, S.; Hunger, M.; Li, L.; Olsbye, U.; Van Speybroeck, V. Experimental and Theoretical Evidence for Promotional Effect of Acid Sites on the Diffusion of Alkenes Through Small-Pore Zeolites. *Angew. Chem. Int. Ed.* **2021,** *60* (18), 10016–10022.
16. Wang, S.; He, Y.; Jiao, W.; Wang, J.; Fan, W. Recent Experimental and Theoretical Studies on Al Siting/Acid Site Distribution in Zeolite Framework. *Curr. Opin. Chem. Eng.* **2019,** *23,* 146–154.
17. Yokoi, T.; Mochizuki, H.; Namba, S.; Kondo, J. N.; Tatsumi, T. Control of the Al Distribution in the Framework of ZSM-5 Zeolite and Its Evaluation by Solid-State NMR Technique and Catalytic Properties. *J. Phys. Chem. C* **2015,** *119* (27), 15303–15315.
18. Nishitoba, T.; Yoshida, N.; Kondo, J. N.; Yokoi, T. Control of Al Distribution in the CHA-Type Aluminosilicate Zeolites and its Impact on the Hydrothermal Stability and Catalytic Properties. *Ind. Eng. Chem. Res.* **2018,** *57* (11), 3914–3922.
19. Di Iorio, J. R.; Gounder, R. Controlling the Isolation and Pairing of Aluminum in Chabazite Zeolites Using Mixtures of Organic and Inorganic Structure-Directing Agents. *Chem. Mater.* **2016,** *28* (7), 2236–2247.

Author's personal copy

20. Paolucci, C.; Khurana, I.; Parekh, A. A.; Li, S.; Shih, A. J.; Li, H.; Iorio, J. R. D.; Albarracin-Caballero, J. D.; Yezerets, A.; Miller, J. T.; Delgass, W. N.; Ribeiro, F. H.; Schneider, W. F.; Gounder, R. Dynamic Multinuclear Sites Formed by Mobilized Copper Ions in NOx Selective Catalytic Reduction. *Science* **2017,** *357* (6354), 898–903.
21. Moors, S. L. C.; De Wispelaere, K.; Van der Mynsbrugge, J.; Waroquier, M.; Van Speybroeck, V. Molecular Dynamics Kinetic Study on the Zeolite-Catalyzed Benzene Methylation in ZSM-5. *ACS Catal.* **2013,** *3* (11), 2556–2567.
22. Serna, P.; Gates, B. C. Zeolite-Supported Rhodium Complexes and Clusters: Switching Catalytic Selectivity by Controlling Structures of Essentially Molecular Species. *J. Am. Chem. Soc.* **2011,** *133* (13), 4714–4717.
23. Brogaard, R. Y.; Kømurcu, M.; Dyballa, M. M.; Botan, A.; Van Speybroeck, V.; Olsbye, U.; De Wispelaere, K. Ethene Dimerization on Zeolite-Hosted Ni Ions: Reversible Mobilization of the Active Site. *ACS Catal.* **2019,** *9* (6), 5645–5650.
24. Schoonheydt, R. A.; Geerlings, P.; Pidko, E. A.; van Santen, R. A. The framework basicity of zeolites. *J. Mater. Chem.* **2012,** *22* (36), 18705–18717.
25. Losch, P.; Joshi, H.; Stegmann, N.; Vozniuk, O.; Schmidt, W. Studying Proton Mobility in Zeolites by Varying Temperature Infrared Spectroscopy. *Molecules* **2019,** *24* (17), 3199.
26. Losch, P.; Joshi, H. R.; Vozniuk, O.; Grünert, A.; Ochoa-Hernández, C.; Jabraoui, H.; Badawi, M.; Schmidt, W. Proton Mobility, Intrinsic Acid Strength, and Acid Site Location in Zeolites Revealed by Varying Temperature Infrared Spectroscopy and Density Functional Theory Studies. *J. Am. Chem. Soc.* **2018,** *140* (50), 17790–17799.
27. Osuga, R.; Yokoi, T.; Doitomi, K.; Hirao, H.; Kondo, J. N. Infrared Investigation of Dynamic Behavior of Brønsted Acid Sites on Zeolites at High Temperatures. *J. Phys. Chem. C* **2017,** *121* (45), 25411–25420.
28. Smith, L.; Cheetham, A. K.; Morris, R. E.; Marchese, L.; Thomas, J. M.; Wright, P. A.; Chen, J. On the Nature of Water Bound to a Solid Acid Catalyst. *Science* **1996,** *271* (5250), 799–802.
29. Termath, V.; Haase, F.; Sauer, J.; Hutter, J.; Parrinello, M. Understanding the Nature of Water Bound to Solid Acid Surfaces. Ab Initio Simulation on HSAPO-34. *J. Am. Chem. Soc.* **1998,** *120* (33), 8512–8516.
30. Vjunov, A.; Wang, M.; Govind, N.; Huthwelker, T.; Shi, H.; Mei, D.; Fulton, J. L.; Lercher, J. A. Tracking the Chemical Transformations at the Brønsted Acid Site Upon Water-Induced Deprotonation in a Zeolite Pore. *Chem. Mater.* **2017,** *29* (21), 9030–9042.
31. Zheng, A.; Han, B.; Li, B.; Liu, S.-B.; Deng, F. Enhancement of Brønsted Acidity in Zeolitic Catalysts Due to an Intermolecular Solvent Effect in Confined Micropores. *Chem. Commun.* **2012,** *48* (55), 6936–6938.
32. De Wispelaere, K.; Wondergem, C. S.; Ensing, B.; Hemelsoet, K.; Meijer, E. J.; Weckhuysen, B. M.; Van Speybroeck, V.; Ruiz-Martíınez, J. Insight into the Effect of Water on the Methanol-to-Olefins Conversion in H-SAPO-34 from Molecular Simulations and in Situ Microspectroscopy. *ACS Catal.* **2016,** *6* (3), 1991–2002.
33. Nastase, S. A. F.; Cnudde, P.; Vanduyfhuys, L.; De Wispelaere, K.; Van Speybroeck, V.; Catlow, C. R. A.; Logsdail, A. J. Mechanistic Insight Into the Framework Methylation of H-ZSM-5 for Varying Methanol Loadings and Si/Al Ratios Using First-Principles Molecular Dynamics Simulations. *ACS Catal.* **2020,** *10* (15), 8904–8915.
34. Li, S.; Zheng, Y.; Gao, F.; Szanyi, J.; Schneider, W. F. Experimental and Computational Interrogation of Fast SCR Mechanism and Active Sites on H-Form SSZ-13. *ACS Catal.* **2017,** *7* (8), 5087–5096.
35. Ristanović, Z.; Chowdhury, A. D.; Brogaard, R. Y.; Houben, K.; Baldus, M.; Hofkens, J.; Roeffaers, M. B. J.; Weckhuysen, B. M. Reversible and Site-Dependent Proton-Transfer in Zeolites Uncovered at the Single-Molecule Level. *J. Am. Chem. Soc.* **2018,** *140* (43), 14195–14205.
36. Cnudde, P.; De Wispelaere, K.; Van der Mynsbrugge, J.; Waroquier, M.; Van Speybroeck, V. Effect of Temperature and Branching on the Nature and Stability of Alkene Cracking Intermediates in H-ZSM-5. *J. Catal.* **2017,** *345,* 53–69.
37. Cnudde, P.; De Wispelaere, K.; Vanduyfhuys, L.; Demuynck, R.; Van der Mynsbrugge, J.; Waroquier, M.; Van Speybroeck, V. How Chain Length and Branching Influence the Alkene Cracking Reactivity on H-ZSM-5. *ACS Catal.* **2018,** *8* (10), 9579–9595.
38. Kosinov, N.; Liu, C.; Hensen, E. J. M.; Pidko, E. A. Engineering of Transition Metal Catalysts Confined in Zeolites. *Chem. Mater.* **2018,** *30* (10), 3177–3198.
39. Bailleul, S.; Yarulina, I.; Hoffman, A. E. J.; Dokania, A.; Abou-Hamad, E.; Chowdhury, A. D.; Pieters, G.; Hajek, J.; De Wispelaere, K.; Waroquier, M.; Gascon, J.; Van Speybroeck, V. A Supramolecular View on the Cooperative Role of Brønsted and Lewis Acid Sites in Zeolites for Methanol Conversion. *J. Am. Chem. Soc.* **2019,** *141* (37), 14823–14842.
40. Yarulina, I.; Wispelaere, K. D.; Bailleul, S.; Goetze, J.; Radersma, M.; Abou-Hamad, E.; Vollmer, I.; Goesten, M.; Mezari, B.; Hensen, E. J. M.; Martínez-Espín, J. S.; Morten, M.; Mitchell, S.; Perez-Ramirez, J.; Olsbye, U.; Weckhuysen, B. M.; Speybroeck, V. V.; Kapteijn, F.; Gascon, J. Structure–Performance Descriptors and the Role of Lewis Acidity in the Methanol-to-Propylene Process. *Nat. Chem.* **2018,** *10* (8), 804.
41. Dapsens, P. Y.; Mondelli, C.; Pérez-Ramírez, J. Design of Lewis-Acid Centres in Zeolitic Matrices for the Conversion of Renewables. *Chem. Soc. Rev.* **2015,** *44* (20), 7025–7043.
42. Paolucci, C.; Di Iorio, J. R.; Schneider, W. F.; Gounder, R. Solvation and Mobilization of Copper Active Sites in Zeolites by Ammonia: Consequences for the Catalytic Reduction of Nitrogen Oxides. *Acc. Chem. Res.* **2020,** *53* (9), 1881–1892.
43. Vercammen, J.; Bocus, M.; Neale, S.; Bugaev, A.; Tomkins, P.; Hajek, J.; Van Minnebruggen, S.; Soldatov, A.; Krajnc, A.; Mali, G.; Van Speybroeck, V.; De Vos, D. E. Shape-Selective C–H Activation of Aromatics to Biarylic Compounds Using Molecular Palladium in Zeolites. *Nat. Catal.* **2020,** *3* (12), 1002–1009.
44. Buurmans, I. L. C.; Weckhuysen, B. M. Heterogeneities of Individual Catalyst Particles in Space and Time as Monitored by Spectroscopy. *Nat. Chem.* **2012,** *4* (11), 873–886.
45. Weckhuysen, B. M. Chemical Imaging of Spatial Heterogeneities in Catalytic Solids at Different Length and Time Scales. *Angew. Chem. Int. Ed.* **2009,** *48* (27), 4910–4943.
46. Chowdhury, A. D.; Houben, K.; Whiting, G. T.; Chung, S.-H.; Baldus, M.; Weckhuysen, B. M. Electrophilic Aromatic Substitution over Zeolites Generates Wheland-Type Reaction Intermediates. *Nat. Catal.* **2018,** *1* (1), 23–31.
47. Hunger, M. Brønsted Acid Sites in Zeolites Characterized by Multinuclear Solid-State NMR Spectroscopy. *Catal. Rev.* **1997,** *39* (4), 345–393.
48. Freude, D.; Oehme, W.; Schmiede, H.; Staudte, B. NMR Investigation of Proton Mobility in Zeolites. *J. Catal.* **1974,** *32* (1), 137–143.
49. Baba, T.; Inoue, Y.; Shoji, H.; Uematsu, T.; Ono, Y. Temperature-Dependent Lineshape of H-1 Magic-Angle-Spinning Nuclear-Magnetic-Resonance Spectra of Acidic Hydroxyl-Groups in Zeolites. *Microporous Mater.* **1995,** *3* (6), 647–655.
50. Sarv, P.; Tuherm, T.; Lippmaa, E.; Keskinen, K.; Root, A. Mobility of the Acidic Proton in Bronsted Sites of H-Y, H-Mordenite, and H-Zsm-5 Zeolites, Studied by High-Temperature H-1 Mas NMR. *J. Phys. Chem.* **1995,** *99* (38), 13763–13768.
51. Baba, T.; Komatsu, N.; Ono, Y.; Sugisawa, H. Mobility of the Acidic Protons in H-ZSM-5 as Studied by Variable Temperature H-1 MAS NMR. *J. Phys. Chem. B* **1998,** *102* (5), 804–808.
52. Baba, T.; Komatsu, N.; Ono, Y.; Sugisawa, H.; Takahashi, T. Nature of the Acidic Protons in H-Mordenite and H-MCM-22 as Studied by Variable Temperature H-1 MAS NMR1. *Microporous Mesoporous Mater.* **1998,** *22* (1–3), 203–210.
53. Baba, T.; Ono, Y. Dynamic Properties of Protons in Solid Acids as Studied by Variable Temperature 1H MAS NMR. *Appl. Catal. Gen.* **1999,** *181* (2), 227–238.
54. Kanellopoulos, J.; Gottert, C.; Schneider, D.; Knorr, B.; Prager, D.; Ernst, H.; Freude, D. NMR Investigation of Proton Mobility in Zeolites. *J. Catal.* **2008,** *255* (1), 68–78.
55. Asakawa, N.; Motokura, K.; Yashima, T.; Koyama, T.; O-nuki, T.; Miyaji, A.; Baba, T. Proton Exchange Reaction Between Hydroxyl Groups in the Supercage and Those in the Sodalitecage of Y Zeolite As Studied by Variable Temperature H-1 MAS NMR. *J. Phys. Chem. C* **2012,** *116* (33), 17734–17738.
56. Osuga, R.; Yokoi, T.; Doitomi, K.; Hirao, H.; Kondo, J. N. Infrared Investigation of Dynamic Behavior of Bronsted Acid Sites on Zeolites at High Temperatures. *J. Phys. Chem. C* **2017,** *121* (45), 25411–25420.
57. Franke, M.; Simon, U. Characteristics of Proton Hopping in Zeolite H-ZSM5. *Phys. Status Solidi B* **2000,** *218* (1), 287–290.
58. Franke, M.; Simon, U. Proton Mobility in H-ZSM5 Studied by Impedance Spectroscopy. *Solid State Ion.* **1999,** *118* (3–4), 311–316.
59. Ryder, J. A.; Chakraborty, A. K.; Bell, A. T. Density Functional Theory Study of Proton Mobility in Zeolites: Proton Migration and Hydrogen Exchange in ZSM-5. *J. Phys. Chem. B* **2000,** *104* (30), 6998–7011.

Author's personal copy

60. Sierka, M.; Sauer, J. Proton Mobility in Chabazite, Faujasite, and ZSM-5 Zeolite Catalysts, Comparison Based on Ab Initio Calculations. *J. Phys. Chem. B* **2001,** *105* (8), 1603–1613.
61. Sierka, M.; Sauer, J. Finding Transition Structures in Extended Systems: A Strategy Based on a Combined Quantum Mechanics-Empirical Valence Bond Approach. *J. Chem. Phys.* **2000,** *112* (16), 6983–6996.
62. Huo, H.; Peng, L.; Grey, C. P. Low Temperature 1H MAS NMR Spectroscopy Studies of Proton Motion in Zeolite HZSM-5. *J. Phys. Chem. C* **2009,** *113* (19), 8211–8219.
63. Lee, B. J.; Kondo, J. N.; Wakabayashi, F.; Domen, K. Infrared Spectroscopic Study of High Temperature Behavior of the Bronsted Acidic Hydroxyl Groups on Zeolites. *Bull. Chem. Soc. Jpn.* **1998,** *71* (9), 2149–2152.
64. Franke, M. E.; Sierka, M.; Simon, U.; Sauer, J. Translational Proton Motion in Zeolite H-ZSM-5. Energy Barriers and Jump Rates from DFT Calculations. *Phys. Chem. Chem. Phys.* **2002,** *4* (20), 5207–5216.
65. Wang, Y.; Zhou, D. H.; Yang, G.; Liu, X. C.; Ma, D.; Liang, D. B.; Bao, X. H. Density Functional Theory Study of Proton Hopping in MCM-22 Zeolite. *Chem. Phys. Lett.* **2004,** *388* (4–6), 363–366.
66. Fermann, J. T.; Blanco, C.; Auerbach, S. Modeling Proton Mobility in Acidic Zeolite Clusters. I. Convergence of Transition State Parameters From Quantum Chemistry. *J. Chem. Phys.* **2000,** *112* (15), 6779–6786.
67. Tuma, C.; Sauer, J. A Hybrid MP2/Planewave-DFT Scheme for Large Chemical Systems: Proton Jumps in Zeolites. *Chem. Phys. Lett.* **2004,** *387* (4–6), 388–394.
68. Beck, L. W.; White, J. L.; Haw, J. F. 1H {27Al} Double-Resonance Experiments in Solids: An Unexpected Observation in the 1H MAS Spectrum of Zeolite HZSM-5. *J. Am. Chem. Soc.* **1994,** *116* (21), 9657–9661.
69. Brunner, E.; Beck, K.; Koch, M.; Heeribout, L.; Karge, H. Verification and Quantitative Determination of a New Type of Brønsted Acid Sites in H-ZSM-5 by 1H Magic-Angle Spinning Nuclear Magnetic Resonance Spectroscopy. *Microporous Mater.* **1995,** *3* (4–5), 395–399.
70. Freude, D. Enhanced Resolution in the 1H NMR Spectra of Zeolite H-ZSM-5 by Heteronuclear Dipolar-Dephasing Spin-Echo MAS. *Chem. Phys. Lett.* **1995,** *235* (1–2), 69–75.
71. Hunger, M. Multinuclear Solid-State NMR Studies of Acidic and Non-Acidic Hydroxyl Protons in Zeolites. *Solid State Nucl. Magn. Reson.* **1996,** *6* (1), 1–29.
72. Peng, L.; Huo, H.; Liu, Y.; Grey, C. P. 17O Magic Angle Spinning NMR Studies of Brønsted Acid Sites in Zeolites HY and HZSM-5. *J. Am. Chem. Soc.* **2007,** *129* (2), 335–346.
73. Abdolrahmani, M.; Chen, K.; White, J. L. Assessment, Control, and Impact of Brønsted Acid Site Heterogeneity in Zeolite HZSM-5. *J. Phys. Chem. C* **2018,** *122* (27), 15520–15528.
74. Schroeder, C.; Siozios, V.; Mück-Lichtenfeld, C.; Hunger, M.; Hansen, M. R.; Koller, H. Hydrogen Bond Formation of Brønsted Acid Sites in Zeolites. *Chem. Mater.* **2020,** *32* (4), 1564–1574.
75. Benco, Ľ.; Demuth, T.; Hafner, J.; Hutschka, F. Spontaneous Proton Transfer between O-Sites in Zeolites. *Chem. Phys. Lett.* **2000,** *324* (5–6), 373–380.
76. Krossner, M.; Sauer, J. Interaction of Water With Brønsted Acidic Sites of Zeolite Catalysts. Ab Initio Study of 1: 1 and 2: 1 Surface Complexes. *J. Phys. Chem.* **1996,** *100* (15), 6199–6211.
77. Jobic, H.; Tuel, A.; Krossner, M.; Sauer, J. Water in Interaction With Acid Sites in H-ZSM-5 Zeolite Does Not Form Hydroxonium Ions. A Comparison between Neutron Scattering Results and Ab Initio Calculations. *J. Phys. Chem.* **1996,** *100* (50), 19545–19550.
78. Beck, L. W.; Xu, T.; Nicholas, J. B.; Haw, J. F. Kinetic NMR and Density Functional Study of Benzene H/D Exchange in Zeolites, the Most Simple Aromatic Substitution. *J. Am. Chem. Soc.* **1995,** *117* (46), 11594–11595.
79. Wang, C.; Li, S.; Mao, X.; Caratzoulas, S.; Gorte, R. J. HD Exchange of Simple Aromatics as a Measure of Brønsted-Acid Site Strengths in Solids. *Catal. Lett.* **2018,** *148* (11), 3548–3556.
80. Rybicki, M.; Sauer, J. Ab Initio Prediction of Proton Exchange Barriers for Alkanes at Brønsted Sites of Zeolite H-MFI. *J. Am. Chem. Soc.* **2018,** *140* (51), 18151–18161.
81. Truitt, M. J.; Toporek, S. S.; Rovira-Truitt, R.; White, J. L. Alkane C—H Bond Activation in Zeolites: Evidence for Direct Protium Exchange. *J. Am. Chem. Soc.* **2006,** *128* (6), 1847–1852.
82. Van Speybroeck, V.; De Wispelaere, K.; Van der Mynsbrugge, J.; Vandichel, M.; Hemelsoet, K.; Waroquier, M. First Principle Chemical Kinetics in Zeolites: The Methanol-to-Olefin Process as a Case Study. *Chem. Soc. Rev.* **2014,** *43* (21), 7326–7357.
83. De Wispelaere, K.; Ensing, B.; Ghysels, A.; Meijer, E. J.; Van Speybroeck, V. Complex Reaction Environments and Competing Reaction Mechanisms in Zeolite Catalysis: Insights From Advanced Molecular Dynamics. *Chem. Eur. J.* **2015,** *21* (26), 9385–9396.
84. Vener, M. V.; Rozanska, X.; Sauer, J. Protonation of Water Clusters in the Cavities of Acidic Zeolites:(H 2 O) n· H-Chabazite, n = 1–4. *Phys. Chem. Chem. Phys.* **2009,** *11* (11), 1702–1712.
85. Liu, P.; Mei, D. Identifying Free Energy Landscapes of Proton Transfer Processes Between Brønsted Acid Site and Water Clusters Inside the Zeolite Pores. *J. Phys. Chem. C* **2020,** *124* (41), 22568–22576.
86. Jiménez-Ruiz, M.; Gahle, D.; Lemishko, T.; Valencia, S.; Sastre, G.; Rey, F. Evidence of Hydronium Formation in Water–Chabazite Zeolite Using Inelastic Neutron Scattering Experiments and Ab Initio Molecular Dynamics Simulations. *J. Phys. Chem. C* **2020,** *124* (9), 5436–5443.
87. Wang, M.; Jaegers, N. R.; Lee, M.-S.; Wan, C.; Hu, J. Z.; Shi, H.; Mei, D.; Burton, S. D.; Camaioni, D. M.; Gutiérrez, O. Y. Genesis and Stability of Hydronium Ions in Zeolite Channels. *J. Am. Chem. Soc.* **2019,** *141* (8), 3444–3455.
88. Zecchina, A.; Geobaldo, F.; Spoto, G.; Bordiga, S.; Ricchiardi, G.; Buzzoni, R.; Petrini, G. FTIR Investigation of the Formation of Neutral and Ionic Hydrogen-Bonded Complexes by Interaction of H-ZSM-5 and H-Mordenite With CH3CN and H2O: Comparison With the H-NAFION Superacidic System. *J. Phys. Chem.* **1996,** *100* (41), 16584–16599.
89. Nusterer, E.; Blöchl, P.; Schwarz, K. Interaction of Water and Methanol With a Zeolite at High Coverages. *Chem. Phys. Lett.* **1996,** *253* (5–6), 448–455.
90. Schwarz, K.; Nusterer, E.; Blöchl, P. E. First-Principles Molecular Dynamics Study of Small Molecules in Zeolites. *Catal. Today* **1999,** *50* (3–4), 501–509.
91. Heard, C. J.; Grajciar, L.; Nachtigall, P. The Effect of Water on the Validity of Löwenstein's Rule. *Chem. Sci.* **2019,** *10* (22), 5705–5711.
92. Bailleul, S.; Rogge, S. M. J.; Vanduyfhuys, L.; Van Speybroeck, V. Insight Into the Role of Water on the Methylation of Hexamethylbenzene in H-SAPO-34 From First Principle Molecular Dynamics Simulations. *ChemCatChem* **2019,** *11* (16), 3993–4010.
93. Olson, D.; Haag, W.; Borghard, W. Use of Water as a Probe of Zeolitic Properties: Interaction of Water With HZSM-5. *Microporous Mesoporous Mater.* **2000,** *35,* 435–446.
94. Eckstein, S.; Hintermeier, P. H.; Zhao, R.; Baráth, E.; Shi, H.; Liu, Y.; Lercher, J. A. Influence of Hydronium Ions in Zeolites on Sorption. *Angew. Chem. Int. Ed.* **2019,** *58* (11), 3450–3455.
95. Collinge, G.; Yuk, S. F.; Nguyen, M.-T.; Lee, M.-S.; Glezakou, V.-A.; Rousseau, R. Effect of Collective Dynamics and Anharmonicity on Entropy in Heterogenous Catalysis: Building the Case for Advanced Molecular Simulations. *ACS Catal.* **2020,** *10* (16), 9236–9260.
96. Heard, C. J.; Grajciar, L.; Uhlík, F.; Shamzhy, M.; Opanasenko, M.; Čejka, J.; Nachtigall, P. Zeolite (In) Stability Under Aqueous or Steaming Conditions. *Adv. Mater.* **2020;**, 2003264.
97. Chizallet, C. Toward the Atomic Scale Simulation of Intricate Acidic Aluminosilicate Catalysts. *ACS Catal.* **2020,** *10* (10), 5579–5601.
98. Silaghi, M.-C.; Chizallet, C.; Raybaud, P. Challenges on Molecular Aspects of Dealumination and Desilication of Zeolites. *Microporous Mesoporous Mater.* **2014,** *191,* 82–96.
99. Heard, C. J.; Grajciar, L.; Rice, C. M.; Pugh, S. M.; Nachtigall, P.; Ashbrook, S. E.; Morris, R. E. Fast Room Temperature Lability of Aluminosilicate Zeolites. *Nat. Commun.* **2019,** *10* (1), 1–7.
100. Pugh, S. M.; Wright, P. A.; Law, D. J.; Thompson, N.; Ashbrook, S. E. Facile, Room-Temperature 17O Enrichment of Zeolite Frameworks Revealed by Solid-State NMR Spectroscopy. *J. Am. Chem. Soc.* **2019,** *142* (2), 900–906.
101. Sun, T.; Xu, S.; Xiao, D.; Liu, Z.; Li, G.; Zheng, A.; Liu, W.; Xu, Z.; Cao, Y.; Guo, Q. Water-Induced Structural Dynamic Process in Molecular Sieves Under Mild Hydrothermal Conditions: Ship-in-a-Bottle Strategy for Acidity Identification and Catalyst Modification. *Angew. Chem.* **2020,** *132* (46), 20853–20862.

Author's personal copy

102. Lisboa, O.; Sánchez, M.; Ruette, F. Modeling Extra Framework Aluminum (EFAL) Formation in the Zeolite ZSM-5 Using Parametric Quantum and DFT Methods. *J. Mol. Catal. A Chem.* **2008,** *294* (1–2), 93–101.
103. Malola, S.; Svelle, S.; Bleken, F. L.; Swang, O. Detailed Reaction Paths for Zeolite Dealumination and Desilication From Density Functional Calculations. *Angew. Chem. Int. Ed.* **2012,** *51* (3), 652–655.
104. Sokol, A.; Catlow, C.; Garces, J.; Kuperman, A. Defect Centers in Microporous Aluminum Silicate Materials. *J. Phys. Chem. B.* **1998,** *102* (52), 10647–10649.
105. Sokol, A. A.; Catlow, C. R. A.; Garces, J.; Kuperman, A. Computational Investigation Into the Origins of Lewis Acidity in Zeolites. *Adv. Mater.* **2000,** *12* (23), 1801–1805.
106. Sokol, A. A.; Catlow, C. R. A.; Garcés, J. M.; Kuperman, A. Local States in Microporous Silica and Aluminum Silicate Materials. 1. Modeling Structure, Formation, and Transformation of Common Hydrogen Containing Defects. *J. Phys. Chem. B.* **2002,** *106* (24), 6163–6177.
107. Silaghi, M.-C.; Chizallet, C.; Petracovschi, E.; Kerber, T.; Sauer, J.; Raybaud, P. Regioselectivity of Al–O Bond Hydrolysis During Zeolites Dealumination Unified by Brønsted–Evans–Polanyi Relationship. *ACS Catal.* **2015,** *5* (1), 11–15.
108. Silaghi, M.-C.; Chizallet, C.; Sauer, J.; Raybaud, P. Dealumination Mechanisms of Zeolites and Extra-Framework Aluminum Confinement. *J. Catal.* **2016,** *339,* 242–255.
109. Nielsen, M.; Brogaard, R. Y.; Falsig, H.; Beato, P.; Swang, O.; Svelle, S. Kinetics of Zeolite Dealumination: Insights From H-SSZ-13. *ACS Catal.* **2015,** *5* (12), 7131–7139.
110. Holzinger, J.; Beato, P.; Lundegaard, L. F.; Skibsted, J. Distribution of Aluminum Over the Tetrahedral Sites in ZSM-5 Zeolites and Their Evolution After Steam Treatment. *J. Phys. Chem. C* **2018,** *122* (27), 15595–15613.
111. Valdiviés-Cruz, K.; Lam, A.; Zicovich-Wilson, C. M. Chemical Interaction of Water Molecules With Framework Al in Acid Zeolites: A Periodic Ab Initio Study on H-Clinoptilolite. *Phys. Chem. Chem. Phys.* **2015,** *17* (36), 23657–23666.
112. Stanciakova, K.; Ensing, B.; Göltl, F.; Bulo, R. E.; Weckhuysen, B. M. Cooperative Role of Water Molecules During the Initial Stage of Water-Induced Zeolite Dealumination. *ACS Catal.* **2019,** *9* (6), 5119–5135.
113. Nielsen, M.; Hafreager, A.; Brogaard, R. Y.; De Wispelaere, K.; Falsig, H.; Beato, P.; Van Speybroeck, V.; Svelle, S. Collective Action of Water Molecules in Zeolite Dealumination. *Cat. Sci. Technol.* **2019,** *9* (14), 3721–3725.
114. Sazama, P.; Wichterlova, B.; Dedecek, J.; Tvaruzkova, Z.; Musilova, Z.; Palumbo, L.; Sklenak, S.; Gonsiorova, O. FTIR and 27Al MAS NMR Analysis of the Effect of Framework Al-and Si-Defects in Micro-and Micro-Mesoporous H-ZSM-5 on Conversion of Methanol to Hydrocarbons. *Microporous Mesoporous Mater.* **2011,** *143* (1), 87–96.
115. Brus, J.; Kobera, L.; Schoefberger, W.; Urbanová, M.; Klein, P.; Sazama, P.; Tabor, E.; Sklenak, S.; Fishchuk, A. V.; Dědeček, J. Structure of Framework Aluminum Lewis Sites and Perturbed Aluminum Atoms in Zeolites as Determined by 27Al {1H} REDOR (3Q) MAS NMR Spectroscopy and DFT/Molecular Mechanics. *Angew. Chem. Int. Ed.* **2015,** *54* (2), 541–545.
116. Chen, K.; Horstmeier, S.; Nguyen, V. T.; Wang, B.; Crossley, S. P.; Pham, T.; Gan, Z.; Hung, I.; White, J. L. Structure and Catalytic Characterization of a Second Framework Al (IV) Site in Zeolite Catalysts Revealed by NMR at 35.2 T. *J. Am. Chem. Soc.* **2020,** *142* (16), 7514–7523.
117. Ruiz, J. M.; McAdon, M. H.; Garces, J. M. Aluminum Complexes as Models for Broensted Acid Sites in Zeolites: Structure and Energetics of $[\mathrm{Al\ (OH)4}]^{-}$,$[\mathrm{Al\ (H2O)6}]^{3+}$, and Intermediate Monomeric Species $[\mathrm{Al(OH)\ x\ (H2O)\ n\text{-}x\cdot mH2O}]^{3\text{-}x}$ Obtained by Hydrolysis. *J. Phys. Chem. B.* **1997,** *101* (10), 1733–1744.
118. Benco, L.; Demuth, T.; Hafner, J.; Hutschka, F.; Toulhoat, H. Extraframework Aluminum Species in Zeolites: Ab Initio Molecular Dynamics Simulation of Gmelinite. *J. Catal.* **2002,** *209* (2), 480–488.
119. Bhering, D. L.; Ramírez-Solís, A.; Mota, C. J. A Density Functional Theory Based Approach to Extraframework Aluminum Species in Zeolites. *J. Phys. Chem. B.* **2003,** *107* (18), 4342–4347.
120. Ong, L. H.; Dömök, M.; Olindo, R.; van Veen, A. C.; Lercher, J. A. Dealumination of HZSM-5 Via Steam-Treatment. *Microporous Mesoporous Mater.* **2012,** *164,* 9–20.
121. van Bokhoven, J. A.; Van der Eerden, A. M.; Koningsberger, D. C. Three-Coordinate Aluminum in Zeolites Observed With In Situ X-ray Absorption near-Edge Spectroscopy at the Al K-Edge: Flexibility of Aluminum Coordinations in Zeolites. *J. Am. Chem. Soc.* **2003,** *125* (24), 7435–7442.
122. Ravi, M.; Sushkevich, V. L.; van Bokhoven, J. A. Lewis Acidity Inherent to the Framework of Zeolite Mordenite. *J. Phys. Chem. C* **2019,** *123* (24), 15139–15144.
123. Yi, X.; Liu, K.; Chen, W.; Li, J.; Xu, S.; Li, C.; Xiao, Y.; Liu, H.; Guo, X.; Liu, S.-B. Origin and Structural Characteristics of Tri-Coordinated Extra-Framework Aluminum Species in Dealuminated Zeolites. *J. Am. Chem. Soc.* **2018,** *140* (34), 10764–10774.
124. Liu, C.; Li, G.; Hensen, E. J.; Pidko, E. A. Nature and Catalytic Role of Extraframework Aluminum in Faujasite Zeolite: A Theoretical Perspective. *ACS Catal.* **2015,** *5* (11), 7024–7033.
125. Liu, C.; Li, G.; Hensen, E. J.; Pidko, E. A. Relationship between Acidity and Catalytic Reactivity of Faujasite Zeolite: A Periodic DFT Study. *J. Catal.* **2016,** *344,* 570–577.
126. Li, S.; Zheng, A.; Su, Y.; Zhang, H.; Chen, L.; Yang, J.; Ye, C.; Deng, F. Brønsted/Lewis Acid Synergy in Dealuminated HY Zeolite: A Combined Solid-State NMR and Theoretical Calculation Study. *J. Am. Chem. Soc.* **2007,** *129* (36), 11161–11171.
127. Li, S.; Zheng, A.; Su, Y.; Fang, H.; Shen, W.; Yu, Z.; Chen, L.; Deng, F. Extra-Framework Aluminium Species in Hydrated Faujasite Zeolite as Investigated by Two-Dimensional Solid-State NMR Spectroscopy and Theoretical Calculations. *Phys. Chem. Chem. Phys.* **2010,** *12* (15), 3895–3903.
128. Chen, K.; Abdolrhamani, M.; Sheets, E.; Freeman, J.; Ward, G.; White, J. L. Direct Detection of Multiple Acidic Proton Sites in Zeolite HZSM-5. *J. Am. Chem. Soc.* **2017,** *139* (51), 18698–18704.
129. Chen, K.; Abdolrahmani, M.; Horstmeier, S.; Pham, T. N.; Nguyen, V. T.; Zeets, M.; Wang, B.; Crossley, S.; White, J. L. Brønsted–Brønsted Synergies Between Framework and Noncrystalline Protons in Zeolite H-ZSM-5. *ACS Catal.* **2019,** *9* (7), 6124–6136.
130. Schallmoser, S.; Ikuno, T.; Wagenhofer, M.; Kolvenbach, R.; Haller, G.; Sanchez-Sanchez, M.; Lercher, J. Impact of the Local Environment of Brønsted Acid Sites in ZSM-5 on the Catalytic Activity in n-Pentane Cracking. *J. Catal.* **2014,** *316,* 93–102.
131. Xue, N.; Vjunov, A.; Schallmoser, S.; Fulton, J. L.; Sanchez-Sanchez, M.; Hu, J. Z.; Mei, D.; Lercher, J. A. Hydrolysis of Zeolite Framework Aluminum and its Impact on Acid Catalyzed Alkane Reactions. *J. Catal.* **2018,** *365,* 359–366.
132. Naccache, C.; Taarit, Y. B. Transition Metal Exchanged Zeolites: Physical and Catalytic Properties. In *Zeolites: Science and Technology;* Ribeiro, F. R., Rodrigues, A. E., Rollmann, L. D., Naccache, C., Eds., Springer Netherlands: Dordrecht, 1984; pp 373–396.
133. Sachtler, W. M. H.; Zhang, Z. Zeolite-Supported Transition Metal Catalysts*. In *Advances in Catalysis;* Eley, D. D., Pines, H., Weisz, P. B., Eds.; vol. 39; Academic Press, 1993; pp 129–220.
134. Armor, J. N. Metal-Exchanged Zeolites as catalysts. *Microporous Mesoporous Mater.* **1998,** *22* (1), 451–456.
135. Pârvulescu, V. I.; Grange, P.; Delmon, B. Catalytic Removal of NO. *Catal. Today* **1998,** *46* (4), 233–316.
136. Deka, U.; Lezcano-Gonzalez, I.; Weckhuysen, B. M.; Beale, A. M. Local Environment and Nature of Cu Active Sites in Zeolite-Based Catalysts for the Selective Catalytic Reduction of NOx. *ACS Catal.* **2013,** *3* (3), 413–427.
137. EPA, U. S. *Integrated Science Assessment (ISA) for Oxides of Nitrogen—Health Criteria (Final Report, Jan 2016)*, U.S. Environmental Protection Agency: Washington, DC, 2016. EPA/600/R-15/068.
138. Li, J.; Chang, H.; Ma, L.; Hao, J.; Yang, R. T. Low-Temperature Selective Catalytic Reduction of NOx With NH3 over Metal Oxide and Zeolite Catalysts—A Review. *Catal. Today* **2011,** *175* (1), 147–156.
139. Brandenberger, S.; Kröcher, O.; Tissler, A.; Althoff, R. The State of the Art in Selective Catalytic Reduction of NOx by Ammonia Using Metal-Exchanged Zeolite Catalysts. *Catal. Rev.* **2008,** *50* (4), 492–531.
140. Beale, A. M.; Gao, F.; Lezcano-Gonzalez, I.; Peden, C. H. F.; Szanyi, J. Recent Advances in Automotive Catalysis for NOx Emission Control by Small-Pore Microporous Materials. *Chem. Soc. Rev.* **2015,** *44* (20), 7371–7405.
141. Busca, G.; Lietti, L.; Ramis, G.; Berti, F. Chemical and Mechanistic Aspects of the Selective Catalytic Reduction of NOx by Ammonia over Oxide Catalysts: A Review. *Appl. Catal. Environ.* **1998,** *18* (1), 1–36.

Author's personal copy

142. Seiyama, T.; Arakawa, T.; Matsuda, T.; Takita, Y.; Yamazoe, N. Catalytic Activity of Transition Metal Ion Exchanged Y Zeolites in the Reduction of Nitric Oxide With Ammonia. *J. Catal.* **1977,** *48* (1), 1–7.
143. Iwamoto, M.; Furukawa, H.; Mine, Y.; Uemura, F.; Mikuriya, S.-I.; Kagawa, S. Copper(II) Ion-Exchanged ZSM-5 Zeolites as Highly Active Catalysts for Direct and Continuous Decomposition of Nitrogen Monoxide. *J. Chem. Soc. Chem. Commun.* **1986**, (16), 1272–1273.
144. Iwamoto, M.; Hamada, H. Removal of Nitrogen Monoxide From Exhaust Gases Through Novel Catalytic Processes. *Catal. Today* **1991,** *10* (1), 57–71.
145. Iwamoto, M.; Yahiro, H.; Tanda, K.; Mizuno, N.; Mine, Y.; Kagawa, S. Removal of Nitrogen Monoxide Through a Novel Catalytic Process. 1. Decomposition on Excessively Copper-Ion-Exchanged ZSM-5 Zeolites. *J. Phys. Chem.* **1991,** *95* (9), 3727–3730.
146. Iwamoto, M.; Yahiro, H.; Mizuno, N.; Zhang, W. X.; Mine, Y.; Furukawa, H.; Kagawa, S. Removal of Nitrogen Monoxide Through a Novel Catalytic Process. 2. Infrared Study on Surface Reaction of Nitrogen Monoxide Adsorbed on Copper Ion-Exchanged ZSM-5 Zeolites. *J. Phys. Chem.* **1992,** *96* (23), 9360–9366.
147. Kwak, J. H.; Tonkyn, R. G.; Kim, D. H.; Szanyi, J.; Peden, C. H. F. Excellent Activity and Selectivity of Cu-SSZ-13 in the Selective Catalytic Reduction of NOx With NH3. *J. Catal.* **2010,** *275* (2), 187–190.
148. Kwak, J. H.; Tran, D.; Burton, S. D.; Szanyi, J.; Lee, J. H.; Peden, C. H. F. Effects of Hydrothermal Aging on NH3-SCR Reaction Over Cu/Zeolites. *J. Catal.* **2012,** *287,* 203–209.
149. Borfecchia, E.; Beato, P.; Svelle, S.; Olsbye, U.; Lamberti, C.; Bordiga, S. Cu-CHA—A Model System for Applied Selective Redox Catalysis. *Chem. Soc. Rev.* **2018,** *47* (22), 8097–8133.
150. Paolucci, C.; Di Iorio, J. R.; Ribeiro, F. H.; Gounder, R.; Schneider, W. F. Chapter One—Catalysis Science of NOx Selective Catalytic Reduction With Ammonia Over Cu-SSZ-13 and Cu-SAPO-34. In *Advances in Catalysis;* Song, C., Ed.; 59; Academic Press, 2016; pp 1–107.
151. Hun Kwak, J.; Zhu, H.; Lee, J. H.; Peden, C. H. F.; Szanyi, J. Two Different Cationic Positions in Cu-SSZ-13? *Chem. Commun.* **2012,** *48* (39), 4758–4760.
152. Gao, F.; Walter, E. D.; Kollar, M.; Wang, Y.; Szanyi, J.; Peden, C. H. F. Understanding Ammonia Selective Catalytic Reduction Kinetics over Cu/SSZ-13 From Motion of the Cu Ions. *J. Catal.* **2014,** *319,* 1–14.
153. Kwak, J. H.; Varga, T.; Peden, C. H. F.; Gao, F.; Hanson, J. C.; Szanyi, J. Following the Movement of Cu Ions in a SSZ-13 Zeolite during Dehydration, Reduction and Adsorption: A Combined in Situ TP-XRD, XANES/DRIFTS Study. *J. Catal.* **2014,** *314,* 83–93.
154. Lezcano-Gonzalez, I.; Deka, U.; Arstad, B.; Van Yperen-De Deyne, A.; Hemelsoet, K.; Waroquier, M.; Van Speybroeck, V.; Weckhuysen, B. M.; Beale, A. M. Determining the Storage, Availability and Reactivity of NH3 within Cu-Chabazite-Based Ammonia Selective Catalytic Reduction Systems. *Phys. Chem. Chem. Phys.* **2014,** *16* (4), 1639–1650.
155. Lezcano-Gonzalez, I.; Wragg, D. S.; Slawinski, W. A.; Hemelsoet, K.; Van Yperen-De Deyne, A.; Waroquier, M.; Van Speybroeck, V.; Beale, A. M. Determination of the Nature of the Cu Coordination Complexes Formed in the Presence of NO and NH3 Within SSZ-13. *J. Phys. Chem. C* **2015,** *119* (43), 24393–24403.
156. Giordanino, F.; Borfecchia, E.; Lomachenko, K. A.; Lazzarini, A.; Agostini, G.; Gallo, E.; Soldatov, A. V.; Beato, P.; Bordiga, S.; Lamberti, C. Interaction of NH3 With Cu-SSZ-13 Catalyst: A Complementary FTIR, XANES, and XES Study. *J. Phys. Chem. Lett.* **2014,** *5* (9), 1552–1559.
157. Paolucci, C.; Parekh, A. A.; Khurana, I.; Di Iorio, J. R.; Li, H.; Albarracin Caballero, J. D.; Shih, A. J.; Anggara, T.; Delgass, W. N.; Miller, J. T.; Ribeiro, F. H.; Gounder, R.; Schneider, W. F. Catalysis in a Cage: Condition-Dependent Speciation and Dynamics of Exchanged Cu Cations in SSZ-13 Zeolites. *J. Am. Chem. Soc.* **2016,** *138* (18), 6028–6048.
158. Lomachenko, K. A.; Borfecchia, E.; Negri, C.; Berlier, G.; Lamberti, C.; Beato, P.; Falsig, H.; Bordiga, S. The Cu-CHA deNOx Catalyst in Action: Temperature-Dependent NH3-Assisted Selective Catalytic Reduction Monitored by Operando XAS and XES. *J. Am. Chem. Soc.* **2016,** *138* (37), 12025–12028.
159. Millan, R.; Cnudde, P.; Hoffman, A. E. J.; Lopes, C. W.; Concepción, P.; van Speybroeck, V.; Boronat, M. Theoretical and Spectroscopic Evidence of the Dynamic Nature of Copper Active Sites in Cu-CHA Catalysts under Selective Catalytic Reduction (NH3–SCR–NOx) Conditions. *J. Phys. Chem. Lett.* **2020,** 10060–10066.
160. Gao, F.; Mei, D.; Wang, Y.; Szanyi, J.; Peden, C. H. F. Selective Catalytic Reduction Over Cu/SSZ-13: Linking Homo- and Heterogeneous Catalysis. *J. Am. Chem. Soc.* **2017,** *139* (13), 4935–4942.
161. Negri, C.; Selleri, T.; Borfecchia, E.; Martini, A.; Lomachenko, K. A.; Janssens, T. V. W.; Cutini, M.; Bordiga, S.; Berlier, G. Structure and Reactivity of Oxygen-Bridged Diamino Dicopper(II) Complexes in Cu-Ion-Exchanged Chabazite Catalyst for NH3-Mediated Selective Catalytic Reduction. *J. Am. Chem. Soc.* **2020,** *142* (37), 15884–15896.
162. Liu, C.; Kubota, H.; Toyao, T.; Maeno, Z.; Shimizu, K.-I. Mechanistic Insights Into the Oxidation of Copper(I) Species During NH3-SCR Over Cu-CHA Zeolites: A DFT Study. *Cat. Sci. Technol.* **2020,** *10* (11), 3586–3593.
163. Chen, L.; Janssens, T. V. W.; Vennestrøm, P. N. R.; Jansson, J.; Skoglundh, M.; Grönbeck, H. A Complete Multisite Reaction Mechanism for Low-Temperature NH3-SCR over Cu-CHA. *ACS Catal.* **2020,** *10* (10), 5646–5656.
164. Chen, L.; Janssens, T. V. W.; Grönbeck, H. A Comparative Test of Different Density Functionals for Calculations of NH3-SCR Over Cu-Chabazite. *Phys. Chem. Chem. Phys.* **2019,** *21* (21), 10923–10930.
165. Mandal, K.; Gu, Y.; Westendorff, K. S.; Li, S.; Pihl, J. A.; Grabow, L. C.; Epling, W. S.; Paolucci, C. Condition-Dependent Pd Speciation and NO Adsorption in Pd/Zeolites. *ACS Catal.* **2020,** *10* (21), 12801–12818.
166. Kubota, T.; Kumada, F.; Tominaga, H.; Kunugi, T. Oxidation of Propylene Over a Pd(II)-Cu(II)-Y Zeolite Catalyst. *Int. Chem. Eng.* **1973,** *13,* 539–545.
167. Arai, H.; Yamashiro, T.; Kubo, T.; Tominaga, H. The Catalysis of Palladium and Cupric Ion-Exchanged Zeolite for Oxidation of Ethylene. *J. Jpn. Pet. Inst.* **1976,** *18.*
168. Lapidus, A. L.; Maganya, M. I.; Maltsev, V. V. Ethylene Oligomerization Over Palladium and Rhodium Aluminosilicate Catalysts. *Neftekhimiya* **1978,** *18,* 376–379.
169. Takahashi, N.; Fujiwara, Y.; Mijin, A. Reaction of Ethylene/Propylene Mixture over Rh·Y Zeolite. *Zeolites* **1985,** *5* (6), 363–364.
170. Yashima, T.; Ushida, Y.; Ebisawa, M.; Hara, N. Polymerization of Ethylene Over Transition-Metal Exchanged Y Zeolites. *J. Catal.* **1975,** *36* (3), 320–326.
171. Ogino, I.; Gates, B. C. Role of the Support in Catalysis: Activation of a Mononuclear Ruthenium Complex for Ethene Dimerization by Chemisorption on Dealuminated Zeolite Y. *Chem. A Eur. J.* **2009,** *15* (28), 6827–6837.
172. Serna, P.; Gates, B. C. A Bifunctional Mechanism for Ethene Dimerization: Catalysis by Rhodium Complexes on Zeolite HY in the Absence of Halides. *Angew. Chem. Int. Ed.* **2011,** *50* (24), 5528–5531.
173. Shibata, J.; Shimizu, K.-I.; Takada, Y.; Shichi, A.; Yoshida, H.; Satokawa, S.; Satsuma, A.; Hattori, T. Structure of Active Ag Clusters in Ag Zeolites for SCR of NO by Propane in the Presence of Hydrogen. *J. Catal.* **2004,** *227* (2), 367–374.
174. Shibata, J.; Takada, Y.; Shichi, A.; Satokawa, S.; Satsuma, A.; Hattori, T. Ag Cluster as Active Species for SCR of NO by Propane in the Presence of Hydrogen over Ag-MFI. *J. Catal.* **2004,** *222* (2), 368–376.
175. Linnert, T.; Mulvaney, P.; Henglein, A.; Weller, H. Long-Lived Nonmetallic Silver Clusters in Aqueous Solution: Preparation and Photolysis. *J. Am. Chem. Soc.* **1990,** *112* (12), 4657–4664.
176. Mulvaney, P.; Henglein, A. Long-Lived Nonmetallic Silver Clusters in Aqueous Solution: A Pulse Radiolysis Study of Their Formation. *J. Phys. Chem.* **1990,** *94* (10), 4182–4188.
177. Ershov, B. G.; Janata, E.; Henglein, A. Growth of Silver Particles in Aqueous Solution: Long-Lived "Magic" Clusters and Ionic Strength Effects. *J. Phys. Chem.* **1993,** *97* (2), 339–343.
178. Gachard, E.; Belloni, J.; Subramanian, M. A. Optical and EPR Spectroscopic Studies of Silver Clusters in Ag,Na-Y Zeolite by γ-Irradiation. *J. Mater. Chem.* **1996,** *6* (5), 867–870.
179. Michalik, J.; Sadlo, J.; Kodaira, T.; Shimomura, S.; Yamada, H. ESR and Optical Studies of Cationic Silver Clusters in Zeolite Rho. *J. Radioanal. Nucl. Chem.* **1998,** *232* (1), 135–138.
180. Sato, K.; Yoshinari, T.; Kintaichi, Y.; Haneda, M.; Hamada, H. Remarkable Promoting Effect of Rhodium on the Catalytic Performance of Ag/Al_2O_3 for the Selective Reduction of NO With Decane. *Appl. Catal. Environ.* **2003,** *44* (1), 67–78.

Author's personal copy

181. Chemical Evidence for Charged Clusters in Silver Zeolites. In *Studies in Surface Science and Catalysis;* Beyer, H. K., Jacobs, P. A., Jacobs, P. A., Jaeger, N. I., JírŮ, P., Schulz-Ekloff, G., Eds.; vol. 12; Elsevier, 1982; pp 95–102.
182. Bruix, A.; Margraf, J. T.; Andersen, M.; Reuter, K. First-Principles-Based Multiscale Modelling of Heterogeneous Catalysis. *Nat. Catal.* **2019,** *2* (8), 659–670.
183. Grajciar, L.; Heard, C. J.; Bondarenko, A. A.; Polynski, M. V.; Meeprasert, J.; Pidko, E. A.; Nachtigall, P. Towards Operando Computational Modeling in Heterogeneous Catalysis. *Chem. Soc. Rev.* **2018,** *47* (22), 8307–8348.
184. Bučko, T.; Benco, L.; Hafner, J.; Ángyán, J. G. Monomolecular Cracking of Propane Over Acidic Chabazite: An Ab Initio Molecular Dynamics and Transition Path Sampling Study. *J. Catal.* **2011,** *279* (1), 220–228.
185. Dellago, C.; Bolhuis, P. G.; Geissler, P. L. Transition Path Sampling. In *Advances in Chemical Physics;* Prigogine, I., Rice, S. A., Eds., John Wiley & Sons, Inc., 2002; pp 1–78.
186. van Erp, T. S.; Bolhuis, P. G. Elaborating Transition Interface Sampling Methods. *J. Comput. Phys.* **2005,** *205* (1), 157–181.
187. Rohrdanz, M. A.; Zheng, W.; Clementi, C. Discovering Mountain Passes Via Torchlight: Methods for the Definition of Reaction Coordinates and Pathways in Complex Macromolecular Reactions. *Annu. Rev. Phys. Chem.* **2013,** *64* (1), 295–316.
188. Krivov, S. V.; Karplus, M. Hidden Complexity of Free Energy Surfaces for Peptide (Protein) Folding. *PNAS* **2004,** *101* (41), 14766–14770.
189. Bailleul, S.; Dedecker, K.; Cnudde, P.; Vanduyfhuys, L.; Waroquier, M.; Van Speybroeck, V. Ab Initio Enhanced Sampling Kinetic Study on MTO Ethene Methylation Reaction. *J. Catal.* **2020,** *388,* 38–51.
190. Rey, J.; Raybaud, P.; Chizallet, C.; Bučko, T. Competition of Secondary Versus Tertiary Carbenium Routes for the Type B Isomerization of Alkenes Over Acid Zeolites Quantified by Ab Initio Molecular Dynamics Simulations. *ACS Catal.* **2019,** 9813–9828.
191. De Wispelaere, K.; Bailleul, S.; Van Speybroeck, V. Towards Molecular Control of Elementary Reactions in Zeolite Catalysis by Advanced Molecular Simulations Mimicking Operating Conditions. *Cat. Sci. Technol.* **2016,** *6* (8), 2686–2705.
192. Rey, J.; Bignaud, C.; Raybaud, P.; Bučko, T.; Chizallet, C. Dynamic Features of Transition States for β-Scission Reactions of Alkenes Over Acid Zeolites Revealed by AIMD Simulations. *Angew. Chem.* **2020,** *132* (43), 19100–19104.
193. Laio, A.; Rodriguez-Fortea, A.; Gervasio, F. L.; Ceccarelli, M.; Parrinello, M. Assessing the Accuracy of Metadynamics†. *J. Phys. Chem. B* **2005,** *109* (14), 6714–6721.
194. Laio, A.; Parrinello, M. Escaping Free-Energy Minima. *PNAS* **2002,** *99* (20), 12562–12566.
195. Laio, A.; Gervasio, F. L. Metadynamics: A Method to Simulate Rare Events and Reconstruct the Free Energy in Biophysics, Chemistry and Material Science. *Rep. Prog. Phys.* **2008,** *71* (12), 126601.
196. Barducci, A.; Bonomi, M.; Parrinello, M. Metadynamics. *Wiley Interdiscip. Rev.: Comput. Mol. Sci.* **2011,** *1* (5), 826–843.
197. Raiteri, P.; Laio, A.; Gervasio, F. L.; Micheletti, C.; Parrinello, M. Efficient Reconstruction of Complex Free Energy Landscapes by Multiple Walkers Metadynamics. *J. Phys. Chem. B* **2006,** *110* (8), 3533–3539.
198. Torrie, G. M.; Valleau, J. P. Nonphysical Sampling Distributions in Monte Carlo Free-Energy Estimation: Umbrella Sampling. *J. Comput. Phys.* **1977,** *23* (2), 187–199.
199. Kumar, S.; Rosenberg, J. M.; Bouzida, D.; Swendsen, R. H.; Kollman, P. A. THE Weighted Histogram Analysis Method for Free-Energy Calculations on Biomolecules. I. THE Method. *J. Comput. Chem.* **1992,** *13* (8), 1011–1021.
200. Kirkwood, J. G. Statistical Mechanics of Fluid Mixtures. *J. Chem. Phys.* **1935,** *3* (5), 300–313.
201. Kästner, J. Umbrella sampling. *Wiley Interdiscip. Rev.: Comput. Mol. Sci.* **2011,** *1* (6), 932–942.
202. Hansen, N.; van Gunsteren, W. F. Practical Aspects of Free-Energy Calculations: A Review. *J. Chem. Theory Comput.* **2014,** *10* (7), 2632–2647.
203. Abrams, C.; Bussi, G. Enhanced Sampling in Molecular Dynamics Using Metadynamics, Replica-Exchange, and Temperature-Acceleration. *Entropy* **2013,** *16* (1), 163–199.
204. Pietrucci, F. Strategies for the Exploration of Free Energy Landscapes: Unity in Diversity and Challenges Ahead. *Rev. Phys.* **2017,** *2,* 32–45.
205. Hajek, J.; Van der Mynsbrugge, J.; De Wispelaere, K.; Cnudde, P.; Vanduyfhuys, L.; Waroquier, M.; Van Speybroeck, V. On the Stability and Nature of Adsorbed Pentene in Brønsted Acid Zeolite H-ZSM-5 at 323 K. *J. Catal.* **2016,** *340,* 227–235.
206. Hoffman, A. J.; Bates, J. S.; Di Iorio, J. R.; Nystrom, S. V.; Nimlos, C. T.; Gounder, R.; Hibbitts, D. Rigid Arrangements of Ionic Charge in Zeolite Frameworks Conferred by Specific Aluminum Distributions Preferentially Stabilize Alkanol Dehydration Transition States. *Angew. Chem. Int. Ed.* **2020,** *59* (42), 18686–18694.
207. Bates, J. S.; Bukowski, B. C.; Greeley, J.; Gounder, R. Structure and Solvation of Confined Water and Water–Ethanol Clusters Within Microporous Brønsted Acids and Their Effects on Ethanol Dehydration Catalysis. *Chem. Sci.* **2020,** *11* (27), 7102–7122.
208. Chen, K.; Damron, J.; Pearson, C.; Resasco, D.; Zhang, L.; White, J. L. Zeolite Catalysis: Water Can Dramatically Increase or Suppress Alkane C–H Bond Activation. *ACS Catal.* **2014,** *4* (9), 3039–3044.
209. Chen, K.; Gumidyala, A.; Abdolrhamani, M.; Villines, C.; Crossley, S.; White, J. L. Trace Water Amounts Can Increase Benzene H/D Exchange Rates in an Acidic Zeolite. *J. Catal.* **2017,** *351,* 130–135.
210. Liu, Y.; Vjunov, A.; Shi, H.; Eckstein, S.; Camaioni, D. M.; Mei, D.; Baráth, E.; Lercher, J. A. Enhancing the Catalytic Activity of Hydronium Ions Through Constrained Environments. *Nat. Commun.* **2017,** *8* (1), 1–8.
211. Hemelsoet, K.; Van der Mynsbrugge, J.; De Wispelaere, K.; Waroquier, M.; Van Speybroeck, V. Unraveling the Reaction Mechanisms Governing Methanol-to-Olefins Catalysis by Theory and Experiment. *ChemPhysChem* **2013,** *14* (8), 1526–1545.
212. Yarulina, I.; Chowdhury, A. D.; Meirer, F.; Weckhuysen, B. M.; Gascon, J. Recent Trends and Fundamental Insights in the Methanol-to-Hydrocarbons Process. *Nat. Catal.* **2018,** *1* (6), 398–411.
213. Wang, W.; Seiler, M.; Hunger, M. Role of Surface Methoxy Species in the Conversion of Methanol to Dimethyl Ether on Acidic Zeolites Investigated by in Situ Stopped-Flow MAS NMR Spectroscopy. *J. Phys. Chem. B.* **2001,** *105* (50), 12553–12558.
214. Wang, W.; Buchholz, A.; Seiler, M.; Hunger, M. Evidence for an Initiation of the Methanol-to-Olefin Process by Reactive Surface Methoxy Groups on Acidic Zeolite Catalysts. *J. Am. Chem. Soc.* **2003,** *125* (49), 15260–15267.
215. Gale, J.; Shah, R.; Payne, M.; Stich, I.; Terakura, K. Methanol in Microporous Materials From First Principles. *Catal. Today* **1999,** *50* (3–4), 525–532.
216. Van der Mynsbrugge, J.; Moors, S. L.; De Wispelaere, K.; Van Speybroeck, V. Insight into the Formation and Reactivity of Framework-Bound Methoxide Species in H-ZSM-5 From Static and Dynamic Molecular Simulations. *ChemCatChem* **2014,** *6* (7), 1906–1918.
217. Lesthaeghe, D.; Van Speybroeck, V.; Marin, G. B.; Waroquier, M. Understanding the Failure of Direct C-C Coupling in the Zeolite-Catalyzed Methanol-to-Olefin Process. *Angew. Chem.* **2006,** *118* (11), 1746–1751.
218. Maihom, T.; Boekfa, B.; Sirijaraensre, J.; Nanok, T.; Probst, M.; Limtrakul, J. Reaction Mechanisms of the Methylation of Ethene With Methanol and Dimethyl Ether Over H-ZSM-5: An ONIOM Study. *J. Phys. Chem. C* **2009,** *113* (16), 6654–6662.
219. Salvador, P.; Kladnig, W. Surface Reactivity of Zeolites Type HY and Na-Y With Methanol. *J. Chem. Soc., Faraday Trans. 1* **1977,** *73,* 1153–1168.
220. O'malley, A. J.; Parker, S. F.; Chutia, A.; Farrow, M. R.; Silverwood, I. P.; García-Sakai, V.; Catlow, C. R. A. Room Temperature Methoxylation in Zeolites: Insight Into a Key Step of the Methanol-to-Hydrocarbons Process. *Chem. Commun.* **2016,** *52* (14), 2897–2900.
221. Matam, S. K.; Howe, R. F.; Thetford, A.; Catlow, C. R. A. Room Temperature Methoxylation in Zeolite H-ZSM-5: An Operando DRIFTS/Mass Spectrometric Study. *Chem. Commun.* **2018,** *54* (91), 12875–12878.
222. Matam, S. K.; Nastase, S. A.; Logsdail, A. J.; Catlow, C. R. A. Methanol Loading Dependent Methoxylation in Zeolite H-ZSM-5. *Chem. Sci.* **2020,** *11* (26), 6805–6814.
223. Brogaard, R. Y.; Olsbye, U. Ethene Oligomerization in Ni-Containing Zeolites: Theoretical Discrimination of Reaction Mechanisms. *ACS Catal.* **2016,** *6* (2), 1205–1214.
224. Sudarsanam, P.; Peeters, E.; Makshina, E. V.; Parvulescu, V. I.; Sels, B. F. Advances in Porous and Nanoscale Catalysts for Viable Biomass Conversion. *Chem. Soc. Rev.* **2019,** *48* (8), 2366–2421.

Author's personal copy

225. Rogge, S. M. J.; Bavykina, A.; Hajek, J.; Garcia, H.; Olivos-Suarez, A. I.; Sepulveda-Escribano, A.; Vimont, A.; Clet, G.; Bazin, P.; Kapteijn, F.; Daturi, M.; Ramos-Fernandez, E. V.; Xamena, F.; Van Speybroeck, V.; Gascon, J. Metal-Organic and Covalent Organic Frameworks as Single-Site Catalysts. *Chem. Soc. Rev.* **2017,** *46* (11), 3134–3184.
226. Copéret, C.; Comas-Vives, A.; Conley, M. P.; Estes, D. P.; Fedorov, A.; Mougel, V.; Nagae, H.; Núñez-Zarur, F.; Zhizhko, P. A. Surface Organometallic and Coordination Chemistry Toward Single-Site Heterogeneous Catalysts: Strategies, Methods, Structures, and Activities. *Chem. Rev.* **2016,** *116* (2), 323–421.
227. Thomas, J. M.; Raja, R.; Lewis, D. W. Single-Site Heterogeneous Catalysts. *Angew. Chem. Int. Ed.* **2005,** *44* (40), 6456–6482.